



저작자표시-비영리-변경금지 2.0 대한민국

이용자는 아래의 조건을 따르는 경우에 한하여 자유롭게

- 이 저작물을 복제, 배포, 전송, 전시, 공연 및 방송할 수 있습니다.

다음과 같은 조건을 따라야 합니다:



저작자표시. 귀하는 원저작자를 표시하여야 합니다.



비영리. 귀하는 이 저작물을 영리 목적으로 이용할 수 없습니다.



변경금지. 귀하는 이 저작물을 개작, 변형 또는 가공할 수 없습니다.

- 귀하는, 이 저작물의 재이용이나 배포의 경우, 이 저작물에 적용된 이용허락조건을 명확하게 나타내어야 합니다.
- 저작권자로부터 별도의 허가를 받으면 이러한 조건들은 적용되지 않습니다.

저작권법에 따른 이용자의 권리는 위의 내용에 의하여 영향을 받지 않습니다.

이것은 [이용허락규약\(Legal Code\)](#)을 이해하기 쉽게 요약한 것입니다.

[Disclaimer](#)

Doctoral Thesis

Deciphering the Molecular Mechanisms of  
Orai1-dependent Entosis in Cancer Development  
and SEPTINs Cleavage-mediated  
Ciliary Defects in Coronavirus Infection

Ah Reum Lee

Department of Biological Sciences

Ulsan National Institute of Science and Technology

2023

Deciphering the Molecular Mechanisms of  
Orai1-dependent Entosis in Cancer Development  
and SEPTINs Cleavage-mediated  
Ciliary Defects in Coronavirus Infection

Ah Reum Lee

Department of Biological Sciences

Ulsan National Institute of Science and Technology

Deciphering the Molecular Mechanisms of  
Orai1-dependent Entosis in Cancer Development and  
SEPTINs Cleavage-mediated  
Ciliary Defects in Coronavirus Infection

A thesis/dissertation submitted to  
Ulsan National Institute of Science and Technology  
in partial fulfillment of the  
requirements for the degree of  
Doctor of Philosophy

Ah Reum Lee

06.09.2023 of submission

Approved by



Advisor

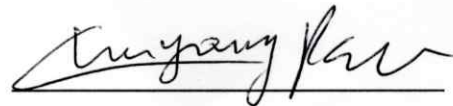
Chan Young Park

# Deciphering the Molecular Mechanisms of Orai1-dependent Entosis in Cancer Development and SEPTINs Cleavage-mediated Ciliary Defects in Coronavirus Infection

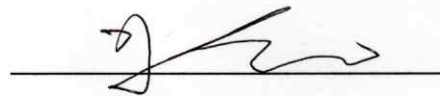
Ah Reum Lee

This certifies that the thesis/dissertation of Ah Reum Lee is approved.

06.09.2023 of submission



Advisor: Chan Young Park



Tae Joo Park



Myung Gon Ko



Taejoon Kwon



Woonggyu Jung

## Abstract

The cytoskeleton is a complex network of protein filaments that plays a crucial role in maintaining cell shape, organizing cellular components, and coordinating various cellular processes. This study aimed to explore the regulation of the cytoskeleton in the context of cancer development and investigate the mechanism underlying cytoskeletal defects during virus infection. It provides insights into the pathogenesis of various disease and identify potential therapeutic targets.

In the first part, I described the regulation mechanism of cytoskeleton during cancer development, specifically in the context of Entosis. Entosis is a non-apoptotic cell death process that forms characteristic cell-in-cell structures in cancers, killing invading cells. Intracellular  $\text{Ca}^{2+}$  dynamics are essential for cellular processes, including actomyosin contractility, migration, and autophagy. However, the significance of  $\text{Ca}^{2+}$  and  $\text{Ca}^{2+}$  channels participating in entosis are unclear. Here, I showed that intracellular  $\text{Ca}^{2+}$  signaling regulates entosis via SEPTIN-Orai1- $\text{Ca}^{2+}$ /CaM-MLCK-actomyosin axis. Intracellular  $\text{Ca}^{2+}$  oscillations in entotic cells showed spatiotemporal variations during engulfment, mediated by Orai1  $\text{Ca}^{2+}$  channels in plasma membranes. SEPTIN controlled polarized distribution of Orai1 for local MLCK activation, resulting in MLC phosphorylation and actomyosin contraction, leading to internalization of invasive cells.  $\text{Ca}^{2+}$  chelators and SEPTIN, Orai1, and MLCK inhibitors suppressed entosis. This study identified potential targets for treating entosis-associated tumors, showed that Orai1 is an entotic  $\text{Ca}^{2+}$  channel that provides essential  $\text{Ca}^{2+}$  signaling, and shed light on the molecular mechanism underlying entosis that involves SEPTIN filaments, Orai1, and MLCK.

In the second part, I explored the mechanism underlying cytoskeletal defects during virus infection, focusing on their implications in ciliopathy. Coronaviruses target ciliate cells causing the loss of cilia, acute rhinorrheas, and other ciliopathies. The loss of ciliary function may help the virus infect, replicate, and spread. However, the molecular mechanisms by which coronaviruses cause ciliary defects are still unclear. Herein I demonstrate how coronavirus infection and SARS-CoV-2 3CL protease induce cilia dysfunction by targeting a host protein septin that is required for the structure and function of cilia. Further, I demonstrate that coronaviruses and 3CL protease lead to the cleavage of several septin proteins (SEPT2, 6, and 9), producing cleaved obstructive fragments. Furthermore, ectopic expression of cleaved SEPT2 fragments shows defective ciliogenesis, disoriented septin filaments, and ablated Sonic Hedgehog (SHH) signaling in a protease activity-dependent manner. I present that the 3CLpro inhibitors are potent and prevent abnormal ciliary structures and SHH signaling. These results provide useful insights into the general mechanisms underlying ciliary defects caused by coronaviruses, which in turn facilitate virus spread and prove that preclinical and clinical 3CL protease inhibitors may prove useful as therapeutics for treating ciliary defects of coronaviruses.



## Contents

|  |    |
|--|----|
| Abstract.....  | 1  |
| List of Figures.....   | 4  |
| Abbreviations.....   | 6  |
| Part 1. Orai1 is an entotic Ca <sup>2+</sup> channel for non-apoptotic cell death, entosis in cancer development... 7    |    |
| 1.1 Introduction.....  | 7  |
| 1.2. Materials and Methods.....  | 10 |
| 1.3. Results.....  | 15 |
| 1.3.1. Spontaneous Ca <sup>2+</sup> oscillations occur during entosis. ....  | 15 |
| 1.3.2. Spontaneous Ca <sup>2+</sup> oscillations occur mainly in the early to mid-engulfment stage.....                  | 17 |
| 1.3.3. Extracellular Ca <sup>2+</sup> regulates intracellular Ca <sup>2+</sup> level for entosis. ....                   | 18 |
| 1.3.4. SOC channel blockers prevent entosis.....   | 19 |
| 1.3.5. Entotic cells show polarized membrane Ca <sup>2+</sup> signals. ....  | 20 |
| 1.3.6. IP <sub>3</sub> related store depletion could induce entotic Ca <sup>2+</sup> signaling.....                      | 22 |
| 1.3.7. Genetic deletion of <i>Orai1</i> using CRISPR-Cas9 system. ....   | 24 |
| 1.3.8. Orai1 is the entotic Ca <sup>2+</sup> channel. ....   | 26 |
| 1.3.9. Orai1 has the differential distribution following entosis stage. ....   | 28 |
| 1.3.10. Orai1 shows the polarized distribution in invading cells.....  | 29 |
| 1.3.11. SEPTIN inhibitor suppresses entosis.....   | 31 |
| 1.3.12. SEPT2 co-localizes with Orai1.....   | 31 |
| 1.3.13. SEPT2 organizes the distribution of Orai1 in invading cells.....   | 33 |
| 1.3.14. MLC phosphorylation is induced by Orai1 at invading cell distal region and peripheral junction.....              | 35 |
| 1.3.15. Local entotic Ca <sup>2+</sup> signaling of Orai1 induces the local phosphorylation of MLC.....                  | 37 |
| 1.4. Discussion.....   | 40 |
| Part 2. Human coronavirus 3CL proteases cleave Septins and disrupt Hedgehog signaling, causing ciliary dysfunction. .... | 42 |
| 2.1. Introduction.....   | 42 |
| 2.2. Materials and Methods.....  | 45 |
| 2.3. Results.....  | 50 |
| 2.3.1. Coronavirus infection and 3CL Proteases cleave septins.....   | 50 |
| 2.3.2. Emerging coronaviruses are more potent at cleaving SEPT2.....   | 53 |



|   |    |
|---|----|
| 2.3.3. A single cleavage site of 3CL proteases is located at Q340 in SEPT2 and Q80 in SEPT6.  | 55 |
| 2.3.4. 3CLpro affects the septin complex by cleaving several septin proteins.   | 56 |
| 2.3.5. Cleaved SEPT2 NT affects the SEPT2 filament formation in non-ciliated RPE1 cells.  | 57 |
| 2.3.6. The cleaved SEPT2 NT interferes with septin filaments by forming homo- and heteromeric complexes with SEPT members in non-ciliary hRPE1 cells. | 59 |
| 2.3.7. The cleaved SEPT2 NT and CT affect ciliogenesis.   | 60 |
| 2.3.8. Mislocated SEPT2 fragments disturb SEPTs translocation into cilia.   | 62 |
| 2.3.9. 3CLpro reduces ciliary septins and induces primary cilia defects.  | 64 |
| 2.3.10. Coronavirus infection shows deciliation and SEPT2 reduction in cilia.   | 66 |
| 2.3.11. Pre-ciliated cells show more severe ciliary defects, mediated by the cleaved SEPT2.   | 68 |
| 2.3.12. Coronavirus infection and 3CLpro affect SHH signaling in ciliary cells.   | 71 |
| 2.4. Discussion   | 75 |
| References  | 79 |

## List of Figures

|  |    |
|--|----|
| Figure 1. Entosis during cancer development. ....  | 7  |
| Figure 2. Orai1 mediated $Ca^{2+}$ signaling. ....   | 8  |
| Figure 3. Spontaneous $Ca^{2+}$ oscillations occur during entosis. ....  | 16 |
| Figure 4. Spontaneous $Ca^{2+}$ oscillations occur mainly in the early to mid-engulfment stage. ....   | 17 |
| Figure 5. Extracellular $Ca^{2+}$ regulates intracellular $Ca^{2+}$ level for entosis. ....  | 19 |
| Figure 6. SOC channel blockers prevent entosis. ....   | 20 |
| Figure 7. Entotic cells show polarized membrane $Ca^{2+}$ signals. ....  | 21 |
| Figure 8. $IP_3$ related store depletion could induce entotic $Ca^{2+}$ signaling. ....  | 23 |
| Figure 9. Genetic deletion of Orai1 using CRISPR-Cas9 system. ....   | 25 |
| Figure 10. Orai1 is the entotic $Ca^{2+}$ channel. ....  | 27 |
| Figure 11. Orai1 has the differential distribution following entosis stage. ....   | 28 |
| Figure 12. Orai1 shows the polarized distribution in invading cells. ....  | 30 |
| Figure 13. SEPTIN inhibitor suppresses entosis. ....   | 31 |
| Figure 14. SEPT2 co-localizes with Orai1. ....   | 32 |
| Figure 15. SEPT2 organizes the distribution of Orai1 in invading cells. ....   | 34 |
| Figure 16. MLC phosphorylation is induced by Orai1 at invading cell distal region and peripheral junction. ....  | 36 |
| Figure 17. Local entotic $Ca^{2+}$ signaling of Orai1 induces the local phosphorylation of MLC. ....   | 38 |
| Figure 18. Intracellular $Ca^{2+}$ signaling regulates entosis via SEPTIN-Orai1- $Ca^{2+}$ /CaM-MLCK-actomyosin axis. ....                                     | 39 |
| Figure 19. Coronavirus life cycle stages and antiviral drug targets. ....  | 42 |
| Figure 20. Coronavirus infection and 3CL Proteases cleave septins. ....  | 52 |
| Figure 21. Emerging coronaviruses are more potent at cleaving SEPT2. ....  | 54 |
| Figure 22. A single cleavage site of 3CL proteases is located at Q340 in SEPT2 and Q80 in SEPT6. ....  | 55 |
| Figure 23. 3CLpro affects the septin complex by cleaving several septin proteins. ....   | 57 |
| Figure 24. Cleaved SEPT2 NT affects the SEPT2 filament formation in non-ciliated RPE1 cells. ....  | 58 |
| Figure 25. The cleaved SEPT2 NT interferes with septin filaments by forming homo- and heteromeric complexes with SEPT members in non-ciliary hRPE1 cells. .... | 60 |
| Figure 26. The cleaved SEPT2 NT and CT affect ciliogenesis. ....   | 61 |
| Figure 27. Mislocated SEPT2 fragments disturb SEPTs translocation into cilia. ....   | 63 |
| Figure 28. 3CLpro reduces ciliary septins and induces primary cilia defects. ....  | 65 |
| Figure 29. Coronavirus infection shows deciliation and SEPT2 reduction in cilia. ....  | 67 |
| Figure 30. Pre-ciliated cells show more severe ciliary defects, mediated by the cleaved SEPT2. ....  | 70 |

Figure 31. Coronavirus infection and 3CLpro affect SHH signaling in ciliary cells..... 73

Figure 32. Coronavirus 3CLprotease targets septins in cilia. .... 75

Figure 33. Prediction of cleavage sites of some SHH signaling molecules..... 77

## Abbreviations

2-APB: 2-Aminoethoxydiphenyl Borate  
AcTub: Acetylated Tubulin  
AJ: Adherens Junction  
CaM: Calmodulin  
CIC: Cell-In-Cell  
CRAC: Calcium Release Activated Calcium  
CRISPR: Clustered Regularly Interspaced Short Palindromic Repeats  
DBHQ: 2,5-Di-tert-butylhydroquinone  
EGF: Epidermal Growth Factor  
ER: Endoplasmic Reticulum  
IP<sub>3</sub>: Inositol 1,4,5-trisphosphate  
MLC: Myosin Light Chain  
MLCK: Myosin Light Chain Kinase  
PIP<sub>2</sub>: Phosphatidylinositol 4,5-bisphosphate  
PJ: Peripheral Junction  
PM: Plasma Membrane  
pMLC: Phospho-Myosin Light Chain  
ROCK: Rho-associated Protein Kinase  
SERCA: Sarco/Endoplasmic Reticulum Ca<sup>2+</sup> ATPase  
SOCE: Store-Operated Ca<sup>2+</sup> Entry  
STIM1: Stromal Interaction Molecule 1  
TG: Thapsigargin  
TTBK2: Tau Tubulin Kinase 2

# Part 1. Orai1 is an entotic $\text{Ca}^{2+}$ channel for non-apoptotic cell death, entosis in cancer development.

## 1.1 Introduction

Entosis, a non-apoptotic cell death process, engulfs homotypic living cells(1). Although it was first observed over 100 years ago, the underlying mechanisms and functional consequences have been studied in recent years. Entosis is triggered by several physiological conditions such as matrix detachment, aberrant mitosis(2), and glucose deprivation(3) (Figure 1). These various pathways for entosis reflect the characteristics of cancer cells, such as abnormal proliferation, anchorage-independence, and metabolic stress, suggesting that intrinsic properties of cancer cells or their microenvironments, can cause entosis. It is associated with a wide range of human diseases, such as genome instability(4, 5), developmental disorders(6, 7), and cancer(8).

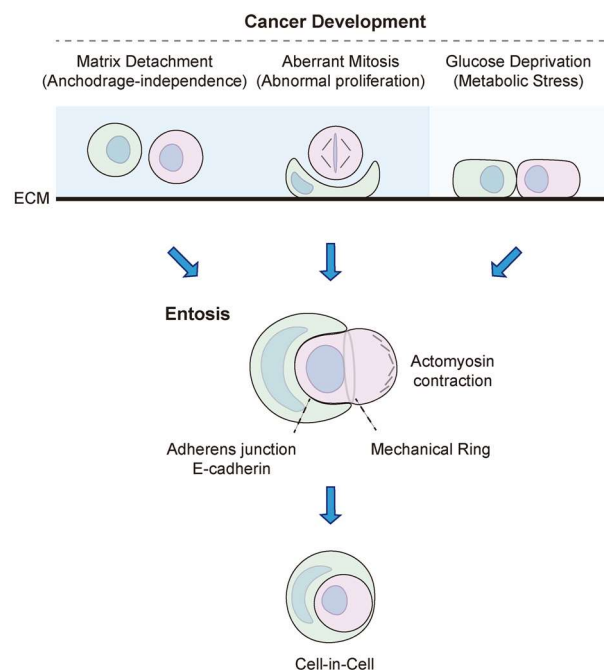


**Figure 1. Entosis during cancer development.**

Entosis is triggered by matrix detachment, aberrant mitosis, and glucose deprivation. Entotic cells engulf each other through adherens junction, mechanical ring, and actomyosin contraction. Consequently, they make a cell-in-cell structure.

Regardless of the mechanism by which entotic cells initiate, they form adherens junctions (AJs) via  $\text{Ca}^{2+}$ /E-cadherins(9). Following the formation of AJs, they are engulfed through actin polymerization following AJ(10), mechanical ring(11), and actomyosin contraction(1, 9). Lastly, they appear in cell-in-cell (CIC) structures, resulting in inside cells escaping and dividing, although they typically die via lysosomal degradation(12).

Engulfing (outer, host, winner) and invading (inner, internalizing, engulfed, loser) entotic cells form CIC structures through actin polymerization and myosin contraction. Invading cells have higher stiffness with accumulated actomyosin in the cell cortex, opposite to AJ, and the resulting mechanical tension drives CIC invasion. It is regulated by RhoA, Rho-associated protein kinase (ROCK), and diaphanous-related formin 1(Dia1)(13, 14). Engulfing cells have lower tension than invading cells and swallow neighboring cells with actin-dependent engulfment activity. Rac1, a key mediator of the actin cytoskeleton, and KRas, the oncogene regulating Rac1 activity, enhance engulfing by regulating actomyosin contractility(13).

Cytosolic  $\text{Ca}^{2+}$  function as intracellular signaling messengers and are involved in cytoskeleton rearrangement, metastasis, metabolism, cell death, and cancer development(15-18). An important mechanism for maintaining intracellular  $\text{Ca}^{2+}$  levels is Store-operated  $\text{Ca}^{2+}$  entry (SOCE), which is mediated by Orai1  $\text{Ca}^{2+}$  channels in plasma-membrane (PM)(19, 20) and Stromal Interaction Molecule (STIM) proteins in the endoplasmic reticulum (ER)(21). STIM senses ER  $\text{Ca}^{2+}$  concentrations and accumulates at ER-PM junctions following ER  $\text{Ca}^{2+}$  depletion, activating Orai1 channels in adjacent PM.  $\text{Ca}^{2+}$  entry through Orai1 channels is associated with several cell signaling processes in most cells(22, 23) (Figure 2).

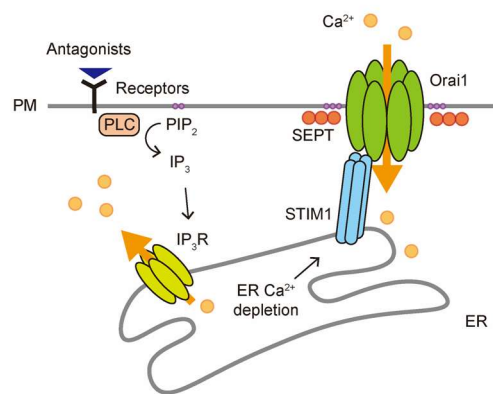


**Figure 2. Orai1 mediated  $\text{Ca}^{2+}$  signaling.**

STIM1 senses ER  $\text{Ca}^{2+}$  depletion and accumulates at ER-PM junctions, activating Orai1 in PM. Orai1-STIM1 interactions are regulated by SEPTINs.

Orai1-STIM1 assembly and stability, and architecture of ER-PM junctions, are determined by specific protein and lipid components including SEPTINs, PIP2, and proteins scaffolding ER to PM(24, 25). SEPTINs, filament forming GTPases, bind to inner PM through specific interactions with PIP2 and assemble on membrane domains(26-28). They promote stable recruitment of Orai1 by maintaining PIP2 organization in PM(29). Their loss results in abnormal Orai1 clustering and reduced SOCE.

MLC phosphorylation is essential for entosis providing contractile force. It is determined by myosin light chain kinase (MLCK), ROCK, and MLC phosphatase. MLCK, the best-studied factor regulating MLC phosphorylation, is  $Ca^{2+}$ /CaM-dependent serine/threonine kinase and is activated by CaM in response to an increase in intracellular  $Ca^{2+}$  levels. Activated MLCK phosphorylates the regulatory myosin light chains of myosin II (MLC2), specifically at serine-19, facilitating actin-activated myosin and promoting myosin-driven contraction.

Extracellular  $Ca^{2+}$  is required for E-cadherin-mediated cell junction formation during entosis. However, the role of intracellular  $Ca^{2+}$  signaling in entosis, and the mechanism through which it is modulated, remain poorly understood. Entosis-associated molecular pathways are  $Ca^{2+}$ -dependent. Orai1, a major  $Ca^{2+}$  route, regulates diverse processes related to entosis. For example,  $Ca^{2+}$  influx through Orai1 controls actin organization and dynamics at the immune synapse in T lymphocytes(30), membrane blebs in amoeboid cells(31), and leading-edge in migrating cells(32, 33). Orai1-dependent signaling enhances contractile force by regulating actomyosin reorganization(22, 34). Furthermore, entosis-associated proteins, including actin, MLC, Ezrin(31), Rac1(33), AMPK, and vinculin(22) are regulated by Orai1 or Orai1 mediating  $Ca^{2+}$  signals. I hypothesized that Orai1 is a major route for  $Ca^{2+}$  influx during entosis.

Here, I provide evidence that Orai1 is an entotic  $Ca^{2+}$  channel, whose membrane localization is tightly controlled by SEPTINs, resulting in temporal entotic  $Ca^{2+}$  oscillations that affect MLCK-actomyosin rearrangement during entosis. I identify the mechanism through Orai1-mediated  $Ca^{2+}$  signaling regulates  $Ca^{2+}$  dependent engulfment during entosis and provide insights into a therapeutic target for entotic regulators promoting entosis-mediated tumor development.

## 1.2. Materials and Methods

### 1.2.1. Cell Lines and cell culturing

MCF7 and HEK293T cells were cultured in Dulbecco's Modified Eagle Medium (DMEM) supplemented with 10% fetal bovine serum (FBS) at 37 °C and 5% CO<sub>2</sub>. For transient transfection, the cells were transfected at 70% confluency with 0.2–1 µg DNA using Lipofectamine 3000 (Invitrogen) or jetprime (PolyPlus) according to the manufacturer's instructions.

### 1.2.2. Cell internalization assays and entosis quantification

MCF7 cells were cultured for at least three days before the experiment. Monolayer cells were trypsinized to a single-cell suspension and washed briefly with phosphate buffered saline (PBS). Suspended cells (1–2 x 10<sup>5</sup> cells/ml) were cultured in the indicated conditions (Ca<sup>2+</sup> chelation, chemical treatment) for 2–6 h on polyHEMA coated plates (1). Cells were pelleted at the indicated times, washed in PBS, and fixed in 4% PFA for 10 min at 25 °C. Fixed samples were washed in PBS and stained with Alexa Fluor™ 594 Phalloidin (Invitrogen, A12381), WGA-488 (Invitrogen, W11261), and Hoechst 33342 (Invitrogen, H3570) for 30 min at 25 °C. To confirm that MCF7 cells were completely internalized by entosis, the cells were examined under a laser-scanning confocal microscope LSM780 (NLO; Zeiss). Prior to heparin treatment, cells were permeabilized by saponin (10 µg/ml).

The percentage of entotic cells was determined by quantifying the number of single cells and cell-in-cell structures. Cells wrapped at least half-way around neighboring cells were considered to be undergoing entosis. Cell pairs participating in entosis (engulfing and invading cell) were counted as one.

The following Chemicals were used. EGTA (Biopure, 4725E), GdCl<sub>3</sub> (Gadolinium (III) Chloride) (Sigma-Aldrich, 439770), AnCoA4 (Sigma-Aldrich, 532999), YM58483 (Cayman Chemical Company, 13246), SKF96365 (Cayman Chemical Company, 10009312), 2-APB (Cayman Chemical Company, 17146), Heparin (Sigma-Aldrich, H3149), Xestospongine C (Calbiochem, 682160), saponin (Sigma-Aldrich, S7900), Forchlorfenuron (Acros, 45629), ML-9 (Cayman Chemical Company, 10010236), and Peptide-18 (Cayman Chemical Company, 19181), Thapsigargin (Cayman Chemical Company, 10522).

### 1.2.3. Live cell imaging of cell-in-cell structures in soft agar

To track entosis, cells (2 x 10<sup>5</sup> cells/ml) were embedded in growth media containing 0.3% low melting agarose and plated on micro-insert 4 wells in polymer coverslip bottom dishes (ibidi, 80406) coated with polyHEMA. The dishes were centrifuged at 1300 rpm for 1 min and then incubated at 37 °C for



20–30 min to allow the cells to settle down. Time-lapse microscopy was performed at 37 °C and 5% CO<sub>2</sub> in live-cell incubation chambers.

To analyze entosis time-lapse progression, fluorescence and differential interference contrast (DIC) images were obtained every 3 s – 5 min for the indicated time courses on a LSM780 (Zeiss) confocal microscope with Zeiss Plan-Apochromat 63x/1.4 Oil objective lens. mCherry and eGFP (GCaMP6s) were simultaneously excited at 594 nm and 488 nm, respectively. Fluorescence emission was collected at 615–840 nm (mCherry) and 510–570 nm (eGFP). Zen software (Zeiss) was used for image acquisition. Images were analyzed using Zen or ImageJ software.

Graphs showing low pass filtered normalized GCaMP6s intensity were generated. Raw signals were converted into values relative to the baseline ( $\Delta F/F$ , where F is the baseline level). Entotic cell pairs consisting of engulfing and invading cells were counted as one. Ca<sup>2+</sup> levels 3 – 5x above the standard deviation were recorded as Ca<sup>2+</sup> signals. The time point at which a complete CIC structure was created was set to 0. The 60 – 0 min period, before complete cell internalized, was defined as “engulfment”. The period from 0 to 60 min after generating the CIC structures, was defined as “Cell-in-Cell”.

#### **1.2.4. Immunofluorescence assay**

Monolayer cells were trypsinized to a single-cell suspension and grown on polyHEMA-coated plates. Cells were pelleted 2.5 h later and seeded on poly-ornithine (Sigma-Aldrich, P3655)-coated cover glass for 10 min. After 10 min, the cells were fixed with 4% paraformaldehyde for 10 min, permeabilized with 0.02–0.1% Triton X-100 in PBS for 10 min at 25 °C, and then blocked with 3% bovine serum albumin (BSA) in PBS for 30 min. After incubating with the indicated antibody for 2–4 h at 25 °C or overnight at 4 °C, the cells were incubated with a conjugated secondary antibody at 25 °C for 1 h. For staining plasma membrane, the cells were incubated with CellBrite Red Cytoplasmic Membrane Dyes (Biotium, 30023) at 25 °C for 10 min. For staining cytosol, the cells were incubated with CellTracker Red Dyes (Invitrogen, C34552) at 25 °C for 10 min. For staining F-actin, the cells were incubated with Alexa Fluor™ 594 Phalloidin (Invitrogen, A12381) at 25 °C for 10 min. Finally, the nuclei were stained with Hoechst 33342 (Molecular Probes) for 10 min. Confocal fluorescence images were acquired using LSM780 confocal microscope (NLO; Zeiss) and LSM980 (Zeiss) with a Zeiss 63x and 100x oil objective lens (NA 1.4 and 1.46, respectively).

#### **1.2.5. Lentivirus-mediated stable cell line construction.**

HEK293T cells were plated into 12-well plates. The cells were transfected with lentiviral constructs together with packaging plasmids (VSVg, p8.2). Supernatants were collected 48 h post-transfection. MCF7 cells were infected with 100–500  $\mu$ l of lentivirus-containing medium and incubated for 48 h.

### 1.2.6. Generation of the knock-out cell lines

MCF7 *Orai1* knockout cells were made with a CRISPR-Cas9 system. Guide RNA sequences for human *Orai1* (sense 5'-GATCGGCCAGAGTTACTCCGAGG-3' and antisense 5'-CCTCGGAGTAACTCTGGCCGATC-3') were inserted into the pRGEN vector and pRGEN-reporter (ToolGen). MCF7 cells were transfected with pRGEN-*Orai1*, pRGEN-Cas9 and pRGEN-report using Lipofectamine 3000 (Invitrogen), according to the manufacturer's instructions. After two days, transfected cells were selected with 200 µg/mL hygromycin (PhytoTechnology Laboratories, ACR0397045A) for seven days. Cell colonies were isolated after 2–3 weeks. To check for genome editing, the region surrounding the target site of the guide RNA was amplified using PCR (forward primer: 5'-ATGCATCCGGAGCCCGCCCCGCCCCGAGC-3' and reverse primer: 5'-CATGGCGAAGCCGGAGAGCAG-3'). PCR products were subsequently purified via agarose gel extraction and then sequenced. Sequencing of PCR fragments from the *Orai1* KO MCF7 cells revealed 1 base-pair deletion confirming successful *Orai1* KO. (KO#1: 12 base-pair deletion, KO#2: base-pair deletion, KO#3: 2 base-pair insertion). Protein expression was confirmed using Western blot analysis. For immunofluorescence assay, CelltrackerRed (Invitrogen, C34552) was used for labeling *Orai1* KO cells.

### 1.2.7. Total RNA extraction, cDNA synthesis and reverse transcription-PCR

Total RNA was extracted from the isolated cells using RiboEX (GeneAll) following the manufacturer's protocol. cDNA was synthesized from 1 µg of RNA using oligo (dT) primers and First Strand cDNA Synthesis Kit (TOYOBO). PCR amplification was conducted on the C1000 Touch thermal Cycler (Bio-Rad) using the following amplification conditions: initial denaturation at 95 °C for 3 min and then 35–45 cycles of denaturation at 95 °C for 30 s, annealing at 55 °C for 30 s, and extension at 72 °C for 1 min; an additional extension at 72 °C for 10 min, 16 °C hold. PCR products were subsequently purified via agarose gel extraction. Primers: h.STIM1 For: 5-AAGGCATTACTGGCGCTGAACCATGG-3, Rev: 5-ACGGGAAGAATCCAAATGTGGAGAGC-3, h.STIM2 For: 5-AACGCTGAAATGCAGCTAGCTATTGC-3 Rev: 5-CGTTCTCGTAAACAAGTTGTCAACTC-3, h.Orai2 For: 5-GGCCATGGTGGAGGTGCAGCTGGAG-3 Rev: 5-GAGTTCAGGTTGTGGATGTTGCT-3, h.Orai3 For: 5-TGGGTCAAGTTTGTGCCATTGG-3 Rev: 5-TGCTGCAGACGCAGAGGACCG-3, GAPDH For: 5-CTGAACGGGAAGCTCACTGGCATG-3 Rev: 5-AGGTCCACCACCCTGTTGCTGTAGC-3

### 1.2.8. Western blot analysis

Cells were scraped into ice-cold cell lysis buffer (50mM Tris-HCL pH 7.5, 150mM NaCl, 1% Triton X-100, 0.1% SDS), and lysed for 10 min on ice. Lysates were centrifuged at 12000rpm at 4 °C for 10 min. For soluble protein blotting, samples were mixed with 1/4 volume of 4x reducing sample buffer (200 mM Tris-HCl (pH6.8), 8% SDS, 0.4% bromophenol blue, 40% glycerol, and 20%  $\beta$ -mercaptoethanol) and boiled at 95 °C for 5 min. Samples were separated using 10% polyacrylamide SDS-PAGE and transferred onto 0.45  $\mu$ m pore size PVDF membranes (Immobilon-P, Millipore). The membrane was blocked with TBS-T plus 7% SKIM-milk and incubated overnight at 4 °C with primary antibodies diluted in TBS-T plus 3% BSA. Blots were incubated with horseradish peroxidase (HRP)-conjugated secondary antibodies and detected using enhanced chemiluminescence (Pierce). Densitometry analysis was performed using the ImageJ software (NIH).

### 1.2.9. Immunoprecipitation

HEK293T cells were transfected with the indicated constructs for 18 h. Transfected cells were washed three times with PBS and lysed with lysis buffer (50 mM Tris-HCl (pH 7.5), 150 mM NaCl, and 1% Triton X-100). Lysates were centrifuged at 12,000 rpm for 10 min and the supernatant was incubated overnight at 4 °C with anti-Flag M2 agarose beads (Sigma-Aldrich). Lysates and immunoprecipitated samples were run on SDS-PAGE gels, probed with horseradish peroxidase (HRP)-conjugated secondary antibodies, and detected by enhanced chemiluminescence (Thermo Fisher Scientific).

### 1.2.10. Antibodies and protein detection

Orai1 (Santa Cruz Biotechnology, SC-377281), Orai2 (Alomone, ACC-061), Orai3 (Alomone, ACC-065), STIM1 (Abnova, H00006786-M01), STIM2 (Cell Signaling Technology, 4917S), p-MLC2 (S19) (Cell Signaling Technology, 3671S), MLC (MilliporeSigma, M4401), GAPDH (proteintech, 60004-1-Ig),  $\beta$ -actin (proteintech, 66009-1-Ig; Santa Cruz Biotechnology, SC-47778), SEPT2 (proteintech, 60075-1-Ig; Novus Biologicals, NBP1-85212), FLAG (Sigma-Aldrich, F1804), GFP (MBL, 598)

### 1.2.11. Intracellular Ca<sup>2+</sup> Imaging

MCF7 cells were loaded with 1  $\mu$ M of Fluo-4 AM (Invitrogen) for 30 min at 37 °C. Ca<sup>2+</sup> imaging was performed in 0 or 2 mM Ca<sup>2+</sup> Ringer's solution with a IX81 microscope (Olympus) equipped with an Olympus  $\times$ 40 oil objective lens (NA 1.30) and with a fluorescent arc lamp (LAMDA LS), excitation filter wheel (Lambda 10-2; Sutter Instruments), stage controller (MS-2000; ASI), and a CCD camera

(C10600; Hamamatsu) at 25 °C. Images were processed with MetaMorph software (Molecular Devices) and analyzed with excel and GraphPad Prism 5. TG (Cayman Chemical Company, 10522, 1 $\mu$ M) was used for inducing ER Ca<sup>2+</sup> depletion. The changes in intracellular Ca<sup>2+</sup> were determined as mean variation between the Fluo-4 fluorescence intensities obtained during the stimulus (F) and the resting state (F0), as follows: F-F0.

### **1.2.12. Statistical analysis**

All generated data were recorded in Excel and analyzed using GraphPad Prism 5 software. Results are presented as means  $\pm$  SEM. The student's *t*-test was used to determine pairwise statistical significance. \*\*\**p* < 0.001; \*\**p* < 0.01; \**p* < 0.05.

## 1.3. Results

### 1.3.1. Spontaneous $\text{Ca}^{2+}$ oscillations occur during entosis.

$\text{Ca}^{2+}$  signaling drives intracellular processes and communicates between cells. Intracellular  $\text{Ca}^{2+}$  concentration exhibits diverse spatiotemporal dynamics, influencing the versatility of  $\text{Ca}^{2+}$ -dependent signaling (17). Hence, I investigated whether and how  $\text{Ca}^{2+}$  signaling, particularly  $\text{Ca}^{2+}$  channel-mediated  $\text{Ca}^{2+}$  dynamics, is required for entosis. To determine whether intracellular  $\text{Ca}^{2+}$  is necessary for entosis, I first measured the entosis efficiency in MCF7 cells treated with BAPTA-AM, a cell-permeable  $\text{Ca}^{2+}$  chelator. For entosis quantification, adherent MCF7 cells were trypsinized into single cells and cultured in suspension for 2–6 h under the indicated conditions ( $\text{Ca}^{2+}$  chelation or chemical treatment) (Figure 3A). Cells were fixed and stained for plasma membrane and nucleus. Analysis using confocal microscopy demonstrated the complete cell-in-cell structures (entotic cells). The percentage of entotic cells was determined through quantifying the number of single cells and cell-in-cell structures (Figure 3B). When I treated BAPTA-AM, the cells showed reduced entosis efficiency compared with cells in the  $\text{Ca}^{2+}$  medium, confirming that intracellular  $\text{Ca}^{2+}$  is required for entosis. The cells showed reduced entosis efficiency compared with cells in the  $\text{Ca}^{2+}$  medium (Figure 3C), confirming that intracellular  $\text{Ca}^{2+}$  is required for entosis.

To assess the effect of  $\text{Ca}^{2+}$  signaling on entosis progression, I measured intracellular  $\text{Ca}^{2+}$  concentrations in “engulfing” and “invading” entotic MCF7 cells expressing mCherry-GCaMP6s, a genetically encoded  $\text{Ca}^{2+}$  indicator (35). Time-lapse microscopy imaging was performed for 100 min at 3 – 5 min intervals in 0.3% low melting agarose as described (1) (Figure 3D). A  $\text{Ca}^{2+}$ -insensitive fluorophore, mCherry, ensured proper GCaMP6s expression and normalized GCaMP6s intensity.  $\text{Ca}^{2+}$  oscillations 1.5x above the standard deviation of the threshold of the GFP/mCherry fluorescence ratio were counted as  $\text{Ca}^{2+}$  signals. Interestingly, I observed spontaneous  $\text{Ca}^{2+}$  oscillations in most (90%) entosis proceeding cells in  $\text{Ca}^{2+}$  dependent manner (Figure 3E and G) as no oscillation occurred when extracellular  $\text{Ca}^{2+}$  was depleted with 2 mM EGTA (Figure 3F and G) and the efficiency of entosis was reduced in the absence of  $\text{Ca}^{2+}$  (35% to 1 %, Figure 3H). And there were no differences in  $\text{Ca}^{2+}$  oscillation between “Engulfing” and “Invading” cell pairs (Figure 3I-K), implying that both cells require intracellular  $\text{Ca}^{2+}$  signals to undergo entosis. These results suggest that extracellular  $\text{Ca}^{2+}$  is necessary for initiating entosis and for intracellular  $\text{Ca}^{2+}$  oscillations during entosis.

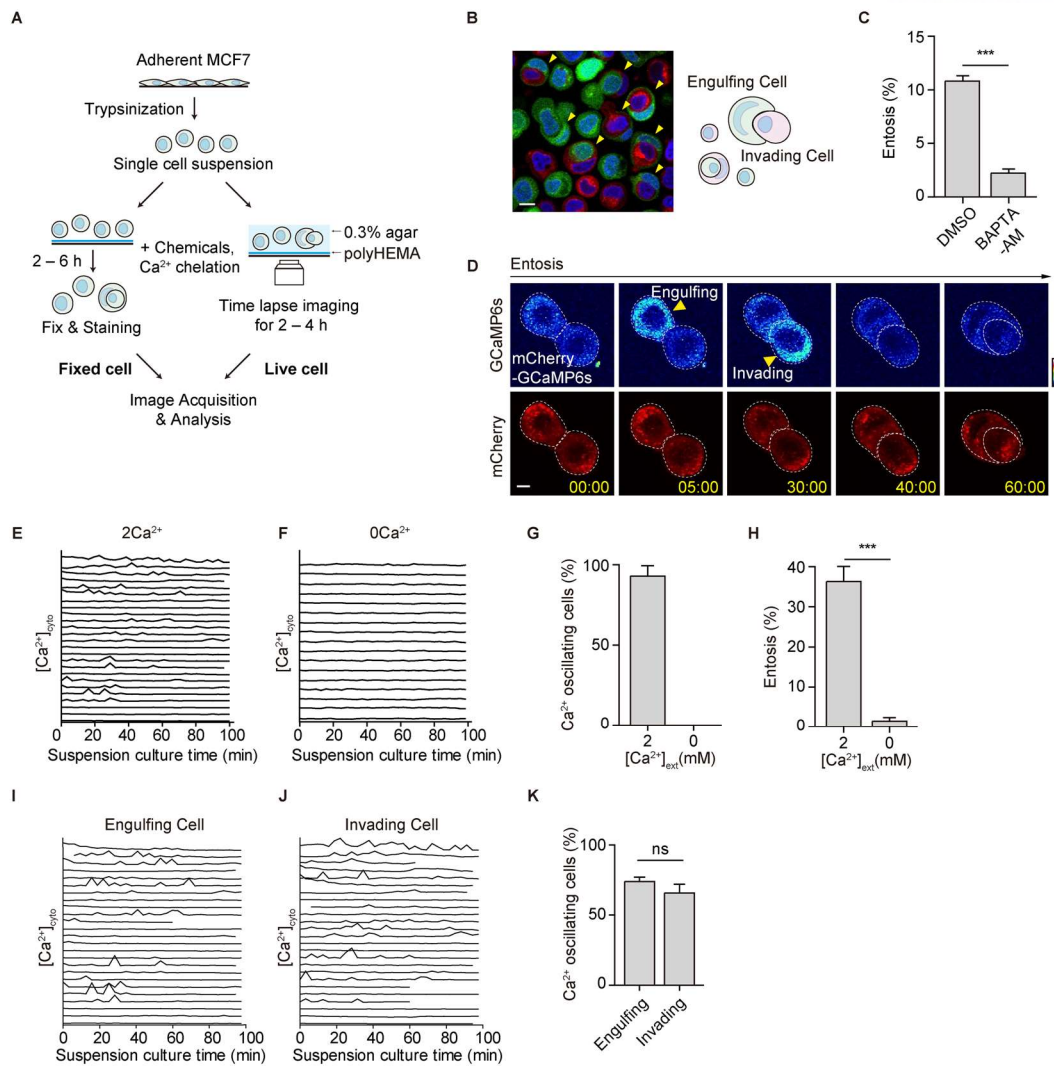


**Figure 3. Spontaneous  $\text{Ca}^{2+}$  oscillations occur during entosis.**

(A) Schematic representation of the method for quantifying and imaging entotic cells. (B) Representative images of entotic cells and a diagram of an entotic cell pair: engulfing and invading cells. Yellow arrowheads indicate entotic cells. Scale bar = 10  $\mu\text{m}$ . (C) Quantification of internalizing cells in BAPTA-AM (10  $\mu\text{M}$ , with 100  $\mu\text{M}$  of EGTA) after 6 h of suspension. Data represent mean  $\pm$  SEM of three independent experiments ( $n > 200$  cells). (D) Spontaneous  $\text{Ca}^{2+}$  oscillations in MCF7 cells during entosis. Yellow arrowheads indicate  $\text{Ca}^{2+}$  signals. Time is presented in minutes: seconds. Scale bar = 5  $\mu\text{m}$ . (E and F) Graph of normalized GCaMP6s ratio (GCaMP6s/mCherry) in entotic cell pairs exposed to 2 mM extracellular  $\text{Ca}^{2+}$  (E,  $n = 24$ ) and non-entotic cells exposed to 0 mM extracellular  $\text{Ca}^{2+}$  (2 mM EGTA) (F,  $n = 17$ ). (G) Quantification of  $\text{Ca}^{2+}$  oscillating cells from (E and F). (H) Quantification of internalizing cells cultured in suspension for 4 h in the presence of 2 mM and 0 mM  $\text{Ca}^{2+}$ . Data represent mean  $\pm$  SEM of triplicate experiments ( $n > 300$  for each cell line). (I and J) Graphs of normalized GCaMP6s ratio in engulfing (I) and invading (J) cells (From E,  $n > 22$ ). (K)

Quantification of  $\text{Ca}^{2+}$  oscillating cells from (G and H). Significance was determined using unpaired two-tailed  $t$ -test. ns, not significant. \*\*\* $p < 0.001$ .

### 1.3.2. Spontaneous $\text{Ca}^{2+}$ oscillations occur mainly in the early to mid-engulfment stage.

I explored entotic  $\text{Ca}^{2+}$  oscillation by analyzing the efficiency and time kinetics of the initiation of internalization and engulfment. Internalization occurred approximately 2 h after matrix detachment (Figure 4A) and was followed by engulfment for 30 to 60 min (Figure 4B and C). To elucidate temporal  $\text{Ca}^{2+}$  oscillation patterns during entosis, time points at which entotic cells formed complete CIC structures were set to 0. I monitored changes in  $\text{Ca}^{2+}$  concentrations in MCF7 cells expressing mCherry-GCaMP6s one hour before and after complete cell internalization at 3 s intervals (Figure 4D). Approximately 90% of entotic cells showed spontaneous  $\text{Ca}^{2+}$  oscillations, with non-synchronized patterns between engulfing and invading cells, before forming complete CIC structures (Figure 4D and E). Interestingly, I noticed that  $\text{Ca}^{2+}$  oscillations dramatically disappeared in entotic cells with complete CIC structure. These results indicated that  $\text{Ca}^{2+}$  oscillations might be temporally controlled during entosis, specifically during engulfment, rather than during most completed CIC structure stages.

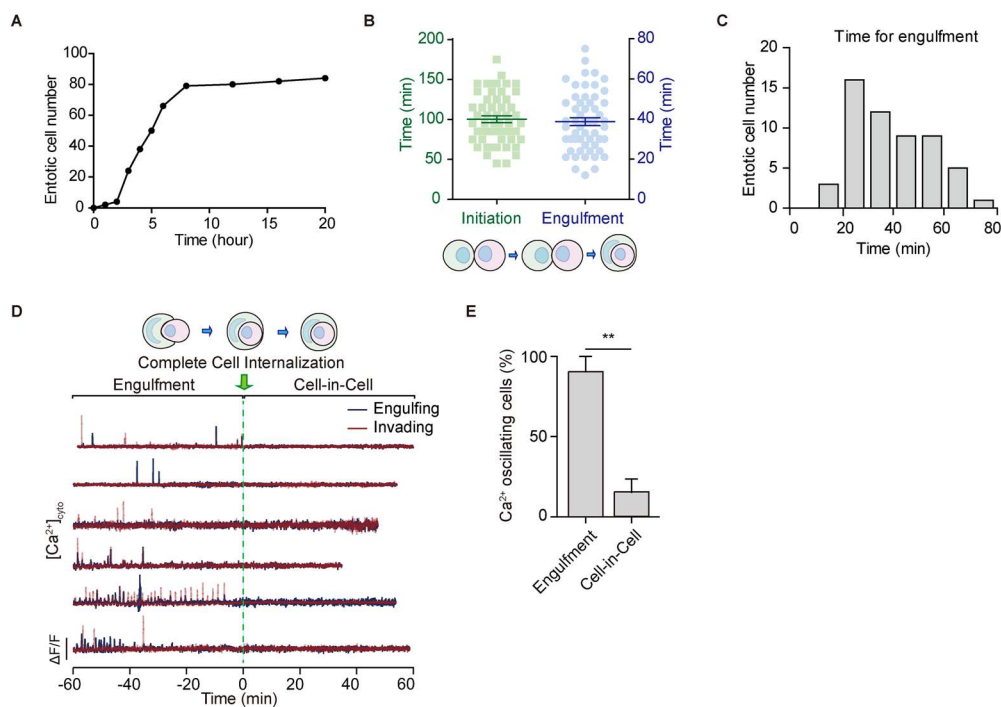


**Figure 4. Spontaneous  $\text{Ca}^{2+}$  oscillations occur mainly in the early to mid-engulfment stage.**

(A and B) (A) Quantification of entotic cells using time-lapse imaging conducted over 20 h (A,  $n = 84$ ). (B and C) Time to entosis initiation and engulfment. Engulfment was initiated after 1 - 2 h of suspension (B,  $n = 54$ ). Complete engulfment takes 30 - 60 min after the initiation (B and C,  $n = 55$ ). (D)



Spontaneous  $\text{Ca}^{2+}$  oscillations in MCF7 cells during entosis. Y axis: 4 (A.U.) (E) Quantification of  $\text{Ca}^{2+}$  oscillating cells during engulfment and CIC stages. The timepoint at which a complete CIC structure was made was aligned to 0. (Engulfment: -60-0 min, Cell-in-Cell: 0-60 min). Data represent mean  $\pm$  SEM of triplicate experiments (n=7, 6, and 5). Significance was determined using unpaired two-tailed *t*-test. ns, not significant. \*\**p* < 0.01.

### 1.3.3. Extracellular $\text{Ca}^{2+}$ regulates intracellular $\text{Ca}^{2+}$ level for entosis.

To determine whether intracellular  $\text{Ca}^{2+}$  oscillations depend on extracellular  $\text{Ca}^{2+}$ , I measured entosis efficiency and intracellular  $\text{Ca}^{2+}$  concentrations under various extracellular  $\text{Ca}^{2+}$  conditions. Both entosis efficiency (Figure 5A) and intracellular  $\text{Ca}^{2+}$  concentrations (Figure 5B) increased as extracellular  $\text{Ca}^{2+}$  concentrations increased from 0 to 2 mM, demonstrating that intracellular entotic  $\text{Ca}^{2+}$  oscillations are linked to extracellular  $\text{Ca}^{2+}$ .

To further confirm the effect of extracellular  $\text{Ca}^{2+}$  on entosis efficiency and intracellular  $\text{Ca}^{2+}$  concentrations, I performed “ $\text{Ca}^{2+}$  add-back” and “ $\text{Ca}^{2+}$  withdrawal” in entotic MCF7 cells. I induced entosis in 0 mM extracellular  $\text{Ca}^{2+}$  with  $\text{Ca}^{2+}$  chelator EGTA for 2 h of suspension culture and followed by in 2 mM  $\text{Ca}^{2+}$  medium for another 2 h. Entosis efficiency increased from 1% at 2 h to 9% at 4 h (Figure 5C). Intracellular  $\text{Ca}^{2+}$  concentrations increased approximately threefold after adding  $\text{Ca}^{2+}$  (Figure 5D). Replacing  $\text{Ca}^{2+}$  with EGTA (“ $\text{Ca}^{2+}$  withdrawal”) decreased entosis efficiency from 15% at 2 h to 4% at 4 h (Figure 5C), while efficiency increased from 15% to 30% in  $\text{Ca}^{2+}$  medium (Figure 5C). I observed similar changes in intracellular  $\text{Ca}^{2+}$  concentrations with  $\text{Ca}^{2+}$  withdrawal resulting in an approximately two-fold reduction in intracellular  $\text{Ca}^{2+}$  concentrations (Figure 5D). These results confirmed that extracellular  $\text{Ca}^{2+}$  influences entosis efficiency by regulating intracellular  $\text{Ca}^{2+}$  concentrations.

I then visualized how  $\text{Ca}^{2+}$  regulates the movement of entotic cells using mCherry-tagged LifeAct. Time-lapse imaging showed changes in movement and morphology of entotic cells. Half invading entotic cells continued to invade engulfed entotic cells, in the presence of 2 mM extracellular  $\text{Ca}^{2+}$ , resulting in CIC structures (Figure 5E). However, the cells began to emerge soon after inhibiting  $\text{Ca}^{2+}$  with EGTA (Figure 5F). Interestingly, I found that a pair of almost engulfed entotic cells (completed more than 90%) were not separated into individual cells even in 0 mM extracellular  $\text{Ca}^{2+}$  with 2 mM EGTA condition (Figure 5G) as proposed (11). It indicated that  $\text{Ca}^{2+}$  may be necessary for CIC attachment at the initial stage and  $\text{Ca}^{2+}$  oscillation in the middle stage, but less in the final stage.

Taken together, these results suggested that extracellular  $\text{Ca}^{2+}$  affects entosis efficiency by regulating oscillating intracellular  $\text{Ca}^{2+}$  signaling for regulating particular entosis stages.



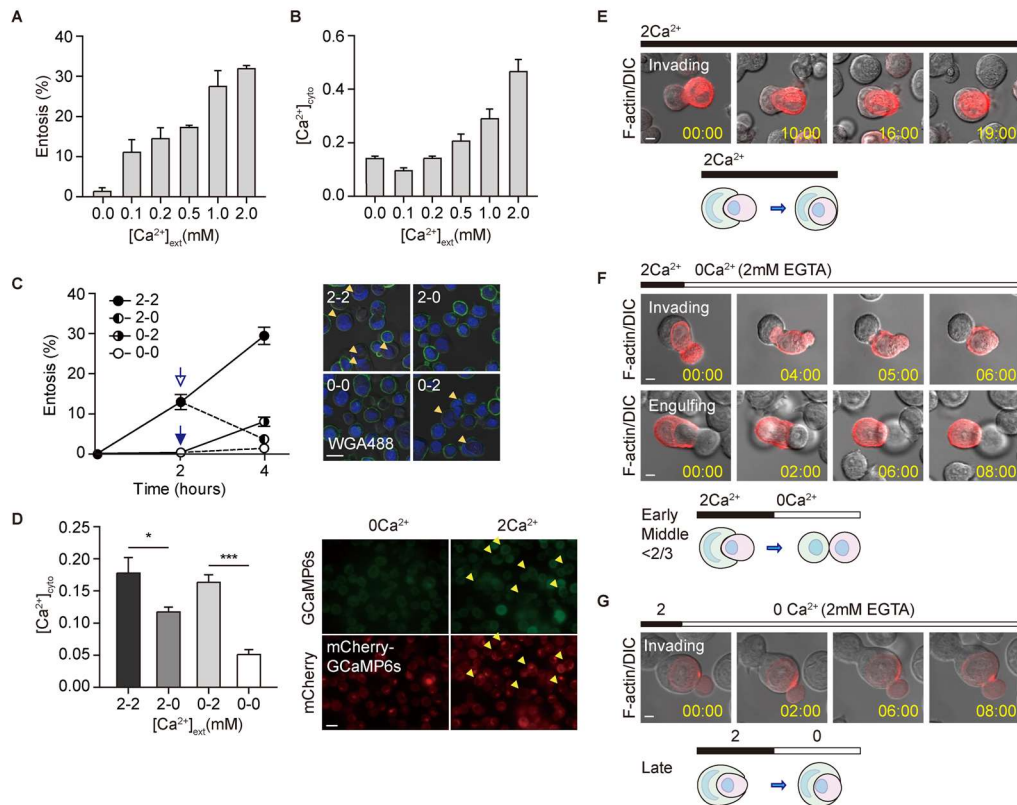


**Figure 5. Extracellular Ca<sup>2+</sup> regulates intracellular Ca<sup>2+</sup> level for entosis.**

(A and B) Quantification of internalizing cells depending on extracellular Ca<sup>2+</sup> concentration (A) and intracellular Ca<sup>2+</sup> level (GCaMP6s/mCherry) (B). Data represent mean ± SEM of triplicate experiments (n = 52 for each condition). (C) Quantification of internalizing cells depending on extracellular Ca<sup>2+</sup> concentration. Ca<sup>2+</sup> add-back (0 - 2) and Ca<sup>2+</sup> withdrawal (2 - 0). Data represent mean ± SEM of triplicate experiments (n > 200 for each cell line). Scale bar = 20 μm. (D) Graph of normalized GCaMP6s ratio (GCaMP6s/mCherry). Data represent mean ± SEM. n= 74, 42, 38, 33 for each group. Scale bar = 20 μm. (E, F and G) Time-lapse images of entotic cells in the presence of Ca<sup>2+</sup> (E) and under Ca<sup>2+</sup> withdrawal (2 → 0 mM and addition of 2 mM EGTA) (F and G). Cherry-Lifect labeled cell morphology. Scale bar = 5 μm. Significance was determined using unpaired two-tailed *t*-test. \*\*\**p* < 0.001; \**p* < 0.05.

### 1.3.4. SOC channel blockers prevent entosis.

It was surprising to find that no reports have been found regarding Ca<sup>2+</sup> channels that are associated with entosis. Thus, I explored which Ca<sup>2+</sup> channels regulate entotic Ca<sup>2+</sup> signaling for entosis. To find out potential Ca<sup>2+</sup> channels, suspended MCF7 were treated with gadolinium (Gd<sup>3+</sup>), an inorganic Ca<sup>2+</sup> channel blocker for 3 h and showed a decreased entosis efficiency (Figure 6A), indicating the

involvement of  $\text{Ca}^{2+}$  channels in entosis. In cancer cells, SOC (Orai) channels are best known for major  $\text{Ca}^{2+}$  channels. Therefore, MCF7 cells were treated with SOC channel blockers, 2-APB, SKF96365, and YM58483 for 4 h and showed reduced entosis efficiency from 35% to 20% (Figure 6B), indicating that SOC  $\text{Ca}^{2+}$  channels might be an unrevealed  $\text{Ca}^{2+}$  channel of entosis. I further analyzed the change in  $\text{Ca}^{2+}$  oscillations in MCF7 cells with the blockers. The number of  $\text{Ca}^{2+}$  oscillating cells decreased by 45 % in the presence of SOC channel blockers compared with DMSO (about 65%, Figure 6C). The amplitude of intracellular  $\text{Ca}^{2+}$  transients also decreased (Figure 6D). These results provide the first evidence that SOC channels are entotic  $\text{Ca}^{2+}$  channels that can induce  $\text{Ca}^{2+}$  oscillations.

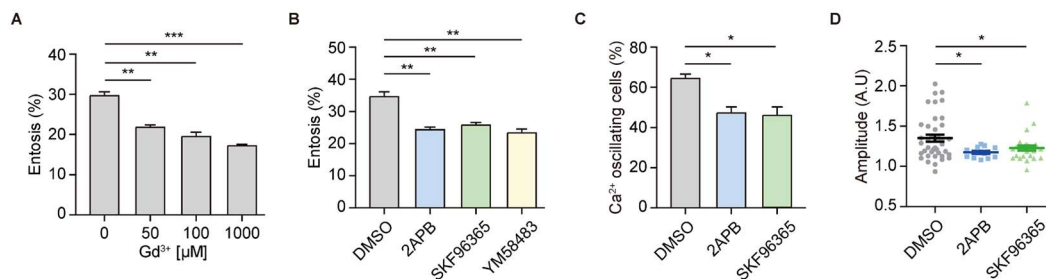


**Figure 6. SOC channel blockers prevent entosis.**

(A) Bar graph showing entosis efficiency after 3 h. Entotic cells were quantified with  $\text{Gd}^{3+}$  in the dose-dependent manner. Data represent mean  $\pm$  SEM of triplicate experiments ( $n > 200$  for each). (B) Quantification of entotic cells in SOC channel blockers; 2-APB (50  $\mu\text{M}$ ), SKF96365 (10  $\mu\text{M}$ ), YM58483 (10  $\mu\text{M}$ ) compared with the control (DMSO). Cell suspensions were cultured with each inhibitor for 4 h. Data represent mean  $\pm$  SEM of the triplicate experiments ( $n > 300$  in each experimental group). (C) Quantification of  $\text{Ca}^{2+}$  oscillating cells in DMSO, 2-APB, and SKF96365 from (Figure S4). Higher  $\text{Ca}^{2+}$  levels, defined by setting the threshold to 1.5x above the standard deviation, were counted as  $\text{Ca}^{2+}$  signals ( $n = 28, 19,$  and  $24$ ). (D) Quantitative comparisons of spontaneous  $\text{Ca}^{2+}$  signals measured using GCaMP6s (GCaMP6s/mCherry). The compared quantities are peak amplitudes  $\Delta\text{F}/\text{F}$  ratios. Data represent mean  $\pm$  SEM. Significance was determined using unpaired two-tailed  $t$ -test. \*\*\* $p < 0.001$ ; \*\* $p < 0.01$ ; \* $p < 0.05$ .

### 1.3.5. Entotic cells show polarized membrane $\text{Ca}^{2+}$ signals.

$\text{Ca}^{2+}$  concentrations of entotic  $\text{Ca}^{2+}$  oscillating cells were enriched in the PM of both invading as well as engulfing cells (Figure 3D), thus, I analyzed spatially localized  $\text{Ca}^{2+}$  signaling during entosis using mCherry-GCaMP6s-CAAX, a PM-localized  $\text{Ca}^{2+}$  indicator. Examining the localization and  $\text{Ca}^{2+}$  responsiveness of mCherry-GCaMP6s-CAAX in MCF7 cells showed restricted local  $\text{Ca}^{2+}$  influx without  $\text{Ca}^{2+}$  release from depleted stores (Figure 7A and B), indicating that GCaMP6s-CAAX can

measure  $\text{Ca}^{2+}$  changes near PM. To investigate entotic membrane  $\text{Ca}^{2+}$  signaling in detail, I performed time-lapse imaging. In MCF7 cells expressing mCherry-GCaMP6s-CAAX, the spontaneous  $\text{Ca}^{2+}$  oscillations were PM-enriched and spatially localized in both engulfing and invading entotic cells (Figure 7C, D, F), which is similar to the results of GCaMP6s a cytosolic  $\text{Ca}^{2+}$  indicator, during engulfment (Figure 4C).

I further analyzed the concentration of membrane  $\text{Ca}^{2+}$  of engulfing and invading cells. Interestingly, not only a change in the local  $\text{Ca}^{2+}$  distribution but also a differential local distribution was observed between invading and engulfing cells during engulfment. In engulfing cells. Local  $\text{Ca}^{2+}$  concentrations were higher at CC (cell-cell contact site) than at the distal membranes (engulfing cell distal region, ED) (Figure 7D and E). However, invading cells had a higher level of  $\text{Ca}^{2+}$  at the cell cortex of the distal membrane (invading cell distal region, ID) and lower local  $\text{Ca}^{2+}$  concentrations at the CC (Figure 7F and G). These results provide the first evidence that differential  $\text{Ca}^{2+}$  signaling in entotic cell pairs is required for proper cellular signaling and organization during entosis.

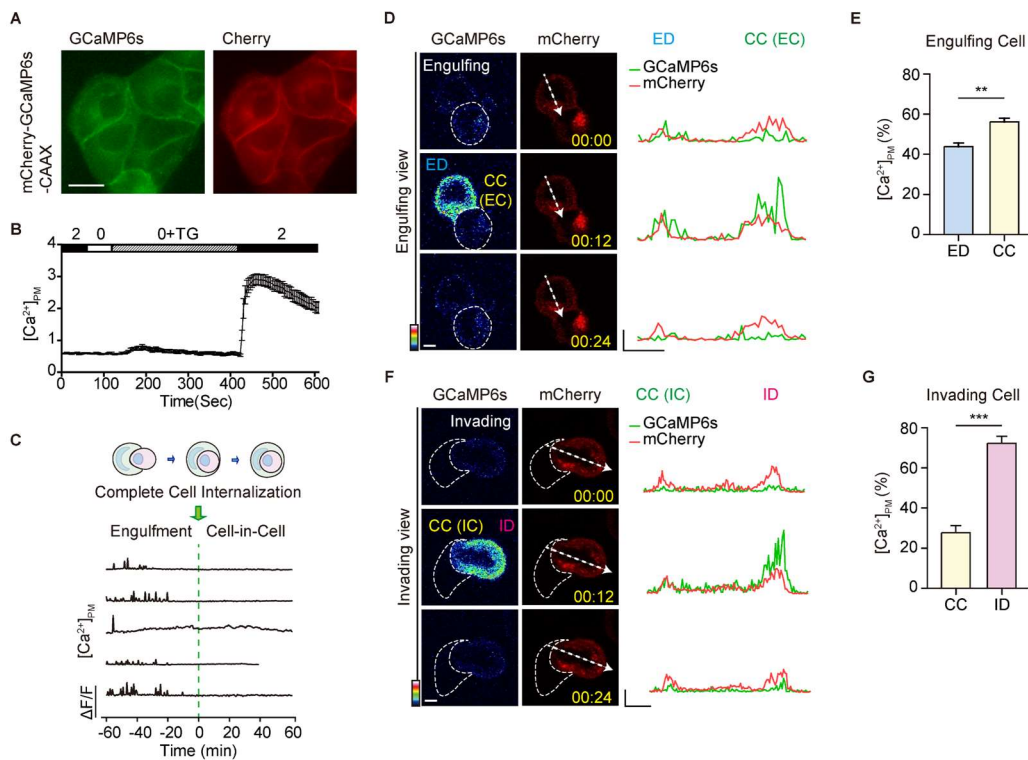


**Figure 7. Entotic cells show polarized membrane  $\text{Ca}^{2+}$  signals.**

(A) Fluorescence images of mCherry-GCaMP6s-CAAX. Scale bar = 20  $\mu\text{m}$ . (B) Thapsigargin (TG)-induced  $\text{Ca}^{2+}$  influx in MCF-7 cells monitored using GCaMP6s-CAAX/Cherry Fluorescence ratio. (C) Graph of normalized GCaMP6s-CAAX ratio in entotic cells. (D and F) Local  $\text{Ca}^{2+}$  influx was reported using GCaMP6s-CAAX, the PM  $\text{Ca}^{2+}$  indicator, in engulfing (D) and invading (F) cells. Line scan profile analysis of mCherry-GCaMP6s-CAAX signal. Scale bar = 5  $\mu\text{m}$ . X axis: 5  $\mu\text{m}$ , Y axis: 500. (E

and G) Bar graphs of the  $\text{Ca}^{2+}$  peak amplitudes in cell contact site and distal region of engulfing (n=5) (E) and invading (n=4) cells (G). Data represent mean  $\pm$  SEM. Significance was determined using unpaired two-tailed *t*-test. \*\*\**p* < 0.001; \*\**p* < 0.01. ED, Engulfing cell distal region; CC, cell-cell contact site; ID, Invading cell distal region.

### 1.3.6. $\text{IP}_3$ related store depletion could induce entotic $\text{Ca}^{2+}$ signaling.

To check how  $\text{Ca}^{2+}$  oscillations are induced and dependent on store depletion during entosis, I investigated whether intra-ER  $\text{Ca}^{2+}$  signaling through the inositol 1,4,5-trisphosphate receptor ( $\text{IP}_3\text{R}$ ) or sarco/endoplasmic reticulum  $\text{Ca}^{2+}$ -ATPase (SERCA) may affect the  $\text{Ca}^{2+}$  influx and entosis efficiency. First, I treated MCF7 cells with the  $\text{IP}_3\text{R}$  inhibitor, heparin (400  $\mu\text{g}/\text{ml}$ ) and Xestospongins C (4  $\mu\text{M}$ ), and measured intracellular  $\text{Ca}^{2+}$  concentration and entosis efficiency. The cells with the  $\text{IP}_3\text{R}$  inhibitor showed a reduced entosis efficiency (Figure 8A), as well as a decreased intracellular  $\text{Ca}^{2+}$  concentration (Figure 8B), indicating that  $\text{IP}_3\text{R}$  coupled store depletion followed by SOCE activation could play a role in entosis. Additionally, I depleted ER  $\text{Ca}^{2+}$  by treating the cells with DBHQ (Di-tert-butylhydroquinone) or TG (Thapsigargin), two SERCA inhibitors. These results showed that, DBHQ (25  $\mu\text{M}$ ) or TG (1  $\mu\text{M}$ ) significantly reduce the efficiency of entosis (Figure 8C), indicating that SERCA-mediated ER  $\text{Ca}^{2+}$  maintenance is crucial for entosis.

Therefore, these results suggest that intra-ER  $\text{Ca}^{2+}$  signaling through the  $\text{IP}_3\text{R}$  is critical for SOCE activation which leads to generating  $\text{Ca}^{2+}$  oscillations in entosis (Figure 8D).

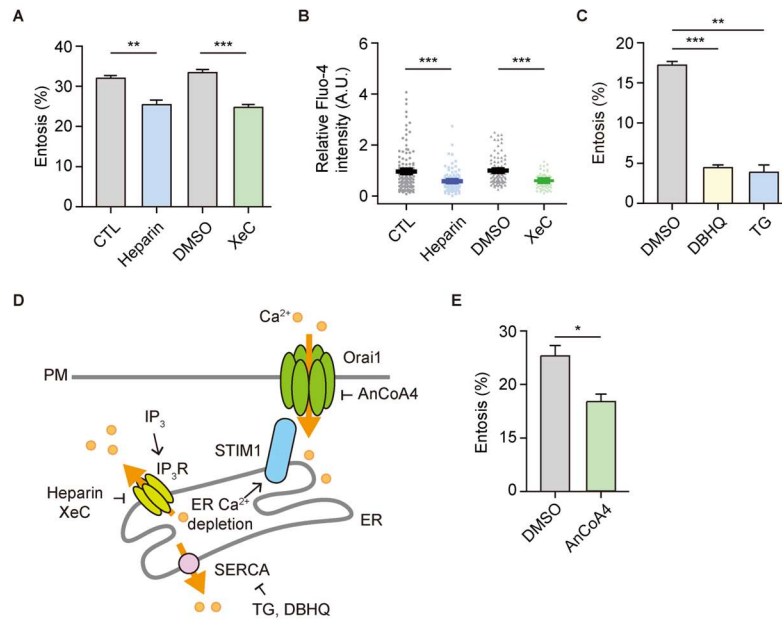


**Figure 8. IP<sub>3</sub> related store depletion could induce entotic Ca<sup>2+</sup> signaling.**

(A) Quantification of entotic cells cultured for 4 h with IP<sub>3</sub>R inhibitor, heparin (400 μg/ml) and Xestospongin C (4 μM). Data represent mean ± SEM of triplicate experiments (n > 300 in each experimental group). (B) Intracellular Ca<sup>2+</sup> levels of MCF7 cells in suspension with control (n = 124) and heparin (400 μg/ml, n = 102) and DMSO (n = 93) and Xestospongin C (4 μM, n = 59). Fluo-4 intensity quantification data represent mean ± SEM. (C) Quantification of entotic cells cultured for 2.5 h in SERCA inhibitors, DBHQ (25 μM) and TG (1 μM). Data represent mean ± SEM of duplicate experiments (n > 200 in each experimental group). (D) The schematic representation of SOCE activation and inhibitors. (E) The effect of AnCoA4 on entosis. The cells were pretreated with AnCoA4 (10 μM) and DMSO for 24 h and quantified entotic cells after 3 h suspension. Data represent mean ± SEM of triplicate experiments (n > 200 for each). Significance was determined using unpaired two-tailed *t*-test. \*\*\**p* < 0.001; \*\**p* < 0.01; \**p* < 0.05.

### 1.3.7. Genetic deletion of *Orai1* using CRISPR-Cas9 system.

I hypothesized that this polarized membrane  $\text{Ca}^{2+}$  might be induced by *Orai1*  $\text{Ca}^{2+}$  channels, the best-known SOC channel because it regulates lots of common signaling pathways in cancer cells, that are also essential for entosis, including actin polymerization, myosin contraction, and membrane blebbing. To test this, I treated MCF7 cells with 10  $\mu\text{M}$  AnCoA4 (Figure 8E), an *Orai1*-specific inhibitor that binds directly to the C-terminus region of *Orai1* and blocks  $\text{Ca}^{2+}$  influx (36). It is not surprising that I observed a decrease in entosis efficiency, indicating that the *Orai1* channel may be an entotic  $\text{Ca}^{2+}$  channel.

I used CRISPR-Cas9-generated *Orai1* knockout (KO) MCF7 cells to explore the function of *Orai1*  $\text{Ca}^{2+}$  channels during entosis (Figure 9A and B). I confirmed the ablation of *Orai1* protein expression in three representative *Orai1* KO cell lines with different indel (deletion/insertion) mutations using immunoblotting (Figure 9C) and immunocytochemistry (Figure 9D). There were no significant differences in other SOCE components (STIM1, STIM2, *Orai2*, *Orai3*) between wildtype (WT) and KO cells (Figure 9E-H).



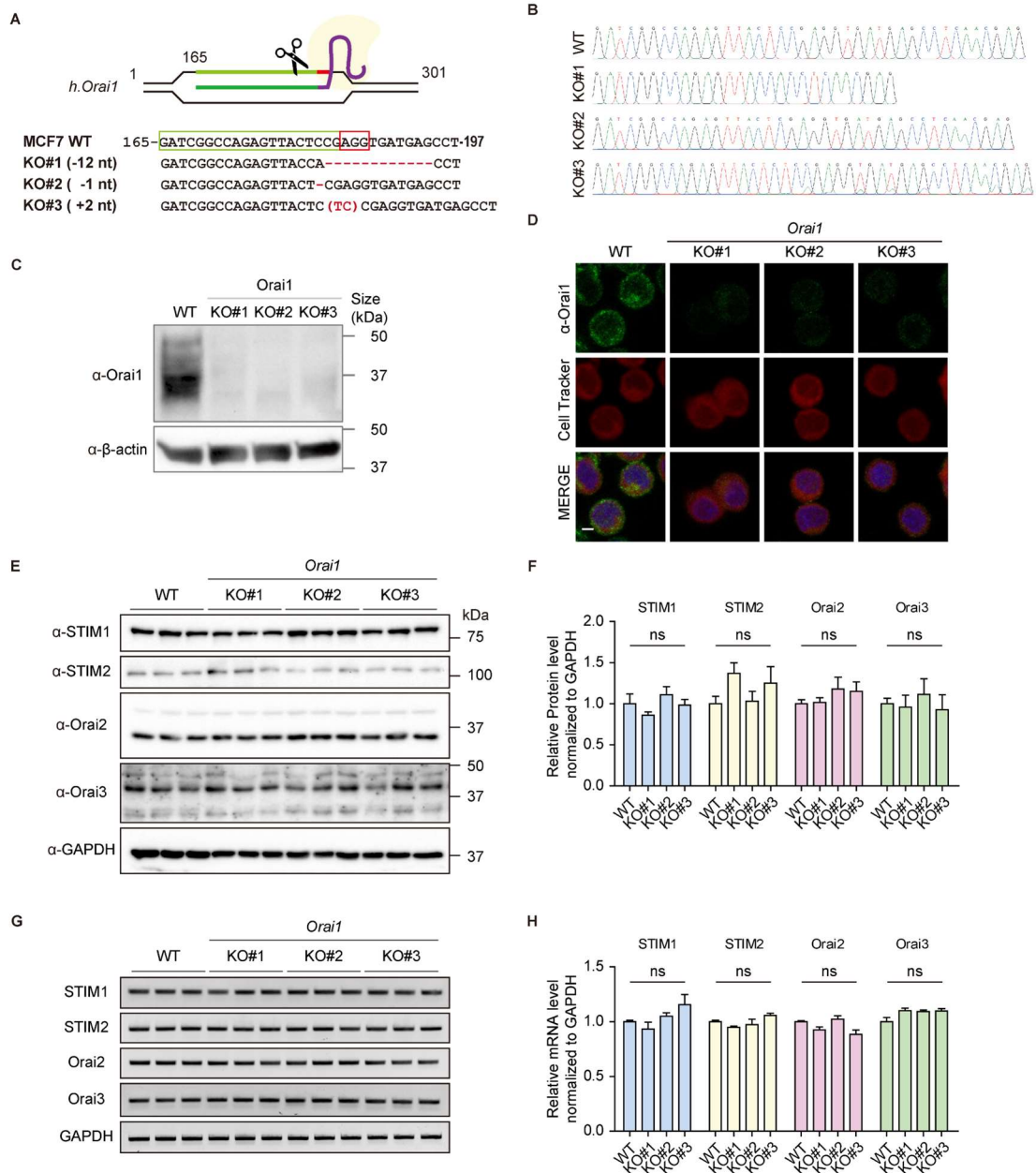


**Figure 9. Genetic deletion of Orai1 using CRISPR-Cas9 system.**

(A and B) Sequences of *Orai1* KO MCF7 cells. Alignment of human *Orai1* sequences from *Orai1* KO cell lines used in this study. (C) Western blot analysis of *Orai1* WT and KO MCF7 cells. β-actin was included as endogenous control. (D) Immunofluorescence images of endogenous Orai1 (green). Non-labeled Orai1 WT cells were mixed with Cell-Tracker Red labeled *Orai1* KO cell lines. (E and G) Protein (E) and mRNA (G) expression levels of other SOCE components: STIM1, STIM2, Orai2, and Orai3 in *Orai1* KO cell lines. GAPDH was used as endogenous control. (F and H) Relative protein (F, from E) and mRNA (H, from G) expression level of SOCE components normalized with GAPDH.

Statistical analysis was performed using one-way ANOVA followed by Dunnett's test. ns, not significant.

### 1.3.8. *Orai1* is the entotic $\text{Ca}^{2+}$ channel.

I confirmed that the loss of *Orai1* resulted in significantly reduced SOCE when ER  $\text{Ca}^{2+}$  stores were depleted (Figure 10A and B). I next found that *Orai1* deletion decreased entosis efficiency from 40% to 15% (Figure 10C), indicating that *Orai1*  $\text{Ca}^{2+}$  channels positively regulate entosis. To investigate whether *Orai1*  $\text{Ca}^{2+}$  channels induce local  $\text{Ca}^{2+}$  influx in entotic cells during the engulfment stages of entosis, I expressed mCherry-GCaMP6s-CAAX in *Orai1* WT and KO cells, acquired time-lapse images at 30 s intervals over 4h, and aligned the end of engulfment to time 0. WT cells showed PM-localized  $\text{Ca}^{2+}$  oscillations before entotic cells formed CIC structures (engulfment stage: -60~0 min) (Figure 10D-F). Surprisingly, few oscillating cells were detected and the frequency of  $\text{Ca}^{2+}$  oscillations was significantly lower in *Orai1* KO cells (Figure 10D-F). Finally, I expressed *Orai1*-GCaMP6s in MCF7 cell and measured *Orai1*-mediated local  $\text{Ca}^{2+}$  influx, confirming no difference in cellular  $\text{Ca}^{2+}$  level in *Orai1*-GCaMP6s expressing cells (Figure 10G and H). *Orai1*-GCaMP6s expressing cells showed *Orai1*-mediated  $\text{Ca}^{2+}$  oscillations during engulfment (Figure 10I). These results suggest that *Orai1* is a bona fide entotic  $\text{Ca}^{2+}$  channel that provides local  $\text{Ca}^{2+}$  oscillations in entotic cells for the engulfment.



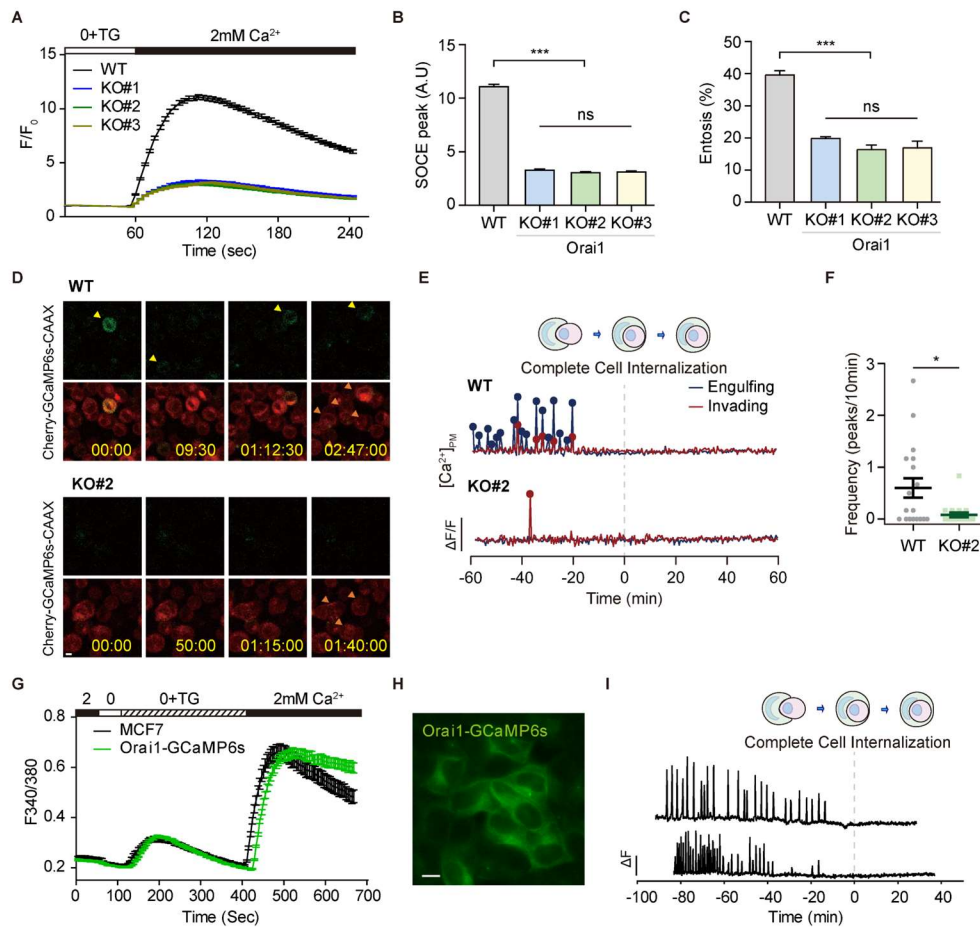


**Figure 10. Orai1 is the entotic  $\text{Ca}^{2+}$  channel.**

(A) TG-induced  $\text{Ca}^{2+}$  influx in *Orai1* KO cell lines monitored by Fluo-4 ( $F/F_0$ ). (B) Comparison between the SOCE peaks from (A). Data represent mean  $\pm$  SEM ( $n=165, 67, 136,$  and  $148$  cells from each cell line). Statistical analysis was performed using one-way ANOVA followed by Dunnett's test.  $***p < 0.001$ . ns, not significant. (C) Quantification of entotic cells in *Orai1* WT and KO MCF7 cells. Data represent mean  $\pm$  SEM of the triplicate experiments ( $n > 300$  in each experimental group). Statistical analysis was performed using one-way ANOVA followed by Dunnett's test.  $***p < 0.001$ . ns, not significant. (D) Plasma membrane  $\text{Ca}^{2+}$  oscillations in Cherry-GCaMP6s-CAAX expressing *Orai1* WT MCF7 cells. Scale bar =  $20 \mu\text{m}$ . (E) Local  $\text{Ca}^{2+}$  influx reported using mCherry-GCaMP6s-CAAX in *Orai1* WT and KO MCF7 cells. (F) Quantification of  $\text{Ca}^{2+}$  signals in *Orai1* WT and KO entotic cells ( $n=18$  for each). Three independent experiments were quantified. Significance was determined using unpaired two-tailed *t*-test.  $*p < 0.05$ . (G) TG-induced  $\text{Ca}^{2+}$  influx in Orai1-GCaMP6s expressing MCF7 cell line monitored by Fura-2 (F340/F380). (H) Orai1 mediated  $\text{Ca}^{2+}$  influx in Orai1-GCaMP6s expressing MCF7 cells. Scale bar =  $10 \mu\text{m}$ . (I) Orai1 mediated  $\text{Ca}^{2+}$  oscillations reported using Orai1-GCaMP6s in MCF7 cells. Mean fluorescence intensity. Y axis:  $2000$  (A.U.).

### 1.3.9. Orai1 has the differential distribution following entosis stage.

To determine whether Orai1  $Ca^{2+}$  channels affect  $Ca^{2+}$  concentrations in entotic cells, I analyzed the localization of endogenous Orai1 at early, middle, and late engulfment stages, based on the proportion of engulfment membrane (Figure 11A). Similar to the observation that entotic cells have differential  $Ca^{2+}$  concentrations with mCherry-GCaMP6s-CAAX (Figure 7D-G), I observed preferential localization of Orai1 during engulfment. Approximately 60% of Orai1 accumulated at CC in the early and middle engulfment stages and moved to the ID in the late stage (Figure 11B). I tracked the localization of Orai1 in cells expressing GFP-Orai1 using time-lapse imaging (Figure 11C). Although distinct differential localization of endogenous Orai1 or GFP-Orai1 was not observed in engulfing cells, GFP-Orai1 was enriched in CC during the early engulfment stage and translocated predominantly to the ID following engulfment. Moreover, the polarized localization of Orai1 was confirmed using cells labeled with cytoplasmic membrane dyes (CellBrite Red, lipophilic carbocyanine, Figure 11D) and cytosol dyes (CellTracker Red, Figure 11E).

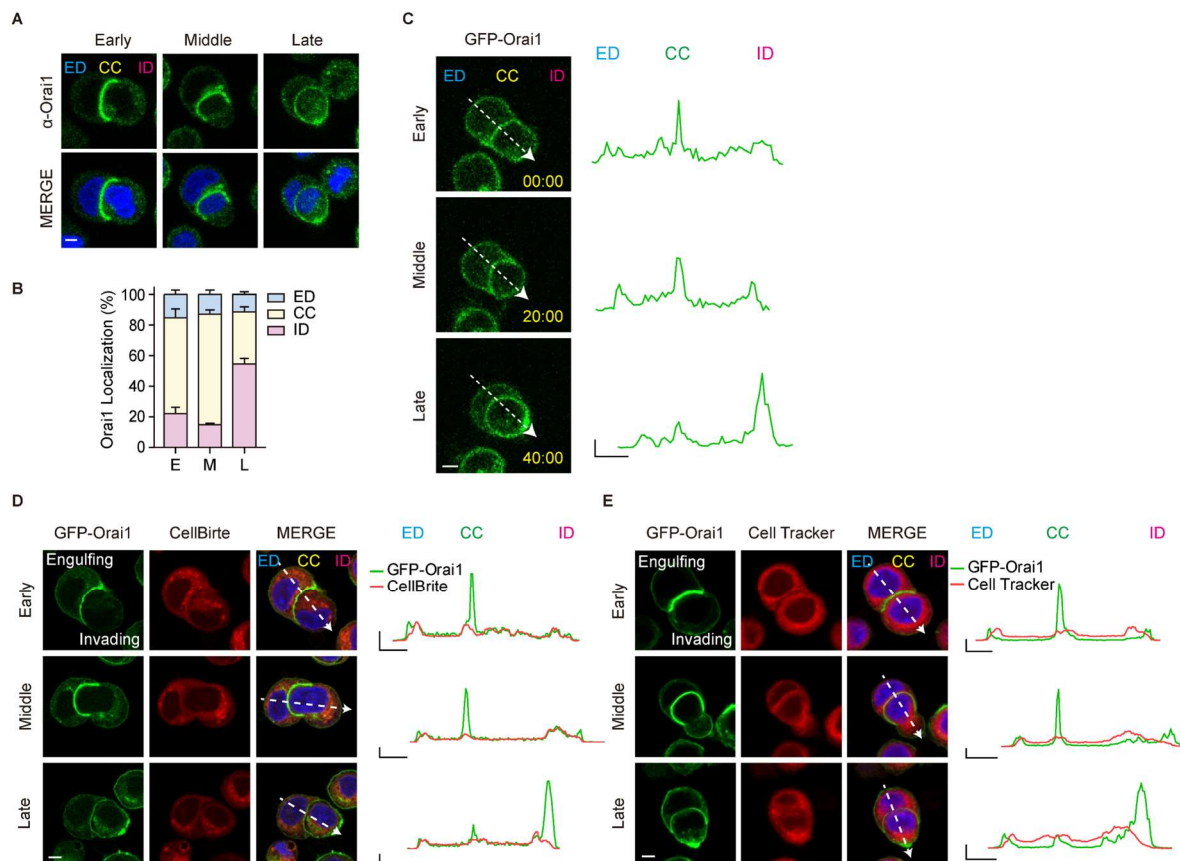


**Figure 11. Orai1 has the differential distribution following entosis stage.**

(A) Immuno-fluorescent images of suspended cells taken after 2.5 h of culturing show endogenous Orai1 (green). (B) Bar graphs showing the distribution of Orai1 at different engulfment stages. Early-

stage (E, <1/3 internalization, n=10); middle-stage (M, 1/3 -2/3 internalization, n=24); late-stage (L, >2/3 internalization, n=35). (C) Time-lapse fluorescence images of GFP-Orai1 stably expressed MCF7 cells during entosis. Times are indicated as hours: minutes: seconds. Line graphs show GFP pixel intensities for the indicated line scans. X axis: 5  $\mu\text{m}$ , Y axis: 5000 (A.U.). (D and E) Fluorescence images of GFP-Orai1 expressing MCF7 cells stained with CellBrite PM marker (D, red, PM) or CellTracker (E, red, cytosol). Line scan analysis of relative GFP-Orai1 (green) and PM or cytosol marker (red) signals along the white arrow in the merge image. X axis: 5  $\mu\text{m}$ , Y axis: 1 (A.U.). Scale bar = 5  $\mu\text{m}$ . ED, Engulfing cell distal region; CC, cell-cell contact site; ID, Invading cell distal region.

### 1.3.10. Orai1 shows the polarized distribution in invading cells.

With single fluorescence imaging, it is difficult to determine the differential localization of Orai1 in entotic cell pairs, although I observed the preferential localization of Orai1 in ID. Therefore, I expressed GFP-Orai1 respectively in engulfing cell or invading cell and additionally co-expressed Lyn-Cherry, PM marker protein, demonstrating the preferential localization of Orai1 during entosis (Figure 12A). Furthermore, I mixed cells expressing mCherry-Orai1 or GFP-Orai1 and visualized the localization of Orai1 in entotic cells, having different pairs of fluorescent-tagged-Ora1s during engulfment (Figure 12B). Two-color label assay confirmed that Orai1 was translocated from CC (IC) to ID in invading cells (Figure 12C and D), but engulfing cells appeared preferentially at the CC during entire engulfment stage (Figure 12C and D). The polarized patterns were further confirmed using endogenous Orai1 immunofluorescence imaging (Figure 12E and F).

Orai1 channels are activated through direct interaction with the ER  $\text{Ca}^{2+}$  sensor, STIM. Co-expressing GFP-Orai1 and Cherry-STIM1 in MCF7 cells showed that Orai1 and STIM1 are co-localized during entosis (Figure 12G and H) suggesting that STIM1 activates Orai1, resulting in entotic  $\text{Ca}^{2+}$  oscillation and cellular responses during engulfment.

Taken together, Orai1 translocation and the spatial entotic  $\text{Ca}^{2+}$  oscillation is well correlated, suggesting that Orai1, as an entotic  $\text{Ca}^{2+}$  channel, may regulate spatiotemporal  $\text{Ca}^{2+}$  signaling in entotic cell pairs during entosis.

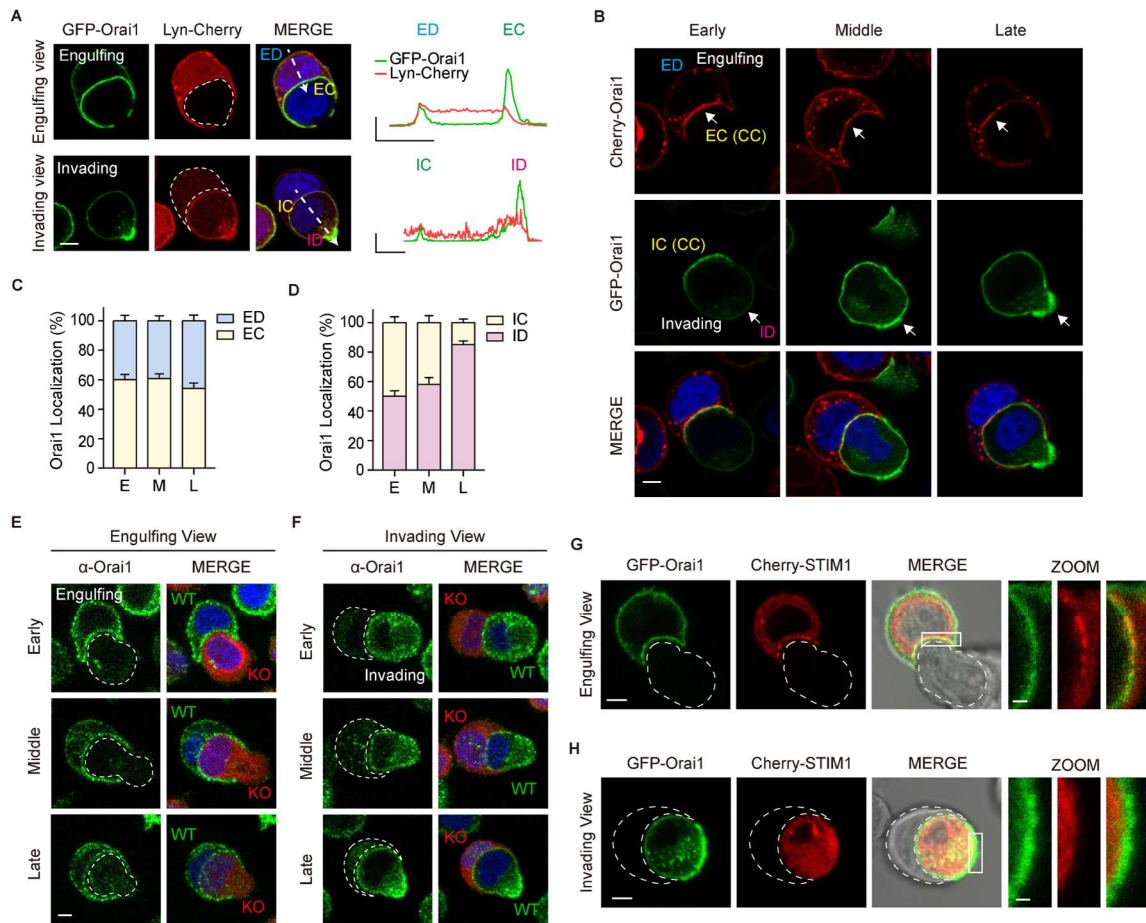


**Figure 12. Orai1 shows the polarized distribution in invading cells.**

(A) Fluorescence images of GFP-Orai1 and Lyn-Cherry (PM marker) expressing MCF7 cells. Line scan analysis of relative GFP-Orai1 (green) and Lyn-Cherry (red) signals along the white arrow in the merge image. X axis: 5  $\mu$ m, Y axis: 1 (A.U.). (B) Fluorescence images of Cherry-Orai1 (engulfing cell)- and GFP-Orai1 (invading cell)- expressing MCF7 cells cultured for 2.5 h in suspension. (C and D) Bar graphs showing Orai1 distribution in engulfing cells (C) and invading cells (D). (E and F) Immunofluorescence images of endogenous Orai1 (green) in WT and *Orai1* KO (red) cells show Orai1 distribution in engulfing (E) and invading cells (F). (G and H) Fluorescence images of GFP-Orai1- and Cherry-STIM1- expressing MCF7 cells cultured for 2.5 h in suspension. Engulfing (G) and Invading (H) cells. Cropped image scale bar = 1  $\mu$ m. Scale bar = 5  $\mu$ m. ED, Engulfing cell distal region; CC, cell-cell contact site; ID, Invading cell distal region; EC, Engulfing cell contact site; IC, Invading cell contact region.

### 1.3.11. SEPTIN inhibitor suppresses entosis.

SEPTINs have been known to modulate local STIM-ORAI  $\text{Ca}^{2+}$  signaling by modulating Orai1 concentrations at the ER-PM junction (29, 37, 38), which led us to investigate whether SEPTINs regulate Orai1 distribution in entotic cells during entosis.

First, I explored the role of SEPTINs during entosis using the SEPTIN inhibitor, forchlorfenuron (FCF; 50  $\mu\text{M}$ ) which alters the assembly and disassembly of SEPTIN networks (39). Surprisingly, I found that entosis efficiency in MCF7 cells treated with FCF for 4 h reduced from approximately 35% to 15% (Figure 13A). And I confirmed the unrecognized function of SEPTINs by adding the inhibitor in the middle of entosis. Efficiency decreased to 25% compared with the control (40%) 2 h after FCF was added (Figure 13B). I also found that FCF also delayed the early-stage onset of entosis (Figure 13C). Hence, these results suggest that SEPTINs may play a role in entosis by modulating the preferential localization of Orai1 and local  $\text{Ca}^{2+}$  oscillations.

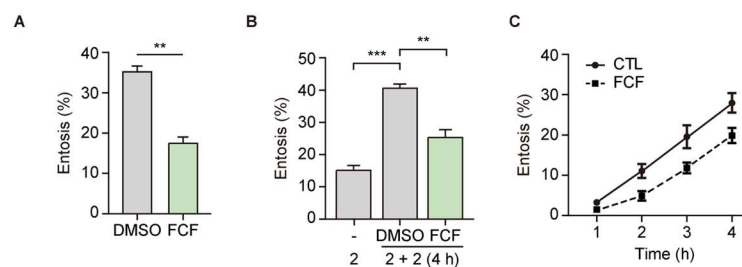


**Figure 13. SEPTIN inhibitor suppresses entosis.**

(A) Quantification of entotic cells cultured for 4 h with DMSO and the SEPTIN inhibitor, FCF (50  $\mu\text{M}$ ). Data represent mean  $\pm$  SEM of triplicate experiments ( $n > 300$  in each experimental group). (B) Quantification of internalized cells suspended in FCF. Cells were pre-suspended for 2 h and then mixed with FCF and cultured for an additional 2 h. Data represent mean  $\pm$  SEM of triplicate experiments ( $n > 200$  in each experiment). (C) Time-dependent quantification of entotic cells with or without FCF. MCF7 cells were cultured in suspension for 4 h at 1 h intervals. Data represent mean  $\pm$  SEM of triplicate experiments ( $n > 300$  in each experiment). Significance was determined using unpaired two-tailed  $t$ -test. \*\*\* $p < 0.001$ , \*\* $p < 0.01$

### 1.3.12. SEPT2 co-localizes with Orai1.

Next, I checked whether SEPT2, a core component of SEPTIN filaments (26, 40, 41), might translocate in entotic cells during engulfment. Surprisingly, I found that SEPT2 is also mainly accumulated at CC during the early and middle and translocated to ID at the late stage of engulfment (Figure 14A and B).



The subcellular location and translocation patterns of SEPT2 are similar to those of Orai1 and local  $Ca^{2+}$  signaling at different engulfment stages (Figure 14A and B; Figure 14C and D). Moreover, the polarized localization of SEPT2 was confirmed using cells labeled with cytoplasmic membrane dyes (CellBrite Red, Figure 14E) and cytosol dyes (CellTracker Red, Figure 14F).

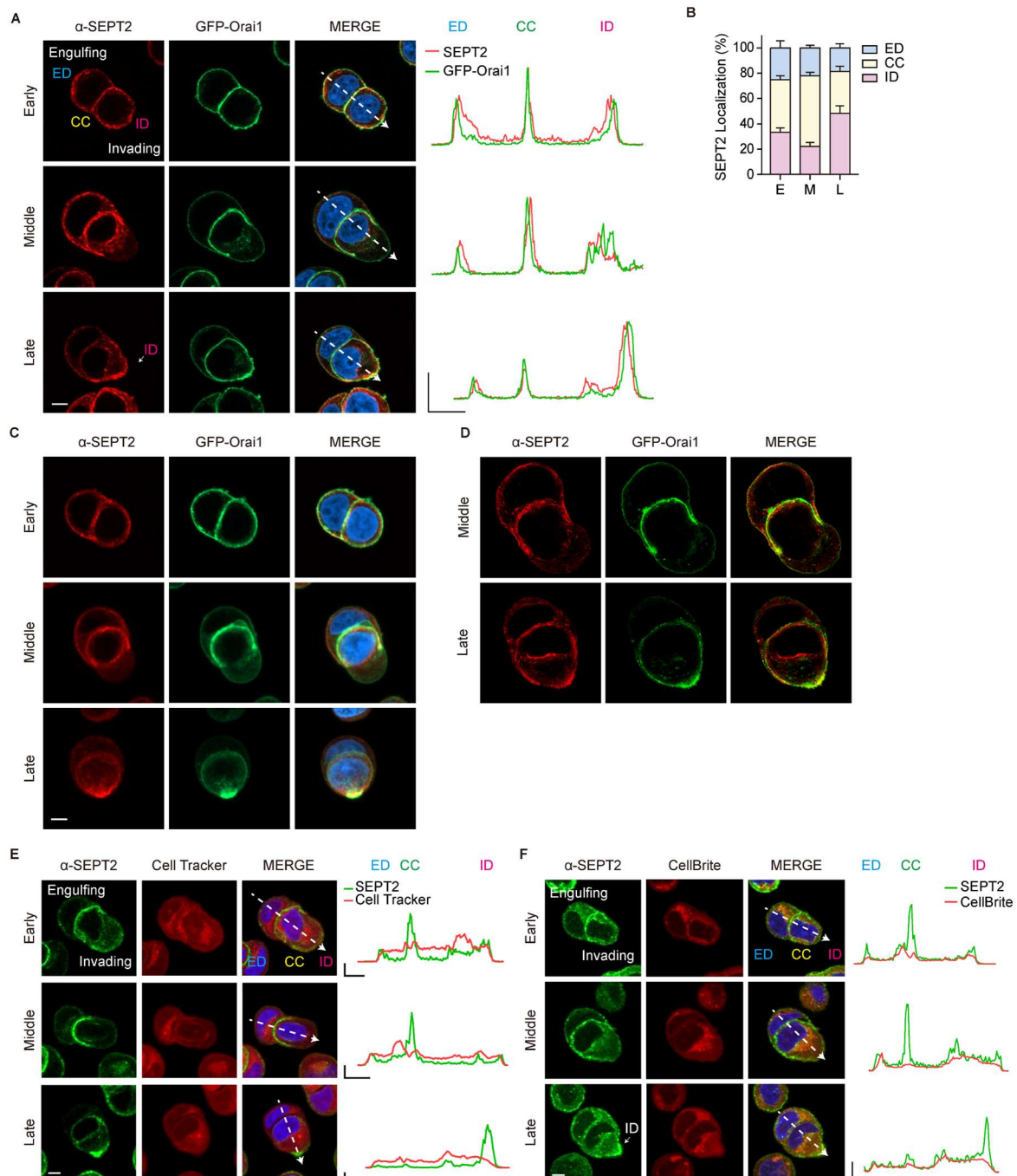


**Figure 14. SEPT2 co-localizes with Orai1.**

(A) Immunofluorescence images show endogenous SEPT2 (red) and GFP-Orai1 (green) in MCF7 cells cultured for 2.5 h in suspension. The arrow indicates enriched SEPT2 at ID. Line graphs show relative

SEPT2 (red) and GFP-Orai1 (green) intensities for the indicated line scans. X axis: 5  $\mu\text{m}$ , Y axis: 1 (A.U.). (B) Bar graph showing the distribution of SEPT2 at different engulfment stages. Early-stage (E, n = 7); middle-stage (M, n = 9); and late-stage (L, n = 13). (C) 3D projection of immunofluorescence images showing endogenous SEPT2 (red) and GFP-Orai1 (green) (D) Super-resolution microscopy of the localization of SEPT2 (red) and GFP-Orai1 (green) during entosis. (E and F) Immuno-fluorescent images of suspended cells taken after 2.5 h of culturing show endogenous SEPT2 (green) and CellTracker (E, red, cytosol marker) or and CellBrite (F, red, PM marker). Line graphs show SEPT2 (green) and cytosol or PM marker (red) intensities for the indicated line scans. X axis: 5  $\mu\text{m}$ , Y axis: 1 (A.U.). Scale bar = 5  $\mu\text{m}$ . ED, Engulfing cell distal region; CC, cell-cell contact site; ID, Invading cell distal region.

### 1.3.13. SEPT2 organizes the distribution of Orai1 in invading cells.

I further confirmed that differential distributions of GFP-SEPT2 filament structures beneath PM were in MCF7 cells treated with FCF, showing an abnormal GFP-SEPT2 pattern at CC and ID (Figure 15A and B). Thus, altered SEPTIN dynamics reduced entosis under FCF conditions with abnormal SEPT2 distribution, showing reduced SEPT2 translocation from CC to ID (Figure 15C-H, I and J). Thus, SEPT2 might regulate the preferential localization of Orai1 in entotic cells during engulfment, resulting in spatially controlled  $\text{Ca}^{2+}$  oscillation. Hence, I investigated whether FCF-treated SEPTIN altered the local distribution of Orai1 during entosis. Orai1 and SEPT2 were co-localized in MCF7 cells regardless of FCF treatment, indicating that SEPT2 is a strong Orai1 modulating protein and determines the location of Orai1 in entotic cells. Further, FCF reduced the accumulation of Orai1 at ID in the late stage (Figure 15C-H, I and K).

To determine whether SEPTINs bind to Orai1 and affect the Orai1-STIM1 complex, I expressed Flag-Myc-Orai1 and GFP-SEPT2 or GFP-STIM1, and immunoprecipitated them with Flag-Myc-Orai1. FCF reduced the interaction between Orai1 and SEPT2 (Figure 15L). GFP-STIM1 intensity increases through TG treatment (from 0.38 to 1.05) and decreases through FCF treatment (from 1.05 to 0.63), suggesting that STIM1 and Orai1 interaction is store-dependent and regulated by SEPTINs (Figure 15M). These data indicated that SEPT2 regulates entotic  $\text{Ca}^{2+}$  signaling via Orai1-SEPT2 and SOCE complex for the local distribution of Orai1.

These results provide the first evidence that SEPTINs are involved in entosis, stabilizing STIM1-Orai1 complexes, critical for entotic  $\text{Ca}^{2+}$  signaling around cell-cell contact and distal membranes of invading cells.

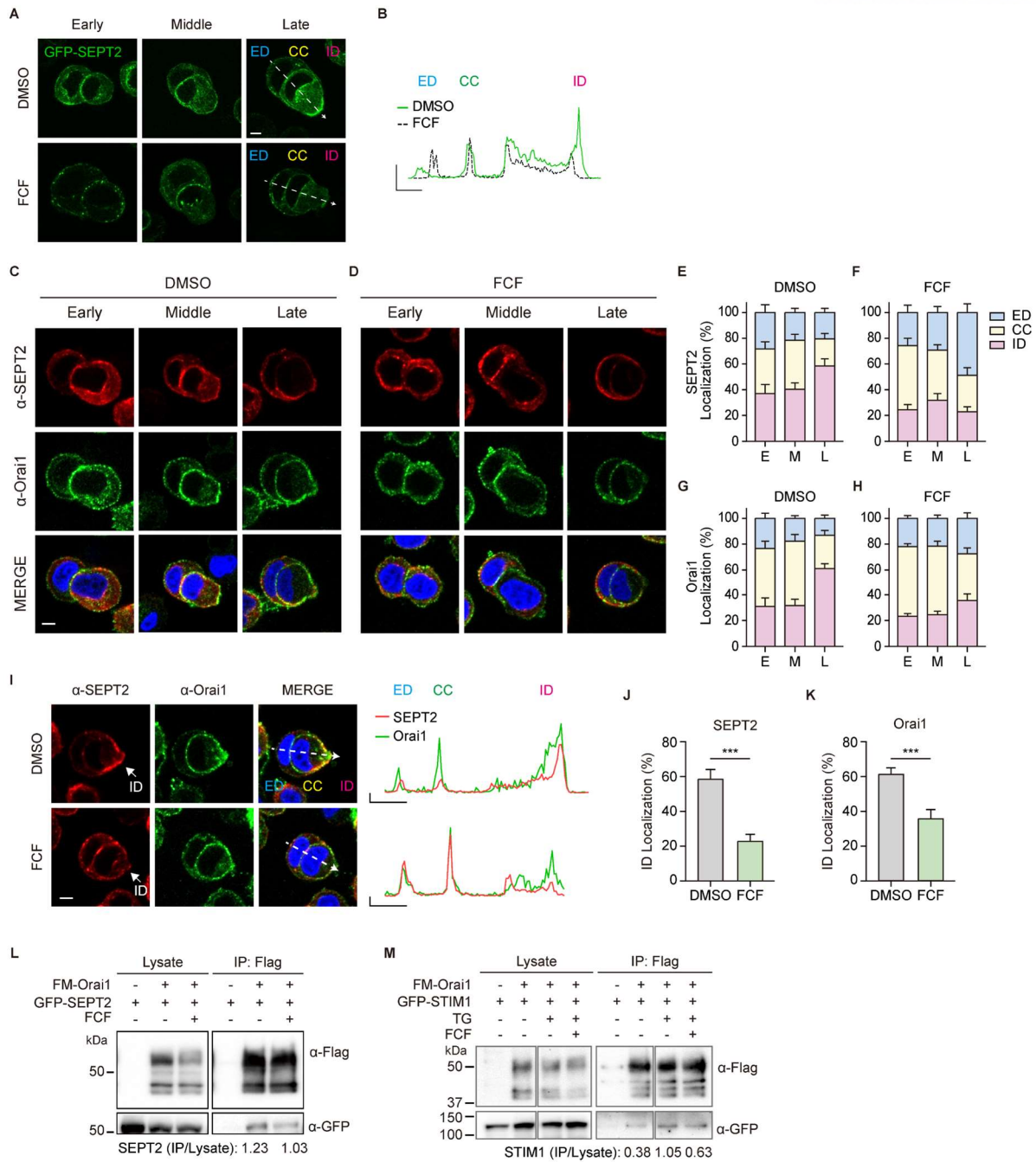


**Figure 15. SEPT2 organizes the distribution of Orai1 in invading cells.**

(A) Fluorescence images of GFP-SEPT2-expressing MCF7 cells cultured for 2.5 h in DMSO and FCF (50  $\mu$ M). (B) Line graphs show the distribution of GFP-SEPT2 in DMSO (green) and FCF (black dotted). (C and D) Immunofluorescence images showing endogenous SEPT2 (red) and endogenous Orai1 (green) in MCF7 cells cultured for 2.5 h in DMSO (C) or FCF (D, 50  $\mu$ M). Scale bar = 5  $\mu$ m. (E to H) Bar graphs showing the distribution of SEPT2 (E, DMSO; F, FCF) and Orai1 (G, DMSO; H, FCF). n = 34 in the DMSO group; n = 29 in the FCF group. (I) Immunofluorescence images showing endogenous SEPT2 (red) and endogenous Orai1 (green) in MCF7 cells cultured for 2.5 h in DMSO or



FCF (50  $\mu\text{M}$ ). The arrow indicates enriched SEPT2 at ID. Line graphs show the distribution of SEPT2 (red) and Orai1 (green). X axis: 5  $\mu\text{m}$ , Y axis: 5000 (A.U.). (J and K) Bar graphs showing the distribution of SEPT2 (J, n = 10) and Orai1 (K, n = 7) at ID in late engulfment stage (from E to H). (L) Immunoblots of whole-cell lysates (left) or IP (right) from cell co-expressing Flag-Myc-Orai1 and GFP-SEPT2 in HEK293T cells with or without 50  $\mu\text{M}$  of FCF. (M) Immunoblots of whole-cell lysates (left) or IP (right) from cell co-expressing Flag-Myc-Orai1 and GFP-STIM1 in HEK293T cells with or without 50  $\mu\text{M}$  of FCF and TG (1  $\mu\text{M}$ ). Scale bar = 5  $\mu\text{m}$ . Significance was determined using unpaired two-tailed *t*-test. \*\*\**p* < 0.001. ED, Engulfing cell distal region; CC, cell-cell contact site; ID, Invading cell distal region. E, Early; M, Middle; L, Late.

#### **1.3.14. MLC phosphorylation is induced by Orai1 at invading cell distal region and peripheral junction.**

Finally, I explored the molecular mechanism by which the entotic Orai1  $\text{Ca}^{2+}$  signaling affects the entotic machinery or target signaling molecules involved in the engulfment processes. I showed that entotic  $\text{Ca}^{2+}$  signaling is necessary for the morphological changes in cells which are regulated by actin-myosin mediated cytoskeleton rearrangement during engulfment (Figure 5E-G). Myosin activity of actomyosin is regulated by reversible phosphorylation of conserved amino acids, specifically at serine-19 in myosin light chain (MLC), and determined by the balance between activities of several kinases like MLCK, ROCK, and myosin phosphatase. I hypothesized that local Orai1  $\text{Ca}^{2+}$  influx might activate  $\text{Ca}^{2+}$ /CaM/MLCK signaling pathway, resulting in MLC phosphorylation (pMLC) for actomyosin contractility and changes in entotic cell morphology.

First, I evaluated the influence of MLCK on entosis using two MLCK inhibitors, ML-9 (10  $\mu\text{M}$ ) and peptide-18 (P18, 10  $\mu\text{M}$ ). ML-9 is a classic MLCK inhibitor and P18 is a specific MLCK inhibitor that mimics the inhibitory domain of MLCK by interacting with the catalytic domain of MLCK. MCF7 cells with inhibitors showed reduced entosis efficiency, demonstrating that MLCK activity and phosphorylation of its downstream protein (MLC) might affect entosis (Figure 16A).

I also examined the local distribution of pMLC as an indicator of active actomyosin bundles as well as Orai1 entotic  $\text{Ca}^{2+}$  mediators during engulfment. Actomyosin, which is asymmetrically enriched and highly active at the ID, drives cell internalizations by providing contractile force. In addition, actomyosin at the peripheral junction (PJ) of engulfing and invading cells maintains the stability of the AJ (Adherent Junction) complex, which occasionally forms a ring-like structure with F-actin. Besides, pMLC was colocalized with Orai1 during engulfment and was enriched in ID (Figure 16B and D) and PJ (Figure 16C and E). Moreover, I confirmed the local MLC phosphorylation using cells labeled with cytosol dyes (CellTracker Red, Figure 16F) and cytoplasmic membrane dyes (CellBrite Red, Figure

16G). These results implicated the role of Orai1 as an entotic  $\text{Ca}^{2+}$  mediator for activating actomyosin through local MLC phosphorylation.

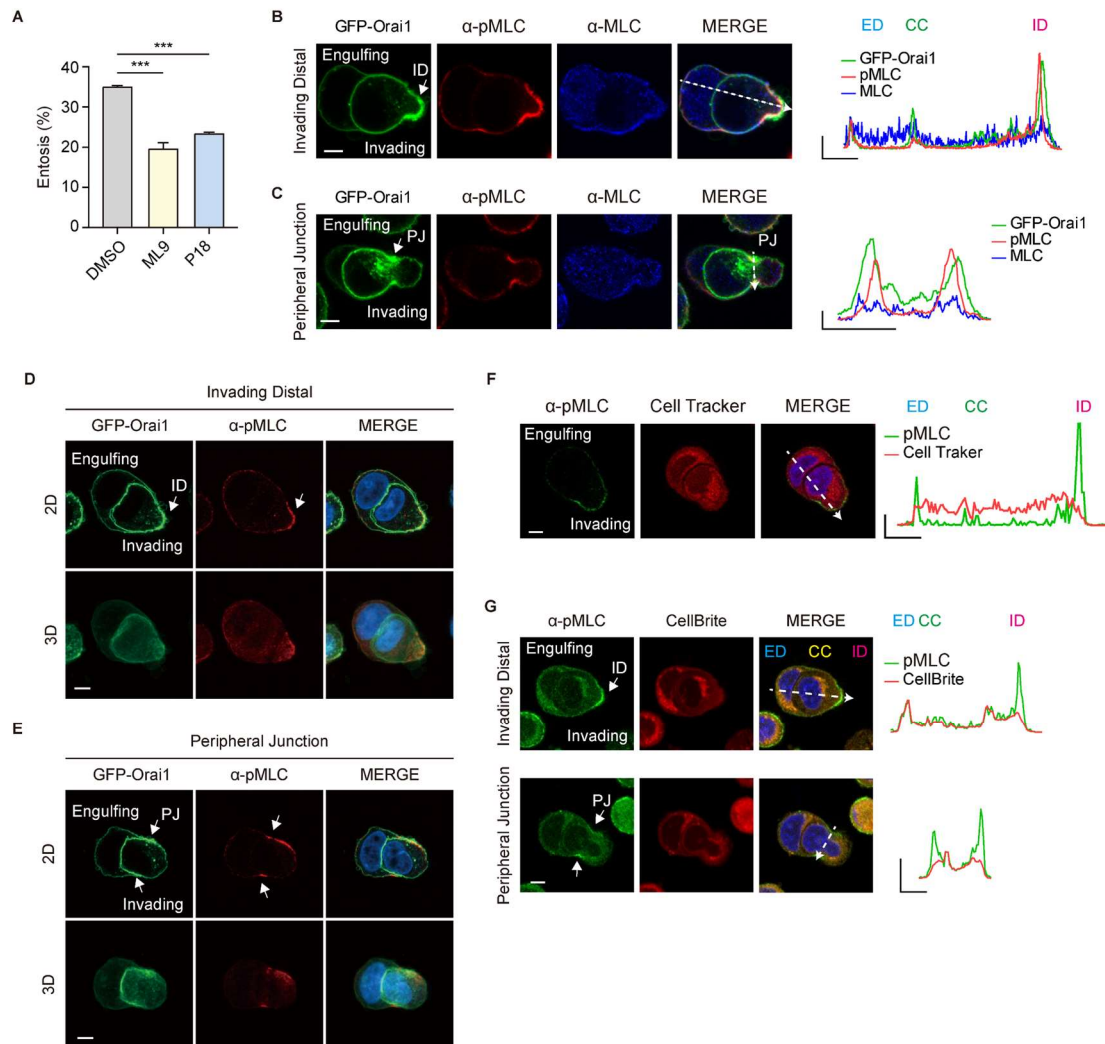


**Figure 16. MLC phosphorylation is induced by Orai1 at invading cell distal region and peripheral junction.**

(A) Quantification of entotic cells cultured for 4 h in DMSO and MLCK inhibitors, ML-9 (10  $\mu\text{M}$ ) and P18 (10  $\mu\text{M}$ ). Data represent mean  $\pm$  SEM of triplicate experiments ( $n > 300$  in each experimental group). Significance was determined using unpaired two-tailed  $t$ -test. \*\*\* $p < 0.001$ . (B and C) Immunofluorescence images of suspended cells after 2.5 h of culturing show endogenous pMLC (red) and MLC (blue) in GFP-Orai1-expressing MCF7 cells. pMLC2 is enriched at ID (B) and PJ (C) compared with total MLC. Line graphs show pMLC, MLC, and GFP intensities for the indicated line scans. X axis: 5  $\mu\text{m}$ , Y axis: 5000. (D and E) Immunofluorescence images showing endogenous pMLC (red) in GFP-Orai1 expressing MCF7 cells cultured in suspension for 2.5 h. pMLC is enriched at ID (D) and PJ (E). (F and G) Immunofluorescent images of suspended cells taken after 2.5 h of culturing show

endogenous pMLC (green) and CellTracker (F, red, cytosol marker) or CellBrite (G, red, PM marker). Line graphs show relative pMLC (green) and cytosol or PM marker (red) intensities for the indicated line scans. X axis: 5  $\mu\text{m}$ , Y axis: 5 (F) or 1 (G) (A.U.).

### **1.3.15. Local entotic $\text{Ca}^{2+}$ signaling of Orai1 induces the local phosphorylation of MLC.**

I also examined whether  $\text{Ca}^{2+}$ /CaM/MLCK might affect pMLC in Orai1-enriched locations within entotic cell pairs using MLCK and SOC channel (Orai1) inhibitors. MLCK inhibitor (P18) or SOC channel blockers (SKF96365) decreased pMLC intensity in ID (Figure 17A-C, G and H) and PJ (Figure 17D-F, G and I), indicating that suppressing Orai1/ $\text{Ca}^{2+}$  and MLCK reduces MLCK activity and pMLC in entotic  $\text{Ca}^{2+}$ -active regions.

To confirm whether SOCE induced entosis through MLCK, I conducted a double inhibition experiment with SOC channel (SKF96365) and MLCK (P18) inhibitors. I compared the efficiency of entosis between cells treated with both inhibitors and against each other. The effects of MLCK and SOC channel inhibitor on the reduction of entosis were not significantly different. In addition, reduced entosis efficiency was not further decreased when both inhibitors were used (Figure 17J). Additionally, I checked the effect of MLCK inhibitors on entosis using Orai1 KO cells. The entosis efficiency was not further decreased when two MLCK inhibitors were used in Orai1 KO cells (Figure 17K). Furthermore, I examined the MLC phosphorylation in the double inhibition (Figure 17L and M). MLCK inhibition alone was not significantly different from MLCK and SOC channel double inhibition. Therefore, these results suggest that SOC channel induce entosis through the activation of MLCK.

These findings suggest that Orai1 channel activates CaM/MLCK and myosin (pMLC) in specific cell regions, facilitating engulfment between entotic cells (Figure 18).

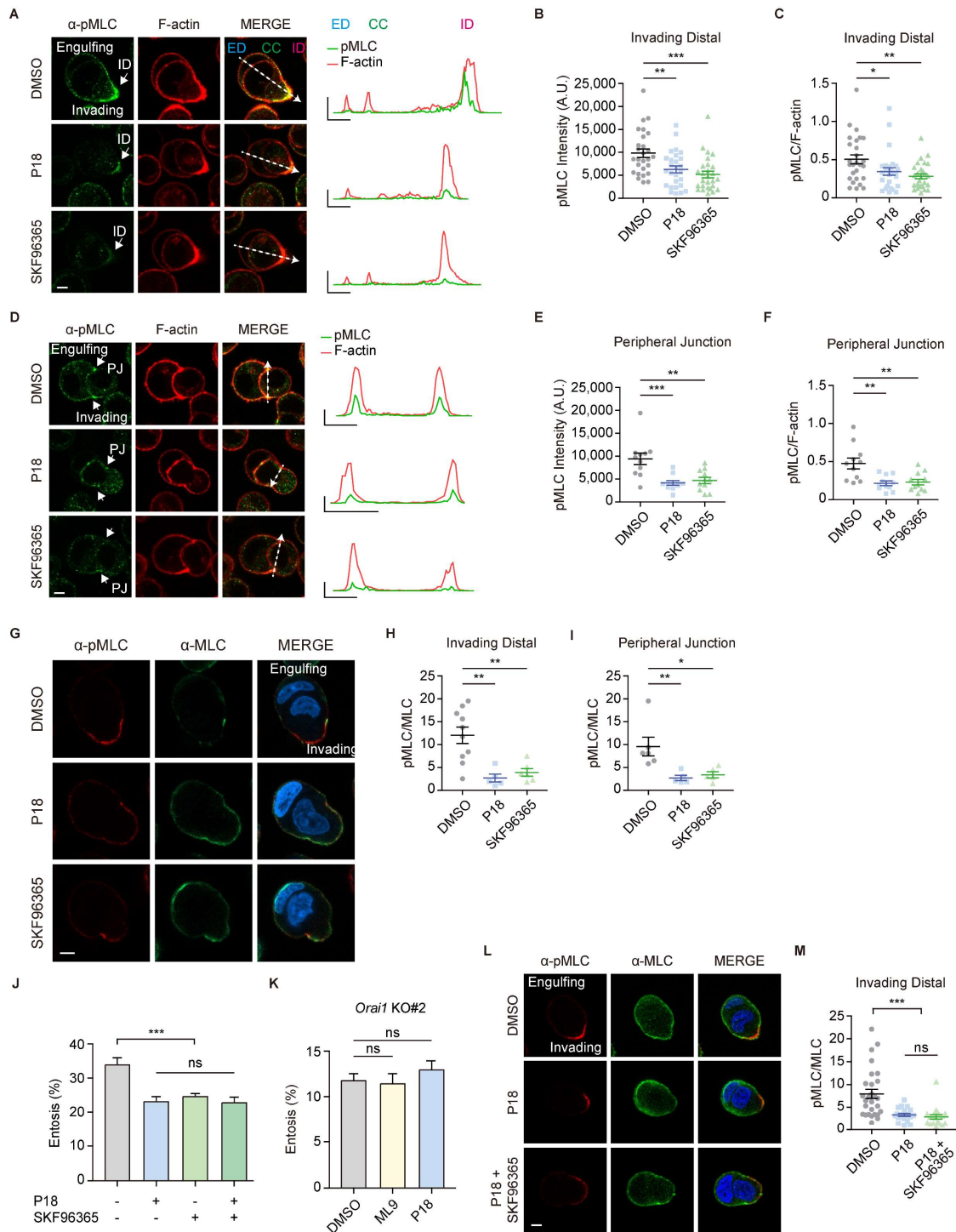


**Figure 17. Local entotic  $\text{Ca}^{2+}$  signaling of Orai1 induces the local phosphorylation of MLC.**

(A and D) Immunofluorescence images of endogenous pMLC (green) and F-actin (phalloidin, red) cultured with DMSO, P18, or SKF96365 at ID (A) and PJ (D). Line graphs show pMLC and F-actin intensities for the indicated line scans. X axis: 5  $\mu$ m, Y axis: 20000. (B and E) Quantification of pMLC2 intensity at ID (B, n = 27 in each group) and PJ (E, n = 11 in each group). Significance was determined

using unpaired two-tailed *t*-test. \*\*\**p* < 0.001; \*\**p* < 0.01. (C and F) Quantification of pMLC/F-actin intensity ratio at ID (C, n=27 in each group) and PJ (F, n=11 in each group). (G) Immuno-fluorescence images of suspended cells after 2.5 h of culturing show endogenous pMLC (red) and MLC (green) in MCF7 cells. (H and I) Quantification of pMLC/MLC intensity ratio at ID (H, n=10, 5, 5) and PJ (I, n=6, 5, 5). Scale bar = 5 μm. ED, Engulfing cell distal region; CC, cell-cell contact site; ID, Invading cell distal region; PJ, peripheral junction. Significance was determined using unpaired two-tailed *t*-test. \*\*\**p* < 0.001, \*\**p* < 0.01, \**p* < 0.05. (J) Quantification of entotic cells cultured for 4 h in MLCK inhibitors, P18 (10 μM) and SOC channel inhibitor, SKF-96365 (10 μM). Data represent mean ± SEM of triplicate experiments (n > 300 in each experimental group). Statistical analysis was performed using one-way ANOVA followed by Dunnett's test. \*\*\**p* < 0.001. ns, not significant. (K) Quantification of entotic cells in *Orai1* KO MCF7 cell with MLCK inhibitors, ML-9 (10 μM) and P18 (10 μM). Significance was determined using unpaired two-tailed *t*-test. ns, not significant. Data represent mean ± SEM of triplicate experiments (n > 300 in each experimental group). (L) Immuno-fluorescence images of suspended cells after 2.5 h of culturing show endogenous pMLC (red) and MLC (green) in MCF7 cells. (M) Quantification of pMLC/MLC intensity ratio at ID (n = 28, 20, 19). Statistical analysis was performed using one-way ANOVA followed by Dunnett's test. \*\*\**p* < 0.001. ns, not significant. Scale bar = 5 μm. ED, Engulfing cell distal region; CC, cell-cell contact site; ID, Invading cell distal region; PJ, peripheral junction.

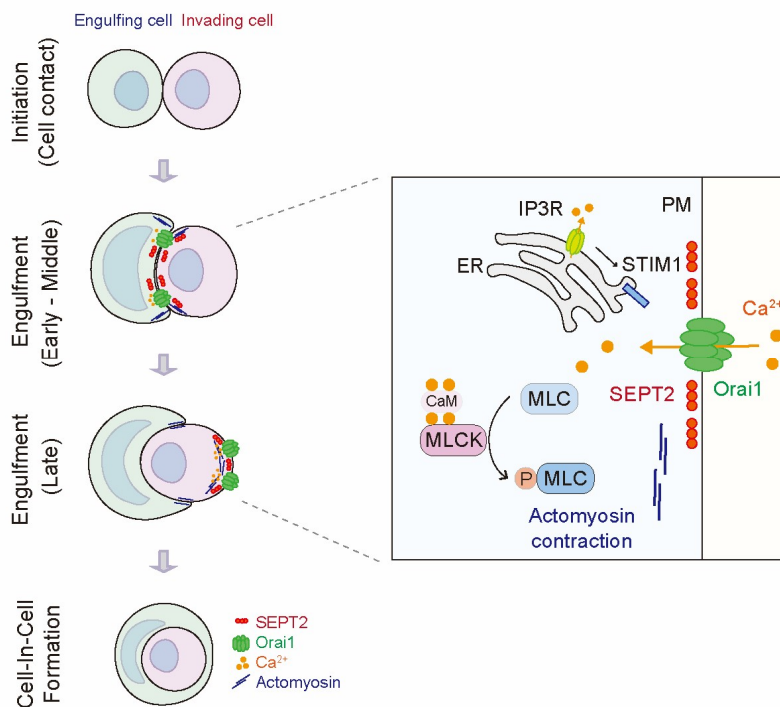


**Figure 18. Intracellular Ca<sup>2+</sup> signaling regulates entosis via SEPTIN-Orai1-Ca<sup>2+</sup>/CaM-MLCK-actomyosin axis.**



## 1.4. Discussion

In this study, I demonstrated that Orai1 is a critical  $\text{Ca}^{2+}$  channel that induces  $\text{Ca}^{2+}$  oscillations during entosis. Orai1 channel is the main pore subunit, but it has two mammalian homologs, Orai2 and Orai3. And Orai1 channel functions as the homomeric or heteromeric channel with other Orai members. Particularly, Orai3 has emerged as a potential fine-tuner for  $\text{Ca}^{2+}$  signaling in a variety of cancer cells, including breast cancer cells MCF7 (42). Furthermore, several TRP channels were found to have a cooperative function with Orai1 in cancer physiology (43, 44), however, their function during entosis remains unknown.  $\text{Ca}^{2+}$  signaling mediated by Orai1 is also modulated by several STIM and Orai binding proteins, especially calcium-dependent proteins such as CaM(45), SARAF(46), EFHB(47), Cortactin(33, 48), etc. It is, therefore, necessary to investigate the role of Orai1 interacting proteins in entosis in the future.

SOCE activation is dependent on intra-ER  $\text{Ca}^{2+}$  signaling through  $\text{IP}_3\text{R}$ , which leads to  $\text{Ca}^{2+}$  oscillations during entosis. Entosis is induced via matrix detachment and formation of adherens junctions, which may activate Orai1-mediated  $\text{Ca}^{2+}$  signaling. It has been reported that E-cadherin ligation stabilizes and activates epidermal growth factor receptor (EGFR) signaling (49-51) and activation of EGFR may result in the activation of PLC $\gamma$  and ER  $\text{Ca}^{2+}$  depletion, resulting in Orai1 mediated  $\text{Ca}^{2+}$  influx (52). However, several lines of evidence demonstrate that, despite the small conductance of Orai  $\text{Ca}^{2+}$  channels and high  $\text{Ca}^{2+}$  selectivity, all Orai isoforms are not non-redundant for the diversity of  $\text{Ca}^{2+}$  signaling/oscillations (53) and all SOCE components are independently involved in the generation of  $\text{Ca}^{2+}$  oscillations. Through activation of physical receptors, the diversity of  $\text{Ca}^{2+}$  oscillations can be expanded, including activation of Src for cancer invasion and fine-tuning transcriptional activation of the  $\text{Ca}^{2+}$ -dependent transcription factor NFAT (54, 55). Considering that  $\text{Ca}^{2+}$  oscillations are influenced by positive and negative feedback effects on the  $\text{Ca}^{2+}$  release system, which result in fluctuations in  $\text{IP}_3$  levels or changes in  $\text{Ca}^{2+}$  channel activity in intracellular stores (56-58). Moreover,  $\text{IP}_3$  stimulates the  $\text{IP}_3$  receptor ( $\text{IP}_3\text{R}$ ) and triggers  $\text{Ca}^{2+}$  release from the ER, leading to  $\text{Ca}^{2+}$  influx mediated by Orai1. Together with my observations that  $\text{IP}_3\text{R}$  inhibitor and SERCA inhibitors reduce the entosis efficiency and  $\text{Ca}^{2+}$  level during entosis. Therefore, it is reasonable to conclude that the  $\text{Ca}^{2+}$  spikes/oscillations, I observed in entosis, would be  $\text{IP}_3$ -dependent  $\text{Ca}^{2+}$  oscillations (which last tens to hundreds of seconds), which are associated with the functional coupling between ER  $\text{Ca}^{2+}$  channels ( $\text{IP}_3\text{Rs}$ ) and PM Orai  $\text{Ca}^{2+}$  channels.

During CIC formation, Orai1-mediated  $\text{Ca}^{2+}$  oscillations occur primarily during the early to the mid-engulfment stage. It is a question inherent in results that few  $\text{Ca}^{2+}$  oscillations were observed in entotic cells following the formation of complete CIC structures ((Figure 4D and F). Furthermore, I observed that invading cells displayed  $\text{Ca}^{2+}$  oscillations during the escape process from CIC structures, implying

that  $\text{Ca}^{2+}$  signaling is also necessary for escape, one of the fates of invading cells. Considering that morphological changes in escaping invading cells require cytoskeletal rearrangement, which requires  $\text{Ca}^{2+}$  signals, validation of  $\text{Ca}^{2+}$  signals in CIC structures would be of interest in determining the fate of entotic cells.

*Orai1* KO cells showed a reduced entosis with a dramatic decrease in  $\text{Ca}^{2+}$  oscillations (Figure 3E-G), implying that *Orai1*-mediated  $\text{Ca}^{2+}$  oscillations might be critical but not absolutely essential for entosis. I cannot exclude the possibility of the existence of different types/patterns of  $\text{Ca}^{2+}$  oscillations or undetectable levels of  $\text{Ca}^{2+}$  oscillations of varying sizes, intensities, shapes, frequencies, and local distributions, caused by other unrecognized  $\text{Ca}^{2+}$  pumps, channels, or *Orai* isoforms (*Orai2* and *Orai3*) present in many types of cells, including MCF7. MCF7 cells express not only *Orai1* but also other  $\text{Ca}^{2+}$  channels (such as *Orai2*, *Orai3*, and TRPC channels) which can be involved in  $\text{Ca}^{2+}$  signaling during the entosis, however, there are no studies about  $\text{Ca}^{2+}$  channel mediated signalings and whether these  $\text{Ca}^{2+}$  signalings may or may not be detected levels of oscillations. Thus, further study is needed to expand this understanding on how diverse  $\text{Ca}^{2+}$  signalings are involved in entosis.

It is important to note that both extracellular and intracellular  $\text{Ca}^{2+}$  ions and signalings are absolutely essential, particularly during the early stages of engulfment. First, in the absence of extracellular  $\text{Ca}^{2+}$ ,  $\text{Ca}^{2+}$  oscillations did not appear, and entosis occurred very rarely in WT MCF7 cells (less than 1%, Figure 3E-H). Second, when extracellular and intracellular  $\text{Ca}^{2+}$  were removed from entotic cells which are undergoing entosis, entotic cells ceased to undergo entosis and returned to single cells (Figure 5E and F). Moreover, the  $\text{Ca}^{2+}$  ions and oscillations are not critical for the late state, which is determined by more than 2/3 of the engulfment state, since entotic cells are still able to form cell-in-cell structures even when the  $\text{Ca}^{2+}$  is withdrawn (Figure 5G) (11). Thus, entosis can be triggered by a variety of signaling events, including physical cell-cell contact by cadherins and  $\text{Ca}^{2+}$  signaling by  $\text{Ca}^{2+}$ -handling proteins. Furthermore, during various stages of entosis, individual entotic cells employ a variety of but unknown signaling events; additionally how *Orai1* and other channels cooperate in the progress of entosis will require further investigation.

## Part 2. Human coronavirus 3CL proteases cleave Septins and disrupt Hedgehog signaling, causing ciliary dysfunction.

### 2.1. Introduction

The coronavirus disease 2019 (COVID-19) pandemic, caused by the severe acute respiratory syndrome coronavirus 2 (SARS-CoV-2), remains a global public health emergency (59, 60). Considering the lethality of SARS-CoV-2, it is crucial to understand its cytotoxic effects, the pathogenesis of COVID-19, and effective antiviral therapies (61). Coronaviruses comprise a positive single-stranded RNA genome of approximately 30 kb and structural and nonstructural (NSP) proteins (62). Upon cell entry, coronavirus genomic RNA (gRNA) is translated into a polyprotein and then further processed by papain-like (PLpro, NSP3) (63) and picornavirus 3C-like (3CLpro, main proteinase, NSP5) proteases (64, 65) to generate mature NSPs, providing the functional diversity needed for the viral life cycle. After infecting host cells, coronaviruses hijack host machinery for viral RNA synthesis and translation, evade immune detection by inhibiting host transcription and translation by multiple NSPs (e.g., SARS-CoV-2 NSP1, NSP14, ORF6), and promote protein degradation by NSP3 and NSP5. These multiple strategies enable thousands of new coronaviruses to accumulate inside a cell eventually leading to the cell bursting (66) (Figure 19).

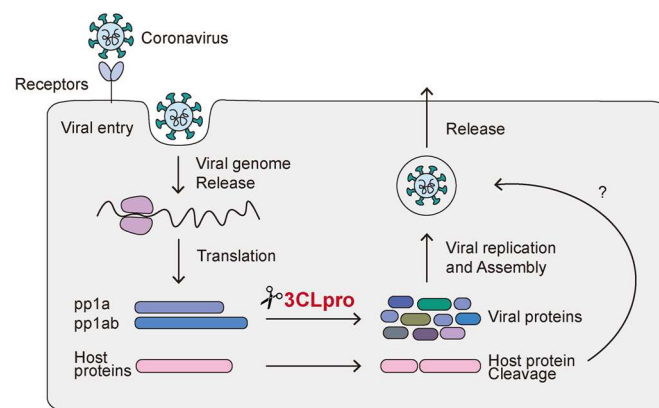


**Figure 19. Coronavirus life cycle stages and 3CL protease.**

When the virus enters a cell, the genomic RNA is translated into a polyprotein. This polyprotein is subsequently processed by 3CLpro, which plays a crucial role in generating mature NSPs for the viral life cycle. The 3CL protease cleaves host proteins if they have the same sequence specificity with viral proteins.

The development of potential antivirals for coronaviruses, including SARS-CoV-2, is urgently needed to prevent hospitalization and death. Considering the essential role and importance of 3CL proteases,



the opportunity for the development of 3CL protease inhibitors as attractive antiviral drugs, has arisen (67). Efforts were made to identify potent 3CL protease inhibitors of SARS-CoV-2, which led to the development of Paxlovid (ritonavir-boosted nirmatrelvir), produced by improving PF-00835231, as an antiviral drug for the SARS-CoV-1 outbreak in 2002 (68). Although Paxlovid reduces mortality by 89%, it remains unclear how 3CL proteinase inhibitors provide an advantage to infected cells or which are the molecular targets in the host cells.

A cilium is a membranous protrusion through which cells receive extracellular signals and which require a microtubule-based cytoskeleton called an axoneme (69). Septins alter tubulin dynamics, suggesting that SEPTs might be structural components of an axoneme (70). The primary cilium is a signaling hub involved in regulating key pathways during development and homeostasis (71). Furthermore, cilia participate in host–virus interactions, as noticed in influenza virus, zika virus, and respiratory syncytial virus (72, 73) and they are covered in mucus, which traps and eliminates pathogens (74).

Most human coronaviruses (229E, OC43, MERS, and SARS-CoV-2) infect ciliated cells in the tissues of nasal epithelia and in the respiratory system as their primary targets (75). These cells display specific interactions between the virus and their receptors such as Angiotensin-Converting Enzyme 2 (76), Dipeptidyl Peptidase 4 (77), and glycan receptor carrying 9-O-acetylated sialic acid (78). Cilia that contribute to the resistance and removal of pathogens in the airways reportedly decline after infection with human coronaviruses, including common cold viruses (HCoV-229E, -OC43 and -HKU1, etc.) and SARS-CoV-2 (75, 79-81). Thus, coronavirus-induced ciliary damage complicates the removal of pathogens from their airways (82).

Recently, Wang et al. demonstrated the mechanism for cilia loss by showing that SARS-CoV-2 ORF10 binds to ZYG11B which induces the degradation of several ciliary proteins (e.g., IFT46) by enhanced CUL2<sup>ZYG11B</sup> E3 ligase activity, leading to cilia dysfunction (83). However, there are no data currently available that support the idea that the protein or subgenomic RNA (sgRNA) of SARS-CoV-2 ORF10 is expressed in the cells during SARS-CoV-2 infection (84, 85). Even though evidence suggests that the loss of ciliary function may contribute to viral infection, replication, and spread, the mechanism by which coronaviruses induce ciliary defects remains unclear.

Eukaryotic cells possess cytoskeletons, including actin filaments (AF), microtubules (MT), and intermediate filaments (IF), which allow them to perform multiple functions simultaneously, including coordination forces for movement and shape change, transporting vesicles through the cytoplasm, and spatially organizing content (86). During coronavirus infection, the cytoskeleton may undergo reconfiguration in accordance with the successive stages of the virus life cycle, such as entry, assembly,

and egress from the host cell (87, 88). Further, it has been noticed that different viruses use disparate strategies and cytoskeleton types, suggesting that viral strategies evolved independently (60).

Numerous studies have demonstrated that there are three cytoskeleton components (AF, MT, and IF) hijacked by and heavily involved in the pathological damages caused by coronaviruses (87). Septins, the fourth type of cytoskeleton filament, are highly conserved guanosine-5'-triphosphate-binding proteins that hetero-oligomerize with cellular membranes and other cytoskeletons (26). Septins orchestrate various cellular processes including cytokinesis, cell migration, cell polarity, and cell-pathogen interactions (89-92). Additionally, they act as diffusion barriers for membrane proteins and multimolecular scaffolds that recruit various signaling components (40, 93). Based on the sequence homology, the 13 mammalian septin genes are classified into four groups, the septin-2 (SEPT1, -2, -4, -5), septin-3 (SEPT3, -9, -12), septin-6 (SEPT6, -8, -10, -11, -14), and septin-7 (SEPT7) groups (26). The protein complexes of each of these groups are arranged into ordered apolar structures (94, 95). The molecular mediators and the structure of cilia are reportedly closely related to septin function and location within the cell (70). SEPT2, SEPT7, and SEPT9 were co-localized along the axoneme in primary cilia and influenced ciliary length, while depletion of septins resulted in the loss of cilia and impaired ciliary function (96, 97). Due to the wide range of cellular functions of septin, its dysfunction is linked to a variety of human diseases such as cancer and Zika-virus induced neurodegenerative diseases (98).

Herein, I show that septins are cleaved by human coronavirus OC43 (HCoV-OC43) infection and 3CL proteases of all human-infectious coronaviruses including SARS-CoV-2, resulting in the defective, shortened cilia seen in coronavirus-infected cells, and dysregulated SHH signaling in ciliated cells, which has not been previously reported. Overall, these results provide strong evidence that septins are the unrevealed host factors of human coronaviruses and the role of septins in viral pathogenesis and innate immunity is elucidated.

## 2.2. Materials and Methods

### 2.2.1. Cell culture and transfection

HEK293T cells were obtained from ATCC (Manassas, VA, USA; CRL-1573) and cultured in Dulbecco's Modified Eagle's Medium (DMEM) supplemented with 10% fetal bovine serum (FBS) at 37°C in 5% CO<sub>2</sub>. HEK293T cells were transfected at 70% confluency with 0.2–2 µg DNA using Jet Prime (Polyplus, 101000001). hRPE-1 SMO-GFP was gifted from the laboratory of Prof. TJ Park at the Ulsan National Institute of Science and Technology. hTERT-RPE1 cells were obtained from ATCC (CRL-4000). The cells were cultured in DMEM mixed with Ham's F12 modified medium (DMEM/F12) supplemented with 10% FBS at 37°C in 5% CO<sub>2</sub>. For transient transfection, RPE-1 cells were transfected at 70% confluency with 0.5–3 µg DNA using FuGeneHD (Promega Madison, WI, USA). NIH-3T3 cells were obtained from ATCC (CRL-1658) and cultured in DMEM supplemented with 10% bovine calf serum (BCS) at 37°C in 5% CO<sub>2</sub> and transfected at 50% confluency with 0.5–3 µg DNA using Lipofectamine 3000 (Invitrogen, Waltham, MA, USA; L3000-015) according to the manufacturer's instructions. Vero E6 cells were gifted from the laboratory of Prof. NH Cho at the Department of Biomedical Sciences, Seoul National University. MRC-5 cells were obtained from ATCC (CCL-171) and were cultured in Eagle's Minimum Essential Medium supplemented with 10% FBS at 37°C in 5% CO<sub>2</sub>.

### 2.2.2. Corona Virus infection

HCoV-OC43 was purchased from Korea Bank for Pathogenic Viruses (Seoul, Korea). The number of infectious OC43 particles was determined by focus-forming immunoassays on Vero-E6 cells or hTERT-RPE1 cells. For these assays, Vero-E6 or RPE1 cells were seeded in 12-well plates and, after 24 h, were infected with 10-fold serial dilutions of the OC43. At 2 h post-infection (hpi), an overlay of 1% low melting agarose prepared in DMEM or DMEM/F12. Infected cells were incubated at 33°C in 5% CO<sub>2</sub> for 1 day, then fixed and processed for immunofluorescence to detect HCoV-OC43 nucleoprotein. Cells were incubated with primary mouse IgG anti-coronavirus group antibody MAB9012 (MilliporeSigma, Burlington, MA, USA; diluted 1:500) for 2 h at 25°C, followed by addition of secondary Alexa Fluor 594 anti-mouse antibody for 30 min at room temperature. Foci were visualized and counted under a fluorescence microscope (In Cell Analyzer 2500; Cytiva, Marlborough, MA, USA).

HEK293T cells were incubated with OC43 for 48 h at a multiplicity of infection (MOI) of 50. At 48 hpi, cells were lysed and subjected to western blot detection. hTERT-RPE1 and NIH-3T3 cells were incubated with OC43 for 2 h at an MOI of 20 to 40. After removing the infectious liquid, the cells were

washed with no-serum medium and maintained in a culture medium. At 24 or 48 hpi, cells were fixed and subjected to immunofluorescence detection.

### **2.2.3. Lentivirus-mediated stable cell line construction**

HEK293T cells were seeded into 12-well plates with  $2 \times 10^5$  cells/ml. Transfection was performed with lentiviral constructs (GFP, GFP-SEPT2 FL, NT and -CT, and FM-SEPT2) together with packaging plasmids (VSVg, p8.2). At 48 h post-transfection, supernatants were collected. hRPE1, NIH-3T3 cells were infected with the lentivirus-containing medium for 48 h.

### **2.2.4. Immunofluorescent staining or Immunocytochemistry**

hTERT-RPE1 cells (GFP-SEPTs and SMO-GFP stable cell lines) were cultured on 0.2% gelatin (Sigma-Aldrich, St. Louis, MO, USA, G1393) coated 15 mm round cover glass in media containing 10% FBS at 37°C and 5% CO<sub>2</sub> overnight, and then starved for 24 h in DMEM/F12 without FBS to induce cilia. NIH-3T3 cells were grown on 2.5% collagen (Gibco, Carlsbad, CA, USA; A10644-01) coated 15 mm cover glass and cultured at 37°C in media containing 10% BCS overnight, and then starved for 24 h in DMEM without BCS to induce cilia. Cilia induced cells were fixed in 4% paraformaldehyde for 10 min at room temperature, washed three times with phosphate-buffered saline (PBS), permeabilized in 0.1% triton-X100 for 10 min at room temperature, washed with PBS three times, blocked in 3% BSA at room temperature for 2 h and incubated with primary antibodies at 4°C for overnight. The cells were washed three times with PBS and stained with secondary antibodies at room temperature for 1 h and mounted with Aqua Poly/Mount solution (Polyscience, Niles, IL, USA; 18606) at room temperature. The cells were imaged using IX83 microscope equipped with an Olympus x60 objective lens (oil, NA 1.30), fluorescent lamp (Olympus, Tokyo, Japan), stage controller (LEP), and CCD camera (ANDOR, Belfast, UK). Images were analyzed using Metamorph software.

### **2.2.5. Antibodies and protein detection**

SEPT2 (Proteintech, Rosemont, IL, USA; 60075-1-Ig), SEPT7 (Proteintech; 13818-I-AP), SEPT9 (Novusbio, Centennial, CO, USA; NBP1-28764), GAPDH (Proteintech; 60004-1-Ig),  $\beta$ -actin (Proteintech; 66009-1-Ig), myc (MilliporeSigma; 05-724 (4A6)), tubulin (SIGMA; T6074), FLAG M2 (SIGMA, F1804), Acetylated tubulin (SIGMA; T7451), Acetylated tubulin (D20G3) (Cell Signaling Technology Danvers, MA, USA; 5335), TTBK2 (Proteintech; 15072-1-AP), SARS-CoV 3CLProtease (ROCKLAND; 200-401-A51), coronavirus (MilliporeSigma; MAB9012).

### **2.2.6. Confocal microscopy**

SEPTs and acetylated  $\alpha$ -tubulin stained cilia were imaged using a LSM780 NLO and LSM980 (Zeiss, Oberkochen, Germany) confocal microscope with a x63 1.4 NA objective (Plan-Apochromat) or x100 1.46 NA objective. Zen software (Zeiss) was used for image acquisition. Images were analyzed using Zen or ImageJ software. All experiments were performed at 25°C.

### **2.2.7. Structured Illumination Microscopy zeiss ELYRA S.1**

SEPTs and acetylated  $\alpha$ -tubulin stained cilia were imaged using super-resolution structured illumination microscopy (SR-SIM). Samples were imaged on a Zeiss ELYRA S.1 microscope with a x100/1.46 Oil objective. Maximum intensity projections in the z-axis were used to generate intensity profiles perpendicular to the axoneme close to the base and tip of individual primary cilia.

### **2.2.8. Immunoprecipitation and Immunoblot analysis**

Cells were lysed by 50 mM Tris-HCL pH 7.5, 150 mM NaCl, 1% Triton X-100 (0.1% SDS). Lysates were centrifuged at 12,000 rpm at 4°C for 10 min and the supernatant was incubated at 4°C with anti-Flag M2 agarose beads (MilliporeSigma; A2220) overnight. Lysates and immunoprecipitated samples were mixed with 1/4 or 1/2 volume of 4X reducing sample buffer (0.2 M Tris-HCL pH 6.8, 8% SDS, 0.4% Bromophenol blue, 40% glycerol) and boiled at 95°C for 5 min. Samples were separated on 10% polyacrylamide SDS-PAGE gels and transferred onto 0.45  $\mu$ m pore size PVDF membrane (Immobilon-P, MilliporeSigma). The membrane was blocked into TBS-T plus 7% skim milk and incubated overnight at 4°C with primary antibodies diluted in TBS-T plus 3% BSA. Blots were incubated with horseradish peroxidase (HRP)-conjugated secondary antibody and detected by enhanced chemiluminescence (Pierce). Densitometry analysis was carried out using ImageJ software (NIH). Fold change relative to control was calculated using the septins:GPADH ratio.

MG132 (Sigma-Aldrich, M8699) was used as proteasome inhibitor. GC376 (Biosynth, Staad, Switzerland; BG167367) and PF00835231 (Selleckchem, Houston, TX, USA; S9731) were used for 3CL protease inhibition.

### **2.2.9. Luciferase assay**

NIH-3T3 cells were co-transfected with the indicated luciferase constructs 8x Gli luciferase reporter (gifted from the laboratory of Prof. KY Shin at Department of Biological Sciences, Seoul National

University) and the Renilla luciferase gene (pRL-TK), used as an internal control for cell number and transfection efficiency. After 18 h, the medium was replaced with serum-free DMEM with 120 nM SAG (smoothed agonist; Sigma-Aldrich; 566660) and induced starvation for 24 h. GLI luciferase assays were performed by the Dual luciferase Reporter assay system (Promega). For each condition, luciferase activity was measured with samples taken from triplicate wells with a 96-well automated luminometer (BioRad, Hercules, CA, USA). Results are calculated as the ratio of firefly to Renilla luciferase activity.

### 2.2.10. RNA isolation and Quantitative Real-Time PCR

Total RNA was isolated with RiboEx (GeneAll Biotechnology Co., Ltd., Seoul, Korea) according to the manufacturer's instructions. One microgram of RNA was used per reverse transcribed using oligo (dT) primers and First Strand cDNA synthesis Kit (ToYoBo, Osaka, Japan). For quantitative real-time polymerase chain reaction analysis was performed using the SYBR green method. Synthesized cDNA and SYBR Green Master Mix (ToYoBo) were run on a LightCycler480 II (Roche, Basel, Switzerland). Relative expression levels of mRNA were calculated using the 2-Ct method. The following primers were used: mGli1 (For: 5-TCGACCTGCAAACCGTAATCC-3, Rev: 5-TCCTAAAGAAGGGCTCATGGTA-3), mPTCH1 (For: 5-AACAAAAATTCAACCAAACCTC-3, Rev: 5-TGTCTTCATTCCAGTTGATGTG-3), OC43 nucleocapsid (For: 5-AGCAACCAGGCTGATGTCAATACC-3, Rev: 5-AGCAGACCTTCCTGAGCCTTCAAT-3), mIFN beta (For: 5-AACCTCACCTACAGGGCGGACTTCA-3, Rev: 5-TCCCACGTCAATCTTTCCTCTTGCTTT-3), mGAPDH (For: 5-TGCACCACCAACTGCTTAG-3, Rev: 5-GATGCAGGGATGATGTTTC3).

### 2.2.11. Plasmids

pLTE-Flag-Myc-SEPT2, pLTE-Flag-Myc-SEPT2-Q340E, pLTE-GFP-SEPT2, pLTE-GFP-SEPT6, pLTE-GFP-SEPT6-Q82E, pLTE-Flag-Myc-SEPT7, pLTE-Flag-Myc-SEPT9, pLTE-GFP-SEPT2-NT(1-340), pLTE-GFP-SEPT2-CT(341-362), pLTE-Flag-Myc-SEPT2-NT(1-340), pLVX-EF1alpha-SARS-CoV-2-nsp5-2xStrep-IRES-Puro (Addgene, Watertown, MA, USA; #141370), pLVX-EF1alpha-SARS-CoV-2-nsp5-C145A-2xStrep-IRES-Puro (Addgene; #141371), pLEX307-HCoV-NL63-3CLp (Addgene; #160286), pLEX307-Bat-CoV-HKU9-3CLp (Addgene; #160284), pLTe-FM-229E-3CLp, pLTe-FM-OC43-3CLp, pUC57-HKU1-3CLpro, GST-3CLp substrate-GFP.

### 2.2.12. Statistics

A student's t-test determines statistical significance between two groups. All results were analyzed with GraphPad Prism5 (GraphPad Software, San Diego, CA, USA). Results are presented as means  $\pm$  SEM. P-value of  $< 0.05$  is considered significant: \* $P < 0.05$ , \*\* $P < 0.01$  and \*\*\* $P < 0.001$ .



## 2.3. Results

### 2.3.1. Coronavirus infection and 3CL Proteases cleave septins

Most viruses use cytoskeletal functions to complete their life cycle of infection. Generally, cytoskeletons are the essential host factors of viral infections for transporting viral components to designated subcellular compartment sites of translation, replication, and reorganization of where mandatory intracellular processes of viral infection from entry to secretion occur. Research over the last decade also suggests that coronaviruses require cytoskeletal functions during their replication cycle. For instance, many studies have shown that actin polymerization and actin rearrangement, MT stability, and vimentin-mediated epithelial-mesenchymal transition pathogenesis and fibrosis can be altered by alpha-coronavirus TGEV (99), MHV (100), and beta-coronavirus SARS-CoV (101, 102), respectively.

Although septins are recognized as the fourth component of the cytoskeleton, the role of septins has not been studied during coronavirus infection. We, therefore, investigated whether the coronavirus could target cytoskeleton components during infection. The protein expression of individual elements (actin, tubulin, and septin) was measured using a western blot of HEK293T cells at an MOI of 50 for 48 hpi. Surprisingly, I noticed a reduced expression level and a slightly lower band of SEPT2 in the coronavirus OC43-infected HEK293T cells, but not in the uninfected cells. In contrast, other cytoskeletal elements (actin and microtubules) did not show a distinguishable difference in either infected or uninfected HEK293T cells (Figure 20A). This was likely due to the abundance and stability, among other characteristics, of cytoskeletal elements. Interestingly, I also found a slightly lower band of SEPT2 following OC43 coronavirus infection, which was found not to be an outcome of protein degradation because a proteasome inhibitor (MG132, 10  $\mu$ M) failed to prevent it (Figure 20B). These results led us to speculate that it is likely that the reduced band of SEPT2 was caused by a coronavirus protease rather than host protease factors. Reduced expression level and slightly lower band of SEPT2 was also detected in SARS-CoV-2 infected HEK293T-ACE2 cells (Figure 20C). Therefore, I investigated whether SEPT2 could be an unrecognized target of coronavirus 3CL proteases (known as Mpro and NSP5) in mediating the outcome of viral infection in host cells. First, I determined whether the endogenous SEPTs were targeted by transiently expressing either SARS-CoV-2 3CL protease (3CLpro) wild-type (WT) or the catalytic mutant C145A (103) in HEK293T cells. Like that of HCoV-OC43 coronavirus infection, the cells expressing 3CLpro WT, but not 3CLpro C145A, showed a reduced full-length band and a slightly down-shifted band of SEPT2 and SEPT9 using anti-SEPT2 and anti-SEPT9 antibodies, respectively (Figure 20D). I confirmed that Flag-Myc-tagged SEPT2 exhibited a reduced intensity of full-length SEPT2 and a cleaved band below the full-length SEPT2 in cells expressing 3CLpro WT but not in a catalytic mutant (C145A) (Figure 20E). Moreover, SEPT2 cleavage by 3CLpro in HEK293T cell was prevented by 3CLpro inhibitors, GC-376 (30  $\mu$ M) and PF-00835231 (20  $\mu$ M)



(Figure 20F). These results suggest that SEPT2 could be a direct cleavage target of 3CLpro during coronavirus infection.

I next checked whether and which septin members could be cleaved by SARS-CoV-2 3CLpro. Among 13 family members, three representative septin members (septin-6, -7, and -9) were chosen from three other subgroups (septin-6, -7, and -3 subgroups), respectively. HEK293T cells were transfected with GFP-SEPT6, FM-SEPT7, and FM-SEPT9, with either no-tagged WT or mutant 3CLpro to fully reconstitute the protease activity. Interestingly, similar results were observed in the cells expressing 3CLpro WT and SEPT6 (Figure 20G) or SEPT9 (Figure 20H) with reduced full-length proteins and cleaved forms of septins. Further, no cleaved forms of SEPT6 and SEPT9 were observed in cells expressing the proteolytically inactive mutant 3CLpro (C145A), indicating that the cleavage product was 3CLpro activity-dependent (Figure 20G and H). However, I was unable to observe either the reduced full-length or the cleaved form of SEPT7 in cells expressing 3CLpro WT (Figure 20I).

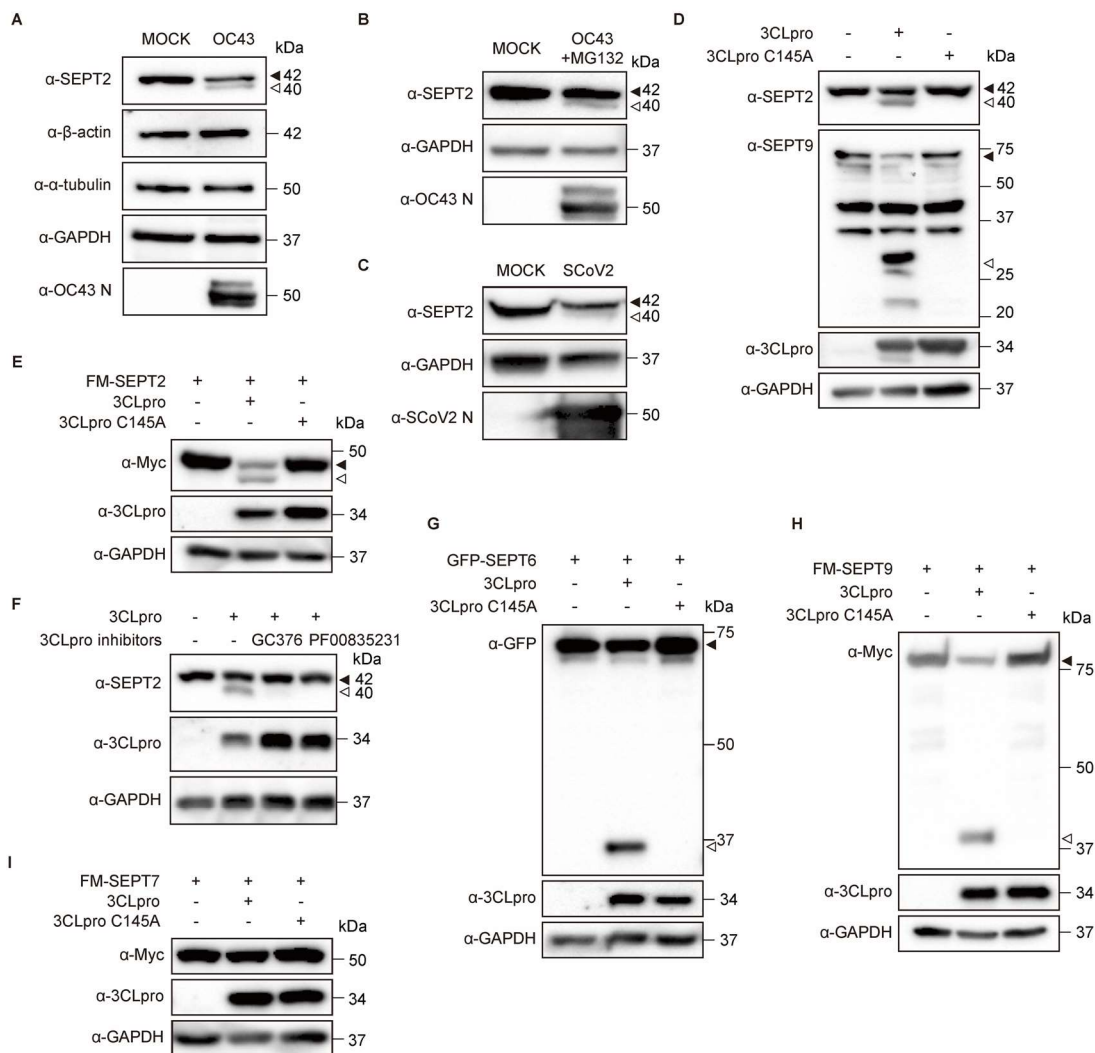


**Figure 20. Coronavirus infection and 3CL Proteases cleave septins.**

(A) HEK293T cells were infected with HCoV-OC43 at an MOI of 50 for 48 h. Infected (OC43) or noninfected (mock) cells were lysed and analyzed by western blot for SEPT2,  $\beta$ -actin,  $\alpha$ -tubulin, GAPDH, and OC43 N protein. OC43 infected cell lysate produced the reduced full-length SEPT2 (42kDa, filled arrowhead) and a new band with a slightly lower size (40kDa) (open arrowhead). (B) HEK293T cells were infected with HCoV-OC43 at an MOI of 50 for 24 h and treated with the proteasome inhibitor MG132 (10  $\mu$ M) for an additional 24 h. Infected (OC43) or noninfected (mock) cells were lysed and analyzed by western blot for SEPT2, GAPDH and OC43 N protein. OC43 infected cell lysate produced the reduced full-length SEPT2 (42kDa, filled arrowhead) and a new band with a slightly lower size (40kDa) (open arrowhead). (C) HEK293T-ACE2 cells were infected with SARS-CoV-2 at an MOI of 0.1 for 48 h. Infected (SARS-CoV-2) or noninfected (mock) cells were lysed and analyzed by western blot for SEPT2, GAPDH, and SARS-CoV-2 N protein. (D) HEK293T cells were transfected with SARS-CoV-2 3CLpro or C145A. Lysates from transfected cells were prepared for immunoblotting for SEPT2 and SEPT9. (E) Immunoblot analysis of Flag-Myc-SEPT2 with 3CLpro or

C145A in HEK293T cells. Open arrowheads denote the 3CLpro-induced cleavage product. **(F)** HEK293T cells were transfected with 3CLpro for 4 h and treated with GC376 (30  $\mu$ M), PF00835321 (20  $\mu$ M) for an additional 20 h. **(G and H)** Immunoblot analysis of the overexpression of GFP-SEPT6 **(G)**, Flag-Myc-SEPT9 **(H)** with 3CLpro or C145A in HEK293T cells. Open arrowheads denote the 3CLpro-induced cleavage product. **(I)** Immunoblot analysis of the overexpression of Flag-Myc-SEPT7 with 3CLpro or C145A in HEK293T cells. There was no cleavage of SEPT7.

### 2.3.2. Emerging coronaviruses are more potent at cleaving SEPT2.

These results suggest that some septins are the novel host targets of SARS-CoV-2 3CLpro and might alter the cytoskeleton machinery for more virus-friendly conditions in infected host cells. This led us to further explore the role of septins in viral infection. I showed that SEPT2 is cleaved by human beta coronaviruses (lineage A HCoV-OC43 and lineage B SARS-CoV-2) (Figure 20A). I then examined whether SEPT2 could be cleaved by other genera or subgenera of human coronaviruses. 3CLpro from HCoV-NL63 and -229E (Alpha), -OC43 and -HKU1 (Beta lineage A), and HKU9 (Beta lineage D) (81) were found to be isolated by either conventional PCR or gene synthesis. Furthermore, an internal 3CLpro enzymatic reporter, the GST-S2rep-GFP fusion protein was also designed by inserting the SARS-CoV-2 cleavage peptides (104, 105) (12 amino acids, TSAVLQSGFRKM, a linker region of NSP5 and NSP6) in between GST and GFP. The GST-S2rep-GFP was expressed with each subgenus of 3CL proteases in HEK293T cells, and I checked the cleavage efficiency of the endogenous SEPT2 and the GST-S2rep-GFP reporter. I observed that the cleavage efficiency of SEPT2 differed among the tested 3CL proteases; specifically, the cleavage efficiency was high in Beta lineage B (SARS-CoV-2) and Beta lineage D (HKU9), mild in Beta lineage A (OC43 and HKU1), and little or absent in Alpha (NL63 and 229E) (Figure 21A). This suggests that existing coronaviruses could target SEPT2 and other SEPTs and emerging coronaviruses (like SARS-CoV-2) are potent enough to cleave SEPT2.

Together with biochemical analysis, I predicted the potential cleavage sites of all septins by SARS-CoV-2 3CLpro by analyzing the size of cleaved bands of SEPTs. I used the NetCorona 1.0 webserver, which is a tool developed to utilize artificial neural networks to predict cleavage sites by SARS-CoV 3CLpro from amino acid sequences (106). I identified several septin family members that have high scores over 0.5 that are possible targets for SARS-CoV 3CLpro. Interestingly, SEPT2, 6, and 9, which have already been confirmed to be cleaved herein, were also predicted to be cleaved, while SEPT7 did not have a predicted cleavage site (score 0.189), which corroborated previous results (Figure 21B). With this prediction result, at least three more septins (SEPT3, 4, and 10) from three subgroups are expected to be targeted by 3CLpro, however, this hypothesis still needs validation (Figure 21B and C).

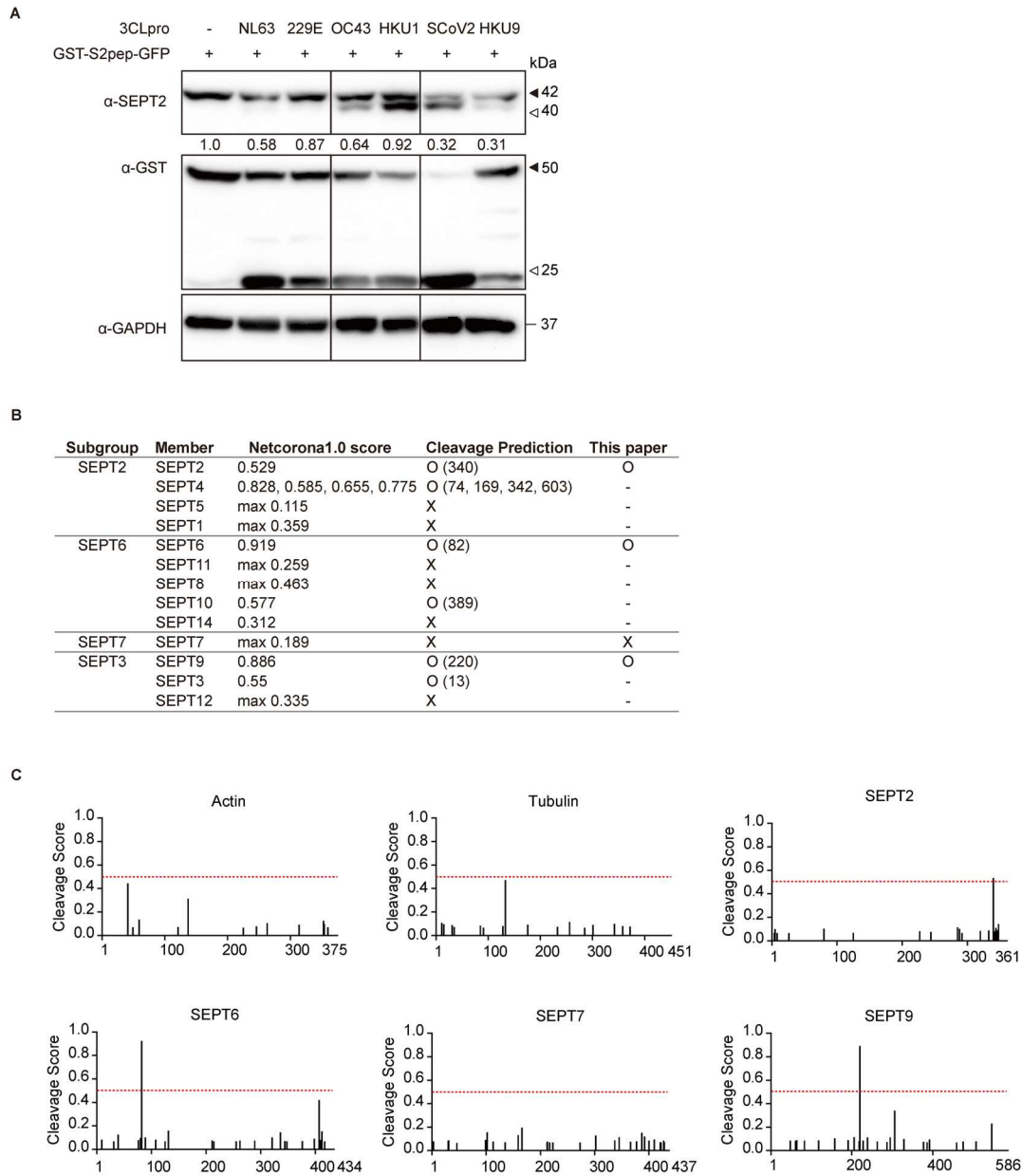


**Figure 21. Emerging coronaviruses are more potent at cleaving SEPT2.**

(A) Immunoblot of endogenous SEPT2 cleavage by 3CLpro from human coronaviruses HCoV-NL63, -229E (Alpha), -OC43, and HKU1 (Beta lineage A), and SARS-CoV-2 (Beta lineage B), and HKU9 (Beta lineage D). GFP-S2pep-GST reporter was used to validate the enzymatic activity of 3CL proteases. Open arrowheads denote the 3CLpro-induced cleavage product. (B) The prediction of cleavage sites of septins through NetCorona1.0 webserver. Values lower than the threshold (0.5) were not predicted as a potential cleavage target site. Numbers indicate the score given by the prediction program. (C) Schematic of b-actin, a-tubulin, SEPT2, SEPT7, SEPT7, and SEPT9 predicted cleavage sites. The red line indicates the threshold (0.5).

### 2.3.3. A single cleavage site of 3CL proteases is located at Q340 in SEPT2 and Q80 in SEPT6.

Based on observation of cleaved SEPT2 and SEPT6 with molecular weights reduced by a few kDa, and the NetCorona 1.0 cleavage predictions within the C-terminal region near the guanine nucleotide-binding region, I suspected one possible cleavage residue, Q340, within the coiled-coil domain in the C-terminal region of human SEPT2 and the amino acid Q80 within the N-terminal region of SEPT6 (Figure 22A and D). To verify the cleavage site of SEPT2 and SEPT6, I made 3CLpro cleavage-resistant mutants (SEPT2 Q340E and SEPT6 Q80E) by changing amino acids Q to E and expressed Flag or GFP-tagged SEPTs WT, or its mutants, with 3CLpro in HEK293T cells. Neither a reduced full-length nor cleaved form of SEPT2 and SEPT6 were detected in the cells expressing SEPT2 Q340E and SEPT6 Q80E, respectively (Figure 22B and E).

Notably, extensive diversity has been observed among the 13 septin family members during evolution. However, the homology of SEPT2 and -6 is well conserved among the different species. Analysis of the sequence homologies around the cleavage site of SEPT2 and SEPT6 by 3CLpro across species revealed that cleavage residue Q at the P1 site was highly conserved in all SEPT2s (Figure 22C), indicating that SEPT2 may be a common target protein of human and animal coronavirus serotypes following infection. Overall, these results suggest that septin members including SEPT2, -6, and -9 are the unrevealed, cleavable host targets of coronavirus 3CL proteases.

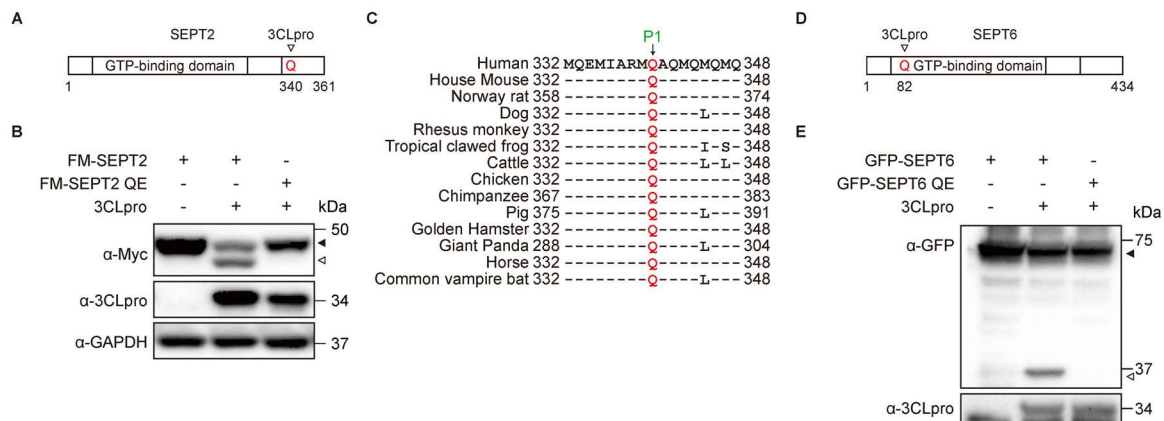


**Figure 22. A single cleavage site of 3CL proteases is located at Q340 in SEPT2 and Q80 in SEPT6.**

(A and D) Schematic of SEPT2 (A) and SEPT6 (D) showing the location of possible 3CLpro cleavage sites. (B) Immunoblot analysis for Flag-Myc-SEPT2 wild-type and the Q340E mutant in HEK293T cells transfected with either an empty vector or 3CLpro. (C) NetCorona1.0 partial sequence alignment of the C-terminal domain of SEPT2 homologs from other species. The putative cleavage sites Q are indicated in red and labeled with P1. (E) Immunoblot analysis for GFP-SEPT6 wild-type and the Q82E mutant in HEK293T cells transfected with either an empty vector or 3CLpro.

#### 2.3.4. 3CLpro affects the septin complex by cleaving several septin proteins.

Septin subgroup members form oligomeric complexes with homo and hetero interactions, which can be arranged into higher-order structures, such as filaments, sheets, or ring-like arrangements involved in a variety of biological processes. Among other members, SEPT2 has been determined to be a core component of septin filaments with an N-C interface by structural studies in SEPT(7,9)–SEPT6–SEPT2–SEPT2–SEPT6–SEPT(7,9) heteromeric complex (94). Although SEPT2 is also known to exist in solution as a dimer with a G-G interface, it is not formed in vivo (107).

Next, I investigated whether SEPT2 cleavage by 3CLpro could affect the formation of septin filaments. In HEK293T cells, I expressed Flag-Myc tagged SEPT2 and 3CLpro and immunoprecipitated SEPT2 with an anti-Flag antibody.

Interestingly, all SEPT subgroup members (SEPT2, 6, 7, and 9) were detected, which confirmed that SEPT2 itself forms a complex oligomer with the other members. However, the cells expressing 3CLpro showed weak interactions between SEPT filament components. These results imply that 3CLpro might affect the septin complex by cleaving several septin proteins, including SEPT2, 6, and 9, which results in an unstable filament structure (Figure 23A). Subsequently, I examined whether SEPT2 could form the core element by interacting with the N-C interface in the presence of 3CLpro, because a cleavage site by 3CLpro resides within the C-terminal domain of SEPT2, resulting in two cleaved SEPT2 fragments (hereafter SEPT2 NT and SEPT2 CT, Figure 24C). HEK293T cells were transfected with 3CLpro and Flag-Myc tagged SEPT2 Q340E, with GFP-tagged SEPT2 or Q340E. FM-SEPT2 Q340E was immunoprecipitated with the anti-Flag antibody and immunoblotted with the GFP antibody. As expected, both cleavage-insensitive SEPT2 proteins could form a complex. Unlike GFP-SEPT2 Q340E, most GFP-SEPT2 WT in the lysates were cleaved with a faint band in the cells expressing 3CLpro (Figure 23B, left bottom panel) but was strongly detected in the immunoprecipitants. Interestingly, I observed that a cleaved SEPT2 NT showed a relatively similar interaction to Flag-SEPT2 compared with that of GFP-SEPT2 WT (a lower band in the middle lane of the right bottom panel) (Figure 23B), indicating that a cleaved SEPT2 NT could similarly form a SEPT2 homodimer to that of two intact SEPT2 proteins.



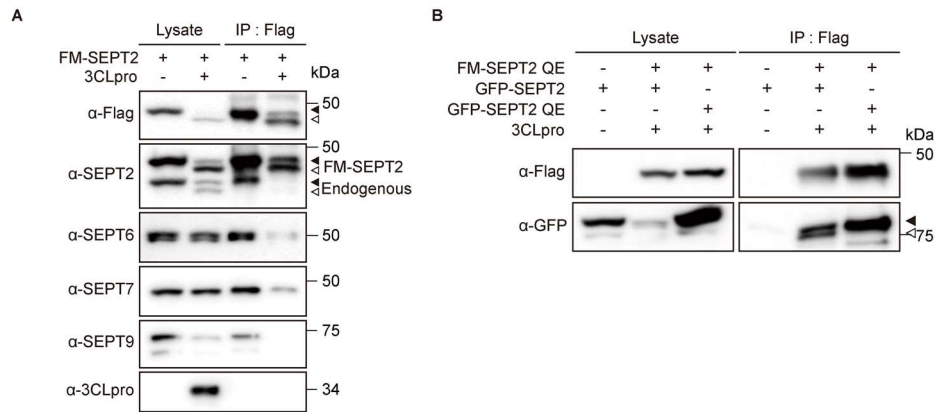


**Figure 23. 3CLpro affects the septin complex by cleaving several septin proteins.**

(A) Immunoblots of whole-cell lysates (left) or immunoprecipitates (right) from HEK293T cells expressing Flag-Myc-SEPT2 along with or without 3CLpro. (B) Immunoblots of whole-cell lysates (left) or immunoprecipitates derived (right) from HEK293T cells co-expressing Flag-SEPT2 QE and 3CLpro with GFP-SEPT2 or GFP-SEPT2 QE.

### 2.3.5. Cleaved SEPT2 NT affects the SEPT2 filament formation in non-ciliated RPE1 cells.

I checked whether a cleaved SEPT2 could be arranged into higher-order structures in cells, such as filaments or sheets. To measure the cellular distribution of SEPT2, I expressed GFP-tagged SEPT2 with 3CLpro WT or C145A mutant in HEK293T cells. I found that the length of SEPT2 filaments was significantly reduced in the presence of 3CLpro WT (Figure 24A and B). These results suggest that 3CLpro cleaves SEPT2 and shortens septin filaments associated with cleaved GFP-SEPT2 NT, indicating that a rearrangement of septin filaments is caused by higher- to lower-order structures during coronavirus infection or 3CLpro cleavage.

To understand the function of cleaved fragments during coronavirus infection, I first examined the cellular distribution of cleaved SEPT2 fragments, SEPT2 NT (amino acids 1–340) and CT (amino acids 341–361). I generated hRPE1 stable cell lines expressing GFP-tagged SEPT2 FL, NT, and CT. While GFP-SEPT2 FL exhibited the typical filament-forming structure, the cleaved fragments, SEPT2 NT (1–340) and CT (341–361), showed different distribution patterns in the free cytosol and weak filament structures, respectively, to a lesser extent than that of full-length GFP-SEPT2 (Figure 24C and D). These observations led us to examine the interaction between full-length SEPT2 and the two cleaved fragments, SEPT2 NT and CT. Flag-tagged SEPT2 was transiently expressed in HEK293T cells with GFP-tagged SEPT2 FL, NT, or CT. After immunoprecipitation with an anti-flag antibody, I found that the binding between the N-terminus and SEPT2 FL had a similar affinity to that of the full-length FM and GFP-SEPT2 dimers (Figure 24E). However, SPET2 CT (341–361) did not bind to SEPT2 FL.

I next examined the cellular distribution of SEPT2 associated with cleaved SEPT2 NT or CT. Flag-Myc tagged SEPT2 FL was introduced into hRPE1 stable cells expressing GFP-SEPT2 FL, NT, or CT. The cells expressing GFP-SEPT2 FL predominantly displayed organized filaments of the full-length FM- and GFP-SEPT2 dimers. Interestingly, I observed that the filament structure of SEPT2 FL was perturbed in the hRPE1 cells expressing GFP-SEPT2 NT but less in CT. FM-SEPTs appeared to associate with GFP-SEPT2 NT more in the cytosol and formed weaker filament structures than GFP-SEPT2 CT cells, which showed assemblies and organized filament structures (Figure 24F) throughout the cytosol, indicating that cleaved SEPT2 NT fragments could affect the filament formation of SEPT2 by disrupting SEPT2-SEPT2 homomeric interactions in non-ciliated RPE1 cells.

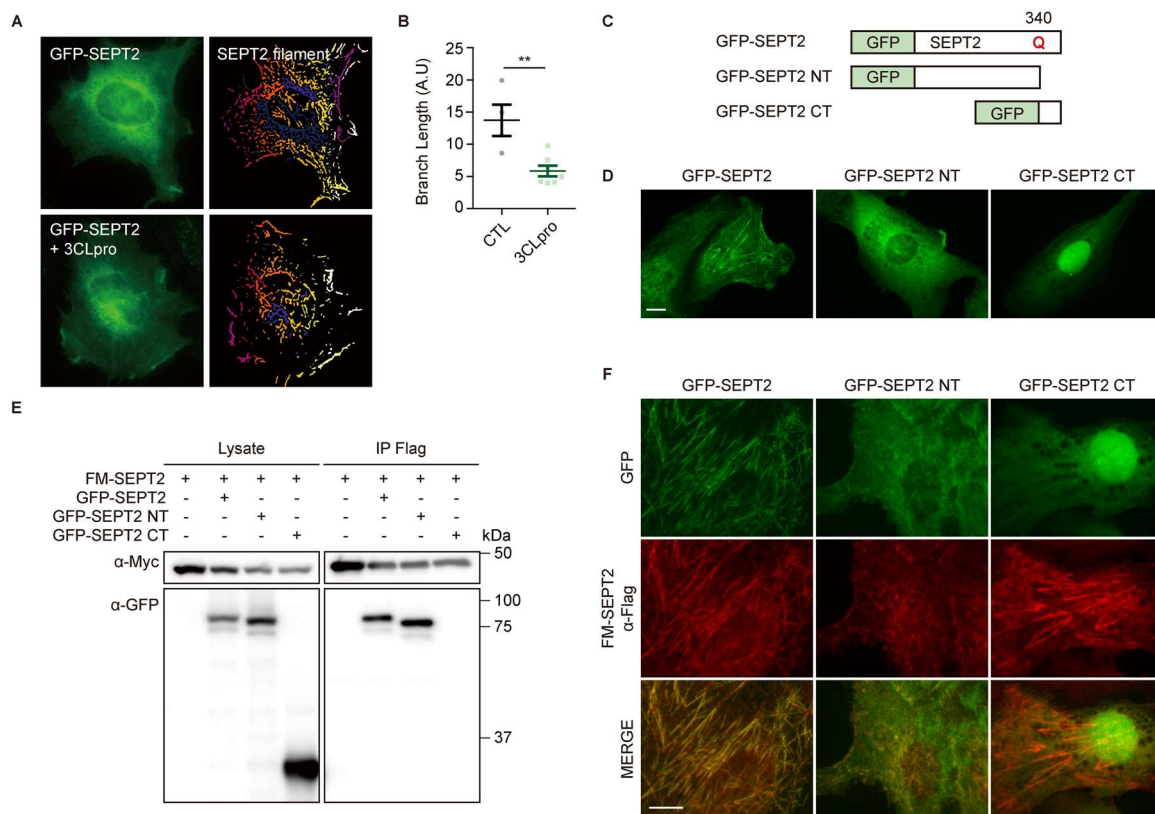


**Figure 24. Cleaved SEPT2 NT affects the SEPT2 filament formation in non-ciliated RPE1 cells.**

(A and B) The fluorescence images show that 3CLpro disrupts the cellular structure and morphology of the GFP-SEPT2 filaments (A). U2OS cells transfected with GFP-SEPT2 were analyzed using “Analyze cytoskeleton” on the ImageJ interface. After processing cells, Representative septin images and the program outputs were shown. (B) Quantification of cellular GFP-SEPT2 branch length. N = 4 and 7. (C) Schematic of cleavage fragments from SEPT2. SEPT2 FL (1-361), NT (1-340), CT (341-361). (D) Fluorescence microscopy for GFP-SEPT2 and the fragments (GFP) in lentivirus-infected hTERT-RPE1 cells. Scale bar, 10  $\mu$ m. (E) Immunoblots of whole-cell lysates (left) or immunoprecipitates (right) from co-expressing Flag-Myc-SEPT2 and GFP-SEPT2 FL, NT, or CT. (E)



Fluorescence microscopy of GFP-SEPT2 (FL, NT, and CT) and FM-SEPT2 (red) in hTERT-RPE1 cells lentivirus infected with the indicated SEPT2 constructs. Scale bar, 10  $\mu\text{m}$ . Cropped image scale bar, 2  $\mu\text{m}$ .

### **2.3.6. The cleaved SEPT2 NT interferes with septin filaments by forming homo- and heteromeric complexes with SEPT members in non-ciliary hRPE1 cells.**

It remains unclear whether the cleaved SEPT2 fragments could interfere with other septin members. Therefore, I checked whether SEPT2 NT (1–340) could form a complex with other SEPT members and compared the binding affinity to that of the full-length SEPT2. HEK293T cells expressing Flag-tagged SEPT2 FL (1–361) or NT (1–340) showed similar immunoprecipitated blots with the same intensity as that of SEPT complexes composed of endogenous SEPT6, 7, and 9 (Figure 25A), indicating that SEPT2 NT could be associated with filamentous SEPT subgroup members following competitive binding with SEPT2 FL.

I also confirmed the binding between SEPT6 and SEPT2 NT in a heteromeric complex. Either GFP-tagged SEPT2 FL or NT was successfully pulled down at a similar level as an immunoprecipitated Flag-tagged SEPT6 using an anti-Flag antibody (Figure 25B).

Together with that of SEPT2, SEPT2 CT seems not to interact with SEPT6 and other SEPT filaments (SEPT2, 7 and 9).

Next, I further investigated the filament structure composed of SEPT7 and SEPT9 to see whether the cleaved forms of SEPT2 could interfere with the filament assembly in cells. To exclude the overexpression effect of SEPT members, I examined the cellular distribution of endogenous SEPT7 and SEPT9 with an anti-SEPT7 and anti-SEPT9, respectively, in hRPE1 cells expressing GFP-tagged FL, SEPT2 NT, and SEPT2 CT. As with SEPT2 instabilities caused by the cleaved fragments (Figure 24F), the perturbed filamentous distributions were observed for SEPT7 and SEPT9 in the cells expressing SEPT2 NT but not with the full-length SEPT2 and CT (Figure 25C and D), suggesting that the SEPT2 NT may form homo- and heteromeric complexes with other SEPT members and result in a rearrangement from the predominantly organized filaments of the full length of SEPTs into smaller, lower-order assemblies, and less organized filamentous structures in non-ciliated cells.

Overall, these results may provide the first evidence that SEPT filament dynamics are affected by SEPT cleavage by 3CL proteases of coronaviruses including SARS-CoV-2. Specifically, 3CLpro cleaves SEPT members (SEPT2, 6, and 9) into two fragments (NT and CT), resulting in the alteration of the physical properties and functions of SEPT filaments in infected cells.

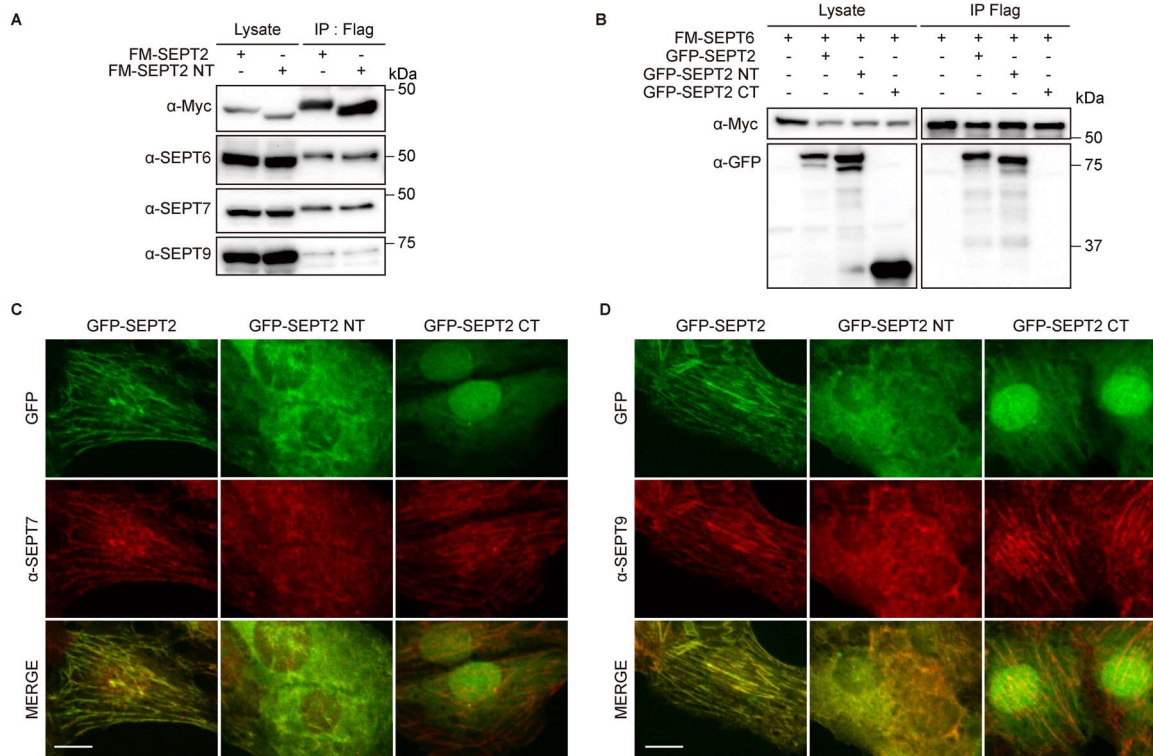


**Figure 25. The cleaved SEPT2 NT interferes with septin filaments by forming homo- and heteromeric complexes with SEPT members in non-ciliary hRPE1 cells.**

(A) Immunoblots of whole-cell lysates (left) or immunoprecipitates (right) from HEK293T cells expressing Flag-Myc-SEPT2 FL and NT. (B) Immunoblots of whole-cell lysates (left) or immunoprecipitates (right) from co-expressing Flag-Myc-SEPT6 and GFP-SEPT2 FL, NT, or CT. (C and D) Fluorescence microscopy for GFP-SEPT2 (FL, NT, and CT) in hTERT-RPE1 cells lentivirus infected with the indicated SEPT2 constructs. Immunostained with anti-SEPT7 (C, red) and anti-SEPT9 (D, red). Scale bar, 10 μm Crop image scale bar, 2 μm.

### 2.3.7. The cleaved SEPT2 NT and CT affect ciliogenesis.

Next, I have raised the question of what may happen to cilia if 3CL protease cleaved SEPTs into fragments. The functions of cytokinesis, cell polarity, and cell migration and the emerging functions of septins in ciliogenesis have also been studied. However, it remains unclear how septins contribute to ciliogenesis in the primary ciliated cells and influence ciliopathies most notably those caused by coronavirus infection since more evidence indicates that cilia morphology and function are more affected by emerging coronaviruses, MERS, and SARS-CoVs infections.

To answer this question, the formation of cilia was induced by serum starvation for 24 h with the hRPE-1 stable cells expressing GFP-tagged SEPT2 FL, NT, and CT (Figure 26A). Interestingly, unlike the colocalization of GFP-SEPT2 FL with acetylated microtubules in the cilium, neither GFP-SEPT2 NT nor CT appeared in the ciliary axoneme and GFP-SEPT2 CT seemed to be stuck in the basement of the ciliary root (i.e., centriole complex) (Figure 26B).

Using confocal microscopy, I were apparently able to detect the ciliary localization of two SEPT2 fragments in the cells stably expressing GFP-SEPT2 NT or CT, exhibiting little fluorescence in the ciliary axoneme. Further, GFP-SEPT2 CT was found to be trapped in the centriole complex, as shown by the anti-TTBK2 antibody labeling, a positive mother centriole marker (Figure 26C). These results suggested that the cleaved SEPTs might be mislocated into the subcellular locations of cilia structures.

Additionally, I found that significant defects in ciliogenesis were observed in cells expressing both SETP2 NT and CT showing a reduced number of ciliated cells (Figure 26D) and a short length of cilia (Figure 26E). Therefore, SEPT2 cleaved fragments by 3CLpro might affect ciliogenesis in the primary cilium during coronavirus infection.

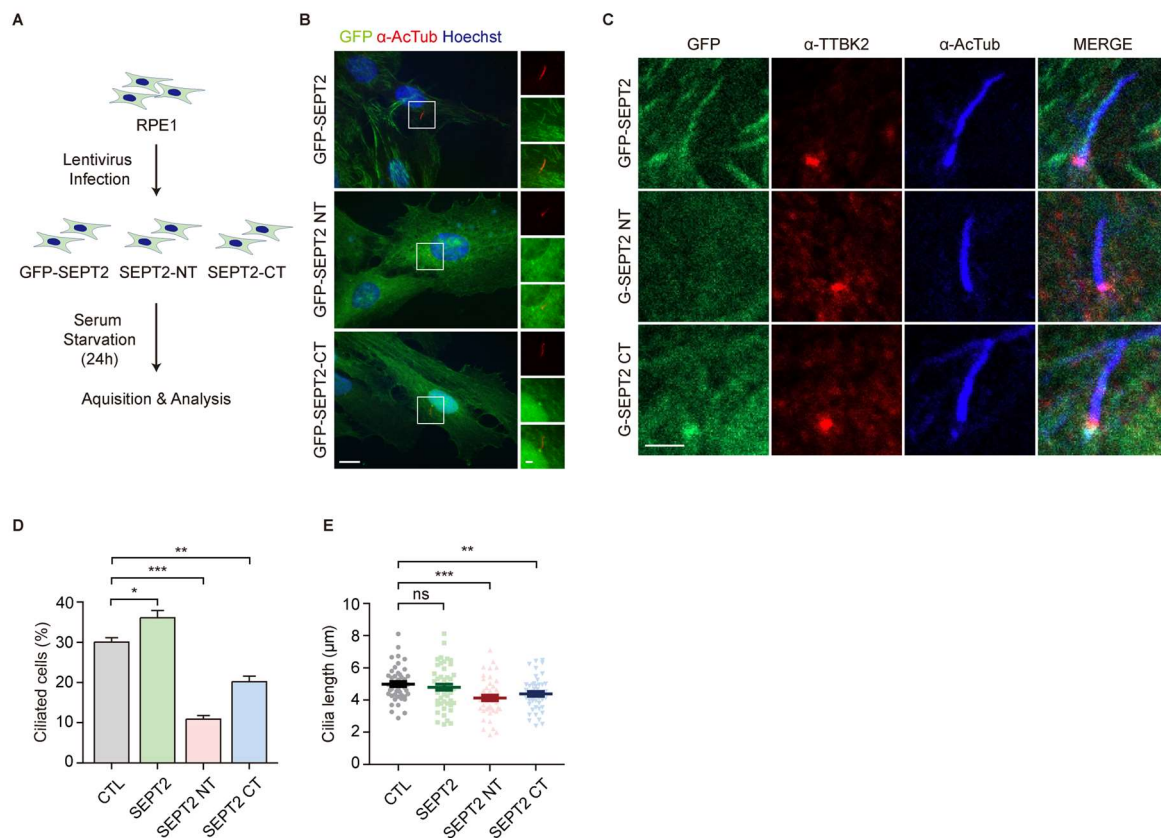


**Figure 26. The cleaved SEPT2 NT and CT affect ciliogenesis.**

(A) A schematic representation of the experimental design for the cilia assembly assay. hTERT-RPE1 cells were infected by indicated SEPT2 fragments. SEPT2 fragment stable cells followed by 24 h serum

starvation and immunostaining for indicated antibodies. **(B)** hTERT-RPE1 cells expressing GFP-SEPT2 fragments (FL, NT, and CT) were serum starved for 24 h and stained with acetylated  $\alpha$ -tubulin (red). Scale bar, 10  $\mu$ m. Crop image scale bar, 2  $\mu$ m. **(C)** hTERT-RPE1 cells expressing GFP-SEPT2 fragments (FL, NT, and CT) were serum starved for 24 h and stained with  $\alpha$ -TTBK2 (red) and acetylated  $\alpha$ -tubulin (blue). Scale bar, 2  $\mu$ m. **(D)** Quantification of the percentage of ciliated cells. At least 264 cells per sample were analyzed. **(E)** Quantification of the ciliary length. n=58 for each group. \*\*\*p < 0.001; \*\*p < 0.01; \*p < 0.05; ns, not significant. two-sample t-test.

### 2.3.8. Mislocated SEPT2 fragments disturb SEPTs translocation into cilia.

As one of the possible explanations for potential ciliary dysfunction and to understand how the cleaved fragments of SEPT2 and other cleaved SEPTs could cause this aberration in ciliogenesis, I investigated whether the cleaved SEPT2 fragments might affect the cellular localization and the proper function of other SEPT members in ciliated cells. Flag-Myc tagged-SEPT2 was expressed in pre-ciliated RPE1 cells stably expressing GFP-tagged SEPT2 FL, NT, or CT. Further, ciliogenesis was induced through serum starvation for 24 h. In line with my expectations, the cells expressing both GFP- and Flag-Myc SEPT2 FL presented well-colocalized filamentous distributions both in the cytosol and cilia (Figure 27A, top). However, the cells expressing GFP-SEPT2 fragments exhibited distinct colocalization patterns showing that FM-SEPT2 FL failed to translocate into the ciliary axoneme while the FM-SEPT2 FL and GFP-SEPT2 NT filament structures colocalized in the cytosol (Figure 27A, middle). This may be because the cytosolic localized SEPT2 NT binds to SEPT2 FL which ensures that these homomeric complexes are retained in the cytosol rather than in the cilia. The cells expressing GFP-SEPT2 CT entrapped in the centriole complex and cytosol showed no colocalization with FM-SEPT2 FL in the base of the ciliary root (Figure 27A, bottom). However, FM-SEPT2 FL was detected in the ciliary axonemes only when the expression level of FM-SEPT2 was higher than that of GFP-SEPT2 NT or CT, suggesting that abundant and unbound SEPT2 proteins might be translocated into their designated locations by escaping the interaction with the fragments. Therefore, I further examined other SEPT subgroup members as well. The cellular location of SEPT7 and SEPT9 was analyzed in cells expressing GFP-SEPT2 FL, NT, or CT. As expected, SEPT7 and SEPT9 showed identical subcellular distributions to those of SEPT2 (Figure 27B and C). Based on these results, it might be reasonable to conclude that cleaved SEPT2 fragments bind to other SEPT members in the cytosol or the ciliary basement and these complexes might obstruct the translocation of SEPT subgroup members to the correct subcellular location for proper function as septin filaments, and this would be the intended consequence of coronaviruses and 3CL proteases in infected ciliary cells.



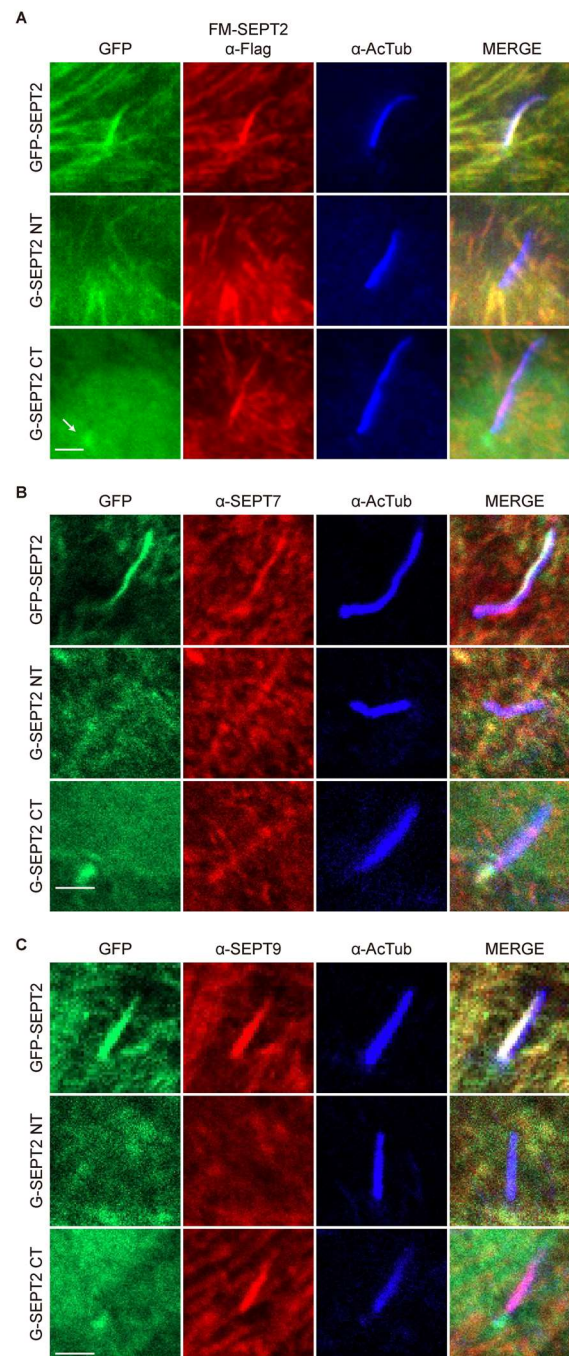


**Figure 27. Mislocated SEPT2 fragments disturb SEPTs translocation into cilia.**

(A) hTERT-RPE1 cells coexpressing FM-SEPT2 (FL, red) and GFP-SEPT2 fragments (FL, NT, and CT) were serum starved for 24 h and immunostained with acetylated  $\alpha$ -tubulin (blue). Arrow indicates CT at the M-centriole basal body. Scale bar, 2  $\mu$ m. (B and C) hTERT-RPE1 cells expressing GFP-SEPT2 fragments (FL, NT, and CT) were serum starved for 24 h and immunostained with acetylated  $\alpha$ -tubulin (blue) and SEPT7 (red, B) or SEPT9 (red, C). Scale bar, 2  $\mu$ m.

### **2.3.9. 3CLpro reduces ciliary septins and induces primary cilia defects.**

Then, I confirmed the SEPT2 cleavage in ciliary cells by 3CLpro expression. I introduced either 3CLpro into pre-ciliated NIH-3T3 cells and induced ciliogenesis (Figure 28A). As expected, the 3CLpro expression displayed a reduction in the intensity of SEPT2 in the ciliary axoneme (Figure 28B and C). This result indicated that the SEPT2 is a novel ciliary target protein of 3CLpro during coronavirus infection.

Finally, I measured the efficiency of ciliogenesis with Smo-GFP RPE cells, another cilia model cell by expressing SARS-CoV-2 3CLpro and found that the cells expressing 3CLpro showed a lower number of cilia cells (Figure 28D and E). NIH-3T3 cells expressing 3CLpro showed a decreased number of ciliated cells (Figure 28F-H). Furthermore, I confirmed the effect of 3CL protease on the ciliogenesis of MRC-5, the primary human lung fibroblast. As observed in RPE-1 and NIH-3T3 cells, MRC-5 cells expressing 3CL protease showed a decreased efficiency of ciliogenesis (Figure 28I-K), confirming that 3CL protease may induce ciliary defects in MRC-5. These results suggest that HCoV-OC43 and 3CL proteases cleaved cytosolic septins in pre-ciliated hRPE1 cells or NIH-3T3 cells and inhibited the translocation of SEPT2 and unidentified ciliary proteins into cilia axoneme, resulting in the ciliogenesis defect.

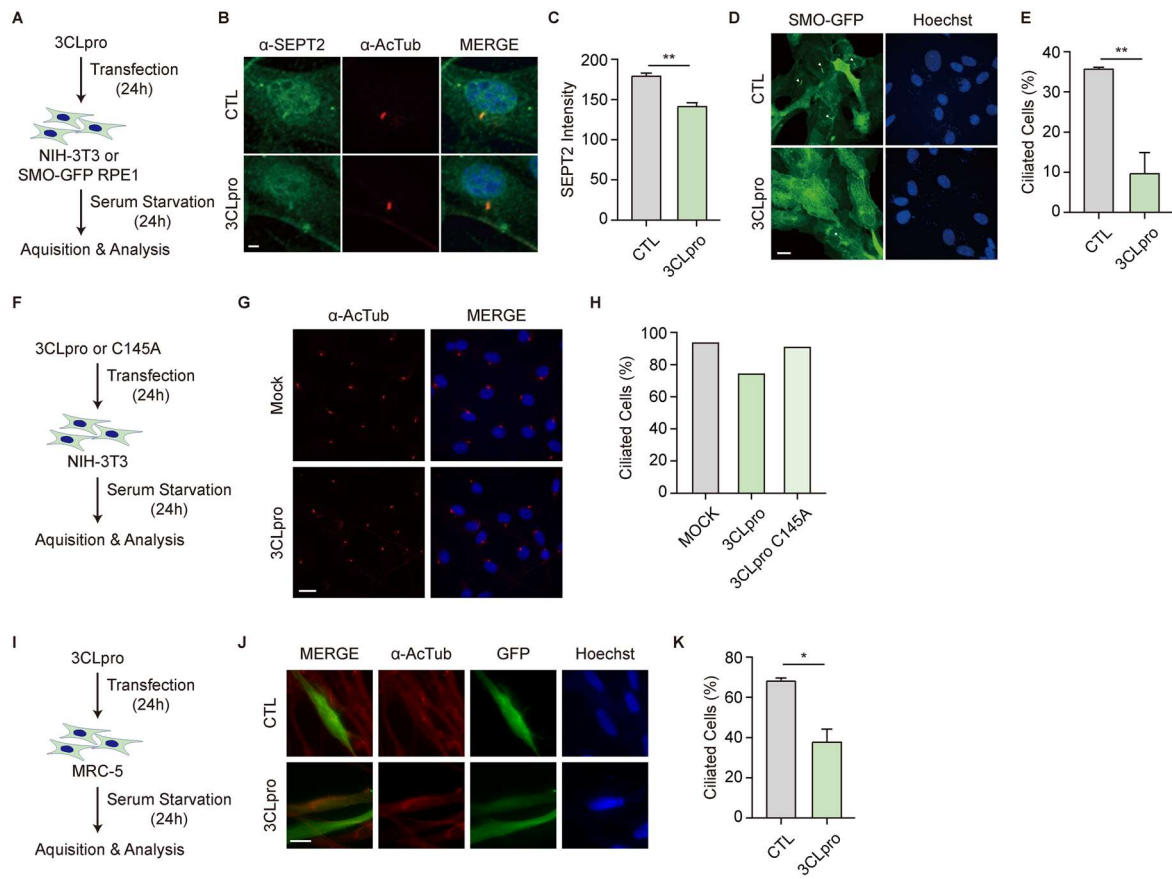


**Figure 28. 3CLpro reduces ciliary septins and induces primary cilia defects.**

(A) A schematic representation of the experimental design for the cilia assembly assay. hTERT-RPE1 or NIH-3T3 cells were transfected by 3CLpro, followed by 24 h serum starvation and immunostained for indicated antibodies. (B) NIH-3T3 cells were transfected with pcDNA3 or 3CLpro were serum-starved and immunostained for SEPT2 (green) and acetylated  $\alpha$ -tubulin (red). Scale bar, 2  $\mu$ m. (C) Quantification of SEPT2 intensity at the cilia axoneme.  $n = 88, 82$  for each group. (D) SMO-GFP-RPE1 cells transfected with pcDNA or 3CLpro were serum-starved and fluorescence images were acquired for SMO-GFP (cilia, green). Scale bar, 10  $\mu$ m. (E) Quantification of the percentage of ciliated cells. At least 130 cells per sample were analyzed. (F and I) A schematic representation of the experimental design for the cilia assembly assay. NIH-3T3 cells were transfected with 3CLpro or C145A mutant, followed by 24 h serum starvation and immunostaining for acetylated tubulin (F). MRC-5 cells were transfected with 3CLpro, followed by 24 h serum starvation and immunostaining for acetylated tubulin (I). (G and J) NIH-3T3 (G) and MRC-5 cells (J) were transfected with pcDNA (vector) or 3CLpro were serum-starved and immunostained for and acetylated  $\alpha$ -tubulin (Actub, red). GFP showed transfected cells (J). The nuclei were stained with Hoechst33342. Scale bar, 10  $\mu$ m. (H and K) Quantification of the percentage of ciliated cells. At least 40 NIH-3T3 cells (H) and 115 MRC-5 cells (K) per sample were analyzed. \*\* $p < 0.01$ ; \* $p < 0.05$ ; ns, not significant.



### 2.3.10. Coronavirus infection shows deciliation and SEPT2 reduction in cilia.

Next, I investigated the molecular mechanisms of ciliary dysfunctions, especially the effect of septin cleavage in ciliated cells by coronavirus infection and 3CLpro. To assess the impact of coronavirus infection on ciliogenesis, I validated two viral infection protocols, “Infection to ciliated cells” and “Infection to pre-ciliated cells” (Figure 29A and Figure 30A). First, for post-infection assay, ciliogenesis was first induced in hRPE1 cells by serum starvation for 24 h and infected with beta-HCoV-OC43 at an MOI of 20 for 24-48 h (Figure 29A).

I compared the percentage of ciliated cells as well as the length of the cilia by staining them with anti-acetylated tubulin. The infected cells were stained with anti-nucleocapsid (N) antibody to differentiate them from the uninfected cells (Figure 29B–D). I found that the number of ciliated cells decreased over the course of HCoV-OC43 infection of 24 to 48 h (Figure 29C), whereas the efficiency of ciliogenesis in non-infected ciliated cells slightly increased. I also observed that the length of primary cilia was shorter in OC43-infected cells than in uninfected cells (Figure 29D). These results suggested that ciliogenesis was affected by coronavirus infection in differentiated hRPE1 ciliary cells.

I previously showed that 3CL protease inhibitors, GC-376, and PF-00835231, blocked SEPT2 cleavage caused by 3CL protease in HEK293T cells (Figure 29D). Therefore, it is also important to examine whether 3CL protease inhibitors could prevent the ciliary defect in coronavirus-infected ciliary cells. The 3CL protease inhibitors (GC-376, PF-00835231) were applied 2 hpi to ciliated hRPE1 cells with OC43 at an MOI of 20. Intriguingly, I found that the efficiency of ciliogenesis was rescued with 3CL protease inhibitors in OC43 virus-infected cells as similar to that of non-infected cells (Figure 29E–G). The prevention of ciliogenesis defects might be due to the inhibition of SEPT2 cleavage by 3CLpro inhibitors, indicating that 3CL protease inhibitors may be effective in treating ciliary defects, one of the outcomes of COVID-19.

And interestingly, I found that the protein expression of SEPT2 in cilia was dramatically reduced in OC43 infected cells compared to that of non-infected cells (Figure 29H and I). This indicated that the viral infection caused the cleavage of an endogenous SEPT2 by 3CL protease and induced the misallocation of fragments, resulting in the ciliogenesis defect. Using structured illumination microscopy, I further visualized SEPT2 with an anti-SEPT2 antibody (green) in primary cilia and noticed that a type of SEPT complex interacted with microtubules to form bundles of striated puncta. Again, I detected a dramatic reduction in the intensity of SEPT2 in the ciliary axoneme as well as a shortening of primary cilia in infected cells (Figure 29J). NIH-3T3 cells were used to confirm the observation of the ciliogenesis defect in ciliated RPE1 cells in response to viral infection. I infected OC43 in ciliated NIH-3T3 cells and assessed the ciliogenesis. I found that OC43 infected a ciliated NIH-3T3 and showed a reduction in the number of ciliated cells and the length of cilia (Figure 29K–

N). From these results, I could confirm that coronavirus infection caused the deciliation. Further identified that this defect of ciliogenesis and deciliation might be induced by the SEPT cleavage by coronavirus 3CLpro. These results provide the first evidence that coronavirus could affect the ciliary SEPT filaments as well as cytosolic SEPT filaments that might cause the ciliary defect.

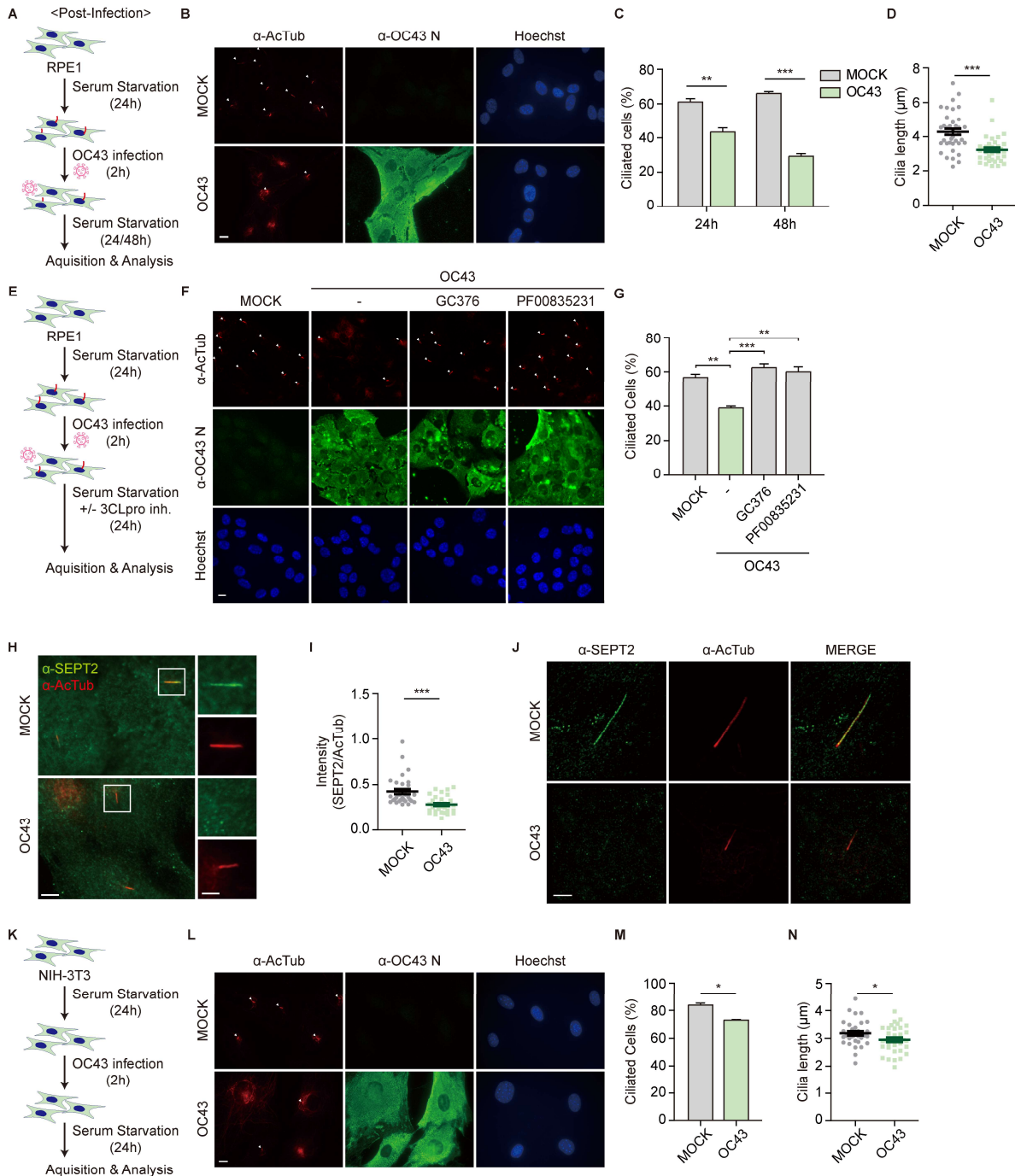


**Figure 29. Coronavirus infection shows deciliation and SEPT2 reduction in cilia.**

(A) A schematic representation of the experimental design for the cilia assembly assay. Pre-serum starved (ciliated) hTERT-RPE1 cells were infected by OC43, followed by 24 or 48 h serum starvation

and immunostained for indicated antibodies. **(B to D)** Fluorescence microscopy and quantification of ciliated hRPE1 cells infected with OC43 and immunostained for acetylated  $\alpha$ -tubulin (red) and OC43 N protein ( $\alpha$ -OC43 N, green). Scale bar, 10  $\mu$ m. Arrowheads indicate cilia **(B)**. Quantification of the percentage of ciliated cells. At least 214 cells per sample were analyzed **(C)**. Quantification of the ciliary length. cilia; n= 38 for each group **(D)**. **(E)** A schematic representation of the experimental design for the cilia assembly assay. Pre-serum-starved (ciliated) hTERT-RPE1 cells were infected by OC43, followed by 24 h serum starvation with 3CLpro inhibitors and immunostained for indicated antibodies. **(F and G)** Fluorescence microscopy and quantification of ciliated hRPE1 cells infected with OC43 and 3CLpro inhibitors (GC376, 50  $\mu$ M; PF00855231, 30  $\mu$ M) and immunostained for acetylated  $\alpha$ -tubulin (red) and OC43 N protein ( $\alpha$ -OC43 N, green). Scale bar, 10  $\mu$ m. Arrowheads indicate cilia **(F)**. Quantification of the percentage of ciliated cells. At least 301 cells per sample were analyzed **(G)**. **(H and I)** Fluorescence microscopy and the quantification of OC43 infected RPE1 cells were immunostained for acetylated  $\alpha$ -tubulin (red) and SEPT2 (green). Scale bar, 10  $\mu$ m, Crop image scale bar, 2  $\mu$ m **(H)**. Quantification data of SEPT2 intensity at the cilia axoneme. The fluorescence of SEPT2 was normalized by acetylated  $\alpha$ -tubulin. n=31 for each group **(I)**. **(J)** Super-resolution microscopy of the localization of SEPT2 along with the axoneme and the diminished localization by OC43 infection. SEPT2 (green), acetylated  $\alpha$ -tubulin (red). Scale bar, 2  $\mu$ m. **(K)** A schematic representation of the experimental design for the cilia assembly assay. Pre-serum-starved (ciliated) NIH-3T3 cells were infected by OC43, followed by 24 h serum starvation and immunostained for indicated antibodies. **(L)** Fluorescence microscopy and quantification of ciliated NIH-3T3 cells infected with OC43 and immunostained for acetylated  $\alpha$ -tubulin (red) and OC43 N protein ( $\alpha$ -OC43 N, green). Scale bar, 10  $\mu$ m. Arrowheads indicate cilia. **(M)** Quantification of the percentage of ciliated cells. At least 104 cells per sample were analyzed. **(N)** Quantification of the ciliary length (n=34 for each group). \*\*\*p < 0.001; \*\*p < 0.01; \*p < 0.05. two-sample t-test. The nuclei were stained with Hoechst33342.

### **2.3.11. Pre-ciliated cells show more severe ciliary defects, mediated by the cleaved SEPT2.**

Next, I examined how coronavirus infection affects the ciliogenesis of progenitor cells or pre-ciliated cells. To test this, I adopted a pre-infection approach involving the infection followed by ciliogenesis (Figure 30A). I first infected hRPE1 cells with HCoV-OC43 at an MOI of 30 for 24 h and then initiated ciliogenesis by removing serum for another 24 h. OC43 infected most pre-ciliated hRPE1 cells. Interestingly, I observed that most acetylated microtubules are enriched at the base of cilia protrusions in infected cells and a few were in cilia, however, most were located in cilia in uninfected cells (Figure 30B). Surprisingly, few ciliated cells were observed after infection (Figure 30C). Despite the low numbers of ciliated cells in infection conditions, I tried to measure the length of cilia that protruded from infected cells and found that the ciliary length in infected cells was slightly shorter than those of

uninfected cells (Figure 30D). I also measured the protein expression level of SEPT2 in cilia and found a significantly reduced amount even in the shorter cilia to OC43 infection, compared to that of non-infected cells (Figure 30E and F).

Furthermore, I investigated whether the treatment of 3CL protease inhibitor to the infected pre-ciliated cells would prevent the ciliary defect or ciliogenesis which might be due to SEPT2 cleavage. I observed that the infected cells with 3CLpro inhibitor GC-376 showed rescued ciliogenesis defects, shown with the infected cell without an inhibitor (Figure 30G and H), suggesting that 3CL protease inhibitors could be effective as therapeutic tools for ciliary defects which are caused by coronavirus infection.

Again, pre-infected NIH-3T3 cells were used to confirm the ciliogenesis defect in response to viral infection. I infected OC43 in pre-ciliated NIH-3T3 cells and assessed the difference in ciliogenesis. I noticed that OC43 infected most of pre-ciliated NIH-3T3 cells. After ciliogenesis induction, infected cells showed the ciliary defect with a reduction in the number of ciliated cells and the length of cilia (Figure 30I–L). I also noticed that the intensity of SEPT2 within a primary cilium was much lower in OC43 infected cells than in the uninfected cells (Figure 30M and N).

Based on these findings, it appears that coronavirus infection has a more pronounced effect on ciliogenesis in pre-ciliated cells than in ciliated cells. These observations could imply that ciliary dysfunction might occur in a wide range of cells in the nasal epithelium or other tissue which have ciliary precursor cells, and stem cells such as basal cells. Therefore, more attention is needed to the pre-ciliated cells and for the recovery of coronavirus-infected patients.

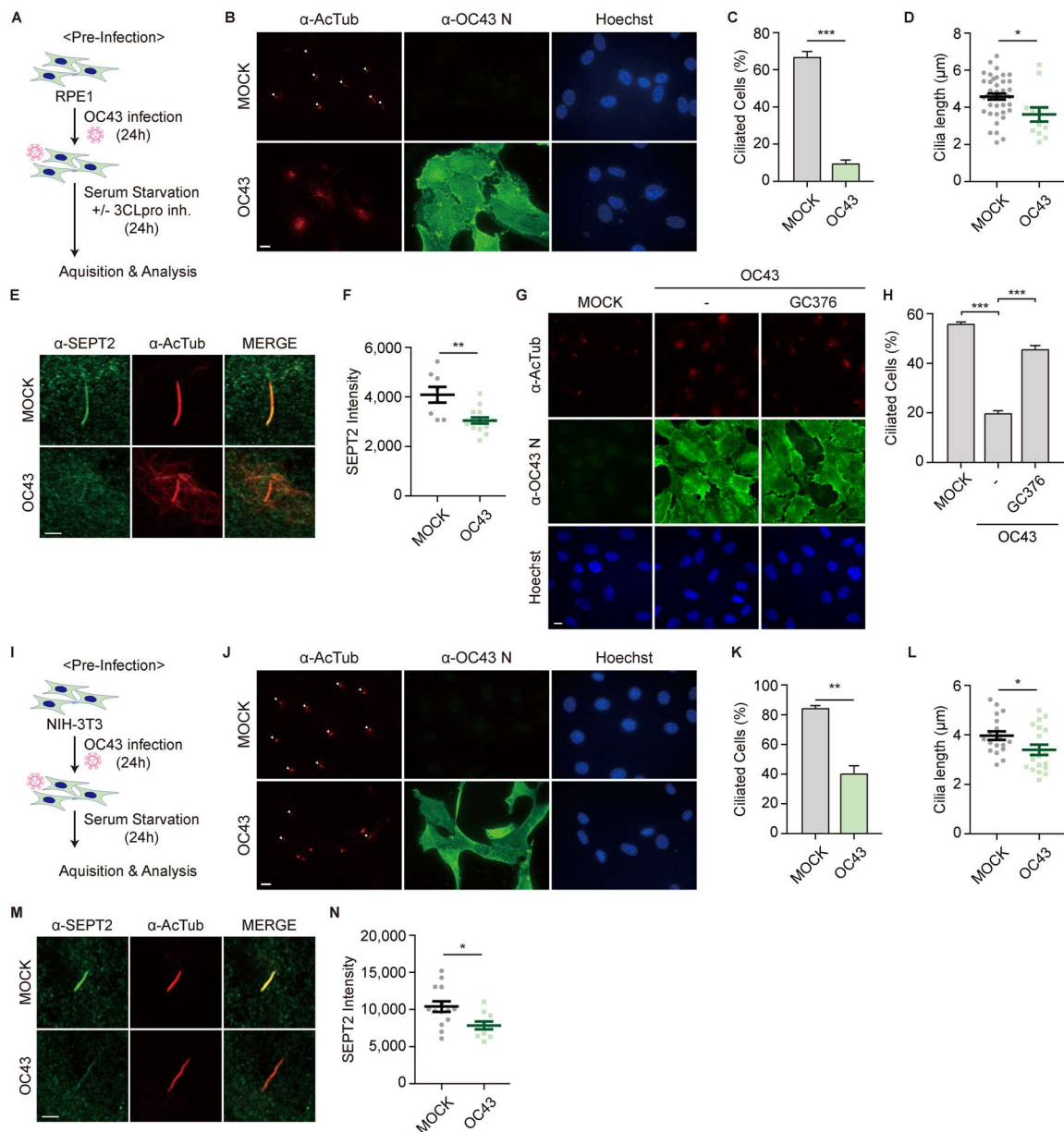


**Figure 30. Pre-ciliated cells show more severe ciliary defects, mediated by the cleaved SEPT2.**

(A) A schematic representation of the experimental design for the cilia assembly assay. hTERT-RPE1 cells were infected with OC43, followed by 24 h serum starvation and immunostaining for indicated antibodies. (B to D) hTERT-RPE1 cells infected with OC43 were serum-starved and immunostained for acetylated  $\alpha$ -tubulin (Actub, red) and OC43 N protein (OC43 N, green). Scale bar, 10  $\mu$ m. Arrowheads indicate cilia (B). Quantification of the percentage of ciliated cells. At least 152 cells per sample were analyzed (C). Quantification of the ciliary length. cilia; n= 43, 12 for each group (D). (E and F) hTERT-RPE1 cells infected by OC43 were immunostained for acetylated  $\alpha$ -tubulin (red) and SEPT2 (green). Scale bar, 2  $\mu$ m. Confocal microscopy shows that SEPT2 is localized to the cilia axoneme (E). Quantification of SEPT2 intensity at the cilia axoneme; n=9, 15 for each group (F). (G



and **H**) Fluorescence microscopy and quantification of ciliated hRPE1 cells infected with OC43 and 3CLpro inhibitors (GC376, 50  $\mu$ M) and immunostained for acetylated  $\alpha$ -tubulin (red) and OC43 N protein ( $\alpha$ -OC43 N, green). Scale bar, 10  $\mu$ m (**G**). Quantification of the percentage of ciliated cells. At least 266 cells per sample were analyzed (**H**). (**I**) A schematic representation of the experimental design for the cilia assembly assay. NIH-3T3 cells were infected with OC43, followed by 24 h serum starvation and immunostaining for indicated antibodies. (**J** to **L**) NIH-3T3 cells infected with OC43 were serum-starved and immunostained for acetylated  $\alpha$ -tubulin (red) and OC43 N protein (OC43 N, green). Scale bar, 10  $\mu$ m. Arrowheads indicate cilia (**J**). Quantification of the percentage of ciliated cells. At least 75 cells per sample were analyzed (**K**). Quantification of the ciliary length. cilia;  $n = 19$  for each group (**L**). (**M** and **N**) NIH-3T3 cells infected by OC43 were immunostained for acetylated  $\alpha$ -tubulin (red) and SEPT2 (Green). Scale bar, 2  $\mu$ m. Confocal microscopy showing that SEPT2 is localized to the cilia axoneme, which is disturbed by OC43 virus infection (**M**). Quantification of SEPT2 intensity at the cilia axoneme.  $n = 14, 10$  for each group (**N**). \*\*\* $p < 0.001$ ; \*\* $p < 0.01$ ; \* $p < 0.05$ . two-sample t-test. The nuclei were stained with Hoechst33342.

### 2.3.12. Coronavirus infection and 3CLpro affect SHH signaling in ciliary cells.

Finally, I investigated why 3CL proteases specifically target SEPT filaments and further whether the cleaved but not degradable septins could disrupt ciliary signaling during coronavirus infection. To answer these questions, I first examined whether coronavirus infection could affect SHH signaling in primary cilia which is the essential signaling for lots of processes in vertebrates (108).

NIH-3T3 cells were transfected with 8xGli firefly luciferase (109-111) and Renilla luciferase as an internal control reporter for 1 day, followed by serum starvation to induce ciliogenesis for 24 h. The ciliated cells were infected with HCoV-OC43 at an MOI of 5 and 10 for 2 h, then stimulated with SAG to stimulate SHH activation for an additional 24 h. To surprise, the transactivation of GLI transcription factors was completely abrogated in the coronavirus-infected NIH-3T3 cells, whereas control uninfected cells exhibited the full activation of GLI upon stimulation with SAG (smoothed agonist) (Figure 31A and B). Additionally, I compared the mRNA levels of GLI1 and PTCH1 in SAG and serum-starved NIH-3T3 cells with or without OC43 infection and observed a decrease in mRNA levels in infected cells (Figure 31C and D). Infection of NIH-3T3 was confirmed with the observation of increased OC43 titer and IFN beta mRNA levels (Figure 31E and F). To the best of my knowledge, these results provide the first evidence that coronaviruses could affect the SHH signaling, which is a major pathway in primary cilia.

I further confirmed that reduced SHH-GLI signaling was dependent on the enzymatic activity of 3CLpro (NSP5) because NIH 3T3 cells expressing NSP5 C145A did not affect SHH signaling (Figure 31G and H).

Finally, I measured the effect of SEPT cleaved fragments, NT and CT, on the transcriptional activity of GLI, and found that the NIH 3T3 cells expressing either NT or CT showed a reduced GLI activity (Figure 31I and J). These results might provide evidence of how coronavirus infection and 3CLpro can induce ciliary dysfunction, which might be due to the cleaved SEPTs and the disrupted ciliary SHH signaling during coronavirus infection.

Furthermore, these results are interesting and let us investigate whether 3CL protease inhibitors would prevent dysregulation of SHH signaling, caused by 3CL protease and cleaved SEPT fragments. The NIH-3T3 cells treated with GC-376 or PF-00835231 showed a restored GLI1 transcriptional activity (Figure 31K-M), suggesting that 3CL protease inhibitors prevent SHH signaling dysfunction by inhibiting 3CL protease activity in coronavirus-infected ciliary cells.



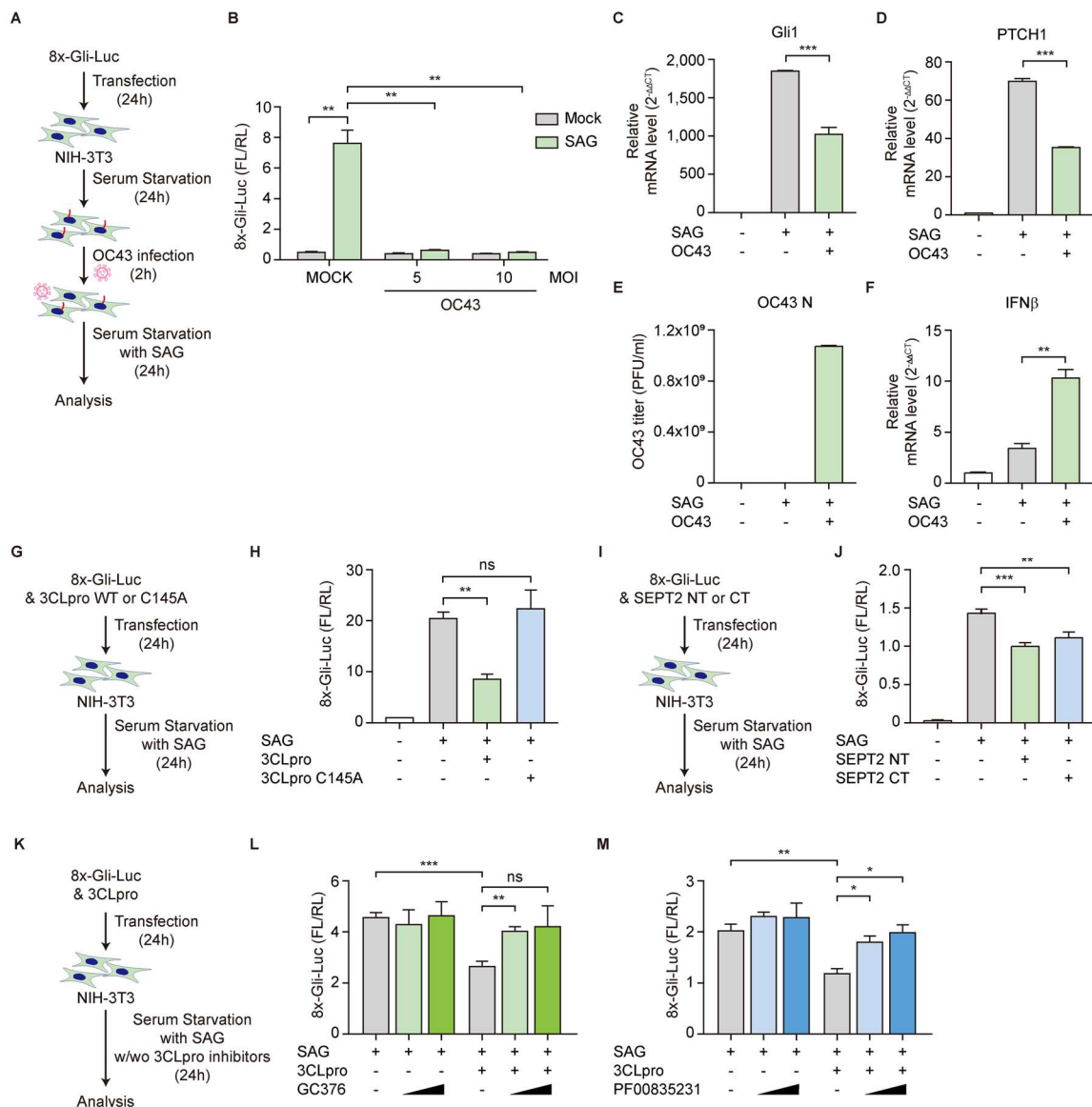


**Figure 31. Coronavirus infection and 3CLpro affect SHH signaling in ciliary cells.**

(A) A schematic representation of the experimental design for the Luciferase assay. Cilia induced NIH-3T3 cells were infected with OC43 at an MOI of 5 or 10 for 2 h before Smoothed agonist (SAG) (120 nM) treatment and serum starvation for 24 h. (B) Data are shown as the fold change of the ratio of luciferase reporter to Renilla activity. (C and D) The mRNA level of Gli1 (C) and PTCH1 (D) was determined by real-time PCR in NIH-3T3 cells, infected with OC43 at MOI 10 for 2 h before SAG (120 nM) treatment for 24 h. The transcript levels were normalized to the expression of GAPDH. (E) The titer of infectious HCoV-OC43 (PFU/ml) was determined by real-time PCR on infected NIH-3T3 cells. (F) The IFN beta mRNA level was determined by real-time PCR in NIH-3T3 cells, infected with OC43 at MOI 10 for 2 h before SAG (120 nM) treatment for 24 h. The transcript levels were normalized to the expression of GAPDH. (G) A schematic representation of the experimental design for the Luciferase assay. NIH-3T3 cells were transfected with SARS-CoV-2 NSP5 (3CL pro) or C145A mutant before

SAG (120 nM) treatment and serum starvation for 24 h. **(H)** Data are shown as the fold change of the ratio of luciferase reporter to Renilla activity. **(I)** Schematic representation of the experimental design for the Luciferase assay. NIH-3T3 cells were transfected with SEPT NT and SEPT2 CT fragments before SAG (120 nM) treatment and serum starvation for 24 h. **(J)** Data are shown as the fold change of the ratio of luciferase reporter to Renilla activity. **(K)** A schematic representation of the experimental design for the Luciferase assay with SAG (120 nM) treatment with 3CLpro inhibitors (GC376 and PF00835231). **(L)** Co-expressed with SARS-CoV-2 NSP5 (3CLpro) and treated GC376 (10, 50  $\mu$ M) with SAG (120 nM) for 24 h. **(M)** Co-expressed with SARS-CoV-2 3CLpro and treated PF00835231 (10, 30  $\mu$ M) with SAG (120 nM) for 24 h. Statistical significance was tested by two-sample t-test. \* $p < 0.05$ ; \*\* $p < 0.01$ ; \*\*\* $p < 0.001$ ; ns, not significant.

## 2.4. Discussion

These results describe a novel mechanism of how coronavirus infection induces ciliary defects (Figure 32). The 3CL protease of most human infectious coronaviruses cleave several septin host targets, thereby disrupting their function within ciliary microtubules and abolishing SHH pathways, which might serve an unknown benefit to coronaviruses and requires further study. Furthermore, 3CL protease inhibitors could be useful as therapeutics for treating ciliary defects caused by coronavirus infection.

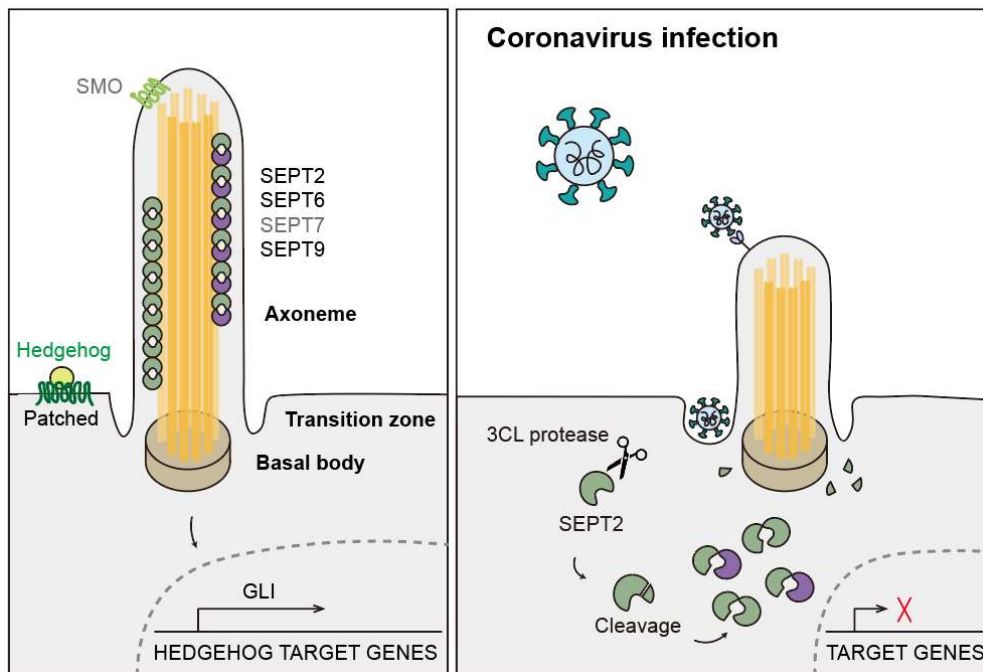


**Figure 32. Coronavirus 3CLprotease targets septins in cilia.**

The 3CL protease of most human infectious coronaviruses cleave several septin host targets, thereby disrupting their function within ciliary microtubules and abolishing SHH pathways.

I observed a more dramatic effect but with a variation in the efficiency of ciliogenesis in some infected cells (Figure 29 and Figure 30). Considering that the function of primary cilia depends on both their morphology and integrity, I measured the ciliary lengths of infected ciliated cells and found that they were shorter than those of uninfected ciliated cells. Furthermore, I found that Gli activity was significantly impaired in OC43-infected cells (Figure 31). Thus, coronavirus infection could eventually cause a ciliary defect in infected cells.

Primary cilia are microtubule-based structures. At their core is the microtubule-based axoneme, which supports cilia stability and acts as a scaffold for cargo transport. Microtubule stability and functions are

regulated by various factors including microtubule-binding proteins. Therefore, cleavage modification of microtubule-binding proteins by virus infection might affect ciliary stability and function. Septins are associated with subsets of microtubules in the cilia axoneme. Recent studies have reported the role of septins in regulating cilia stability and SHH signaling.

My data represented that SEPT2 fragments (NT and CT, cleaved by 3CL protease) were not located in cilia nor activated SHH signaling. I found NT fragments of SEPT2 in the cytosol rather than the ciliary axoneme, which may interfere with the translocation of other septins (uncleaved SEPT2, -7, and -9) as well as other ciliary maintenance and signaling proteins, including SHH pathway proteins, which requires further study.

The intraflagellar transport family of proteins and other ciliary proteins are transported from the base of the cilium to the tip. The SEPT2 CT fragment was found to be localized at the cilia basal body (Figure 26). Therefore, I hypothesized that SEPT2 CT may interfere with the transport of ciliary proteins or other cargoes, resulting in an SHH signaling reduction. Moreover, due to impaired microtubule stability, the function and translocation of ciliary proteins may be compromised.

Several SEPTs were found to be cleaved by 3CL proteases and coronaviruses, resulting in ciliary defects and the disruption of SHH signaling in infected cells. For a better understanding of how coronavirus 3CL protease might affect SHH signaling in ciliated cells, I examined whether 3CL protease could target other proteins in SHH signaling pathway. Using NetCorona 1.0, I were able to predict that several essential components are cleaved by 3Cl protease, including PTCH1, GLI2, GLI3, KIF7, and GSK3b (Figure 33). The SHH signaling pathway would be defective if one or more of the proteins in this pathway are cleaved by 3CL proteases in infected cells. The study of these potential targets may provide insight into additional molecular mechanisms associated with virus-induced ciliary dysfunction and compromised SHH signaling.

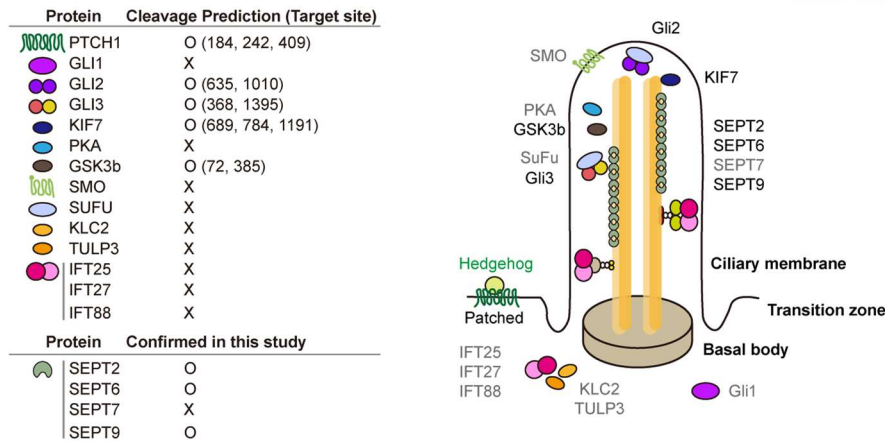


**Figure 33. Prediction of cleavage sites of some SHH signaling molecules.**

Values lower than the threshold (0.5) are not predicted as potential cleavage target sites. Numbers indicate the target sites of human SHH signaling proteins given by the prediction program.

SARS-CoV-2 infection is primarily transmitted through ciliated cells that express high levels of ACE2 receptors. Therefore, it is essential to understand how SARS-CoV-2 interacts with ciliated cells. Additionally, it may help us to understand how the virus causes disease and how to prevent it.

There has been recent research exploring the effects of viral infection on cilia loss and potential implications for viral replication and pathogenesis.

He et al. suggested that Coronavirus may disrupt the formation and function of cilia by targeting critical genes of ciliary cells. They found that infection with SARS-CoV-2 reduced the mRNA levels of FOXJ1 and RFX3, which are responsible for ciliogenesis. This causes the dedifferentiation of multiciliated cells, resulting in the loss of the ciliated layer and impaired mucociliary elimination. Thus, SARS-CoV-2 infection makes the respiratory system vulnerable to viral infection (75, 112).

Another study found that SARS-CoV-2 ORF10 can interfere with cilia biogenesis and maintenance by targeting IFT46, which is essential for normal ciliary function. They showed that SARS-CoV-2 ORF10 interacts with ZYG11B, increasing the E3 ligase activity of the CUL2ZYG11B complex. This enhanced activity results in the degradation of IFT46 through ubiquitination and subsequent proteasomal degradation (83).

Therefore, Coronaviruses can interact with the cilia and disrupt their function, leading to cilia loss. This in turn can alter the physiology of the cell, making it more susceptible to viral infection and potentially enhancing viral replication. Additionally, cilia loss can also lead to changes in the cell environment, allowing the virus to spread more readily and cause disease.

A better understanding of the impact of cilia loss and ciliated cell death on virus replication and pathogenesis could provide key insights into better ways to treat and prevent respiratory illnesses caused by coronaviruses. Despite extensive research on coronaviruses and cilia, further study is needed to determine the detailed mechanisms underlying cilia loss and cell death, as well as the potential impact of impaired cilia on viral replication and pathogenesis in ciliated cells.

## References

1. M. Overholtzer *et al.*, A nonapoptotic cell death process, entosis, that occurs by cell-in-cell invasion. *Cell* **131**, 966-979 (2007).
2. J. Durgan *et al.*, Mitosis can drive cell cannibalism through entosis. *Elife* **6**, (2017).
3. J. C. Hamann *et al.*, Entosis Is Induced by Glucose Starvation. *Cell Rep* **20**, 201-210 (2017).
4. M. Krajcovic *et al.*, A non-genetic route to aneuploidy in human cancers. *Nat Cell Biol* **13**, 324-330 (2011).
5. H. L. Mackay *et al.*, Genomic instability in mutant p53 cancer cells upon entotic engulfment. *Nat Commun* **9**, 3070 (2018).
6. Y. Li, X. Sun, S. K. Dey, Entosis allows timely elimination of the luminal epithelial barrier for embryo implantation. *Cell Rep* **11**, 358-365 (2015).
7. Y. Lee *et al.*, Entosis Controls a Developmental Cell Clearance in *C. elegans*. *Cell Rep* **26**, 3212-3220 e3214 (2019).
8. S. Krishna, M. Overholtzer, Mechanisms and consequences of entosis. *Cell Mol Life Sci* **73**, 2379-2386 (2016).
9. Q. Sun, E. S. Cibas, H. Huang, L. Hodgson, M. Overholtzer, Induction of entosis by epithelial cadherin expression. *Cell Res* **24**, 1288-1298 (2014).
10. W. Ren, W. Zhao, L. Cao, J. Huang, Involvement of the Actin Machinery in Programmed Cell Death. *Front Cell Dev Biol* **8**, 634849 (2020).
11. M. Wang *et al.*, Mechanical Ring Interfaces between Adherens Junction and Contractile Actomyosin to Coordinate Entotic Cell-in-Cell Formation. *Cell Rep* **32**, 108071 (2020).
12. O. Florey, S. E. Kim, C. P. Sandoval, C. M. Haynes, M. Overholtzer, Autophagy machinery mediates macroendocytic processing and entotic cell death by targeting single membranes. *Nat Cell Biol* **13**, 1335-1343 (2011).
13. Q. Sun *et al.*, Competition between human cells by entosis. *Cell Res* **24**, 1299-1310 (2014).
14. V. Purvanov, M. Holst, J. Khan, C. Baarlink, R. Grosse, G-protein-coupled receptor signaling and polarized actin dynamics drive cell-in-cell invasion. *Elife* **3**, (2014).
15. D. E. Clapham, Calcium signaling. *Cell* **131**, 1047-1058 (2007).
16. Y. F. Chen, Y. T. Chen, W. T. Chiu, M. R. Shen, Remodeling of calcium signaling in tumor progression. *J Biomed Sci* **20**, 23 (2013).
17. R. Bagur, G. Hajnoczky, Intracellular Ca<sup>2+</sup> Sensing: Its Role in Calcium Homeostasis and Signaling. *Mol Cell* **66**, 780-788 (2017).
18. M. J. Berridge, M. D. Bootman, H. L. Roderick, Calcium signalling: dynamics, homeostasis and remodelling. *Nature Reviews Molecular Cell Biology* **4**, 517-529 (2003).



19. M. Prakriya *et al.*, Orai1 is an essential pore subunit of the CRAC channel. *Nature* **443**, 230-233 (2006).
20. S. Feske *et al.*, A mutation in Orai1 causes immune deficiency by abrogating CRAC channel function. *Nature* **441**, 179-185 (2006).
21. J. Roos *et al.*, STIM1, an essential and conserved component of store-operated Ca<sup>2+</sup> channel function. *Journal of Cell Biology* **169**, 435-445 (2005).
22. S. Yang, J. J. Zhang, X. Y. Huang, Orai1 and STIM1 are critical for breast tumor cell migration and metastasis. *Cancer Cell* **15**, 124-134 (2009).
23. M. Prakriya, R. S. Lewis, Store-Operated Calcium Channels. *Physiol Rev* **95**, 1383-1436 (2015).
24. P. G. Hogan, The STIM1–ORAI1 microdomain. *Cell Calcium* **58**, 357-367 (2015).
25. R. M. La Rovere, G. Roest, G. Bultynck, J. B. Parys, Intracellular Ca<sup>2+</sup> signaling and Ca<sup>2+</sup> microdomains in the control of cell survival, apoptosis and autophagy. *Cell Calcium* **60**, 74-87 (2016).
26. S. Mostowy, P. Cossart, Septins: the fourth component of the cytoskeleton. *Nat Rev Mol Cell Biol* **13**, 183-194 (2012).
27. A. A. Bridges, M. S. Jentsch, P. W. Oakes, P. Occhipinti, A. S. Gladfelter, Micron-scale plasma membrane curvature is recognized by the septin cytoskeleton. *J Cell Biol* **213**, 23-32 (2016).
28. D. Lobato-Márquez, S. Mostowy, Septins recognize micron-scale membrane curvature. *Journal of Cell Biology* **213**, 5-6 (2016).
29. S. Sharma *et al.*, An siRNA screen for NFAT activation identifies septins as coordinators of store-operated Ca<sup>2+</sup> entry. *Nature* **499**, 238-242 (2013).
30. M. I. Lioudyno *et al.*, Orai1 and STIM1 move to the immunological synapse and are up-regulated during T cell activation. *Proceedings of the National Academy of Sciences* **105**, 2011-2016 (2008).
31. K. Aoki *et al.*, STIM-Orai1 signaling regulates fluidity of cytoplasm during membrane blebbing. *Nat Commun* **12**, 480 (2021).
32. F. C. Tsai *et al.*, A polarized Ca<sup>2+</sup>, diacylglycerol and STIM1 signalling system regulates directed cell migration. *Nat Cell Biol* **16**, 133-144 (2014).
33. A. M. Lopez-Guerrero *et al.*, RAC1-Dependent ORAI1 Translocation to the Leading Edge Supports Lamellipodia Formation and Directional Persistence. *Sci Rep* **10**, 6580 (2020).
34. Y. T. Chen *et al.*, The ER Ca<sup>2+</sup> sensor STIM1 regulates actomyosin contractility of migratory cells. *J Cell Sci* **126**, 1260-1267 (2013).
35. T.-W. Chen *et al.*, Ultrasensitive fluorescent proteins for imaging neuronal activity. *Nature* **499**, 295-300 (2013).

36. A. M. Sadaghiani *et al.*, Identification of Orai1 channel inhibitors by using minimal functional domains to screen small molecule microarrays. *Chem Biol* **21**, 1278-1292 (2014).
37. J. J. Lopez *et al.*, Molecular modulators of store-operated calcium entry. *Biochim Biophys Acta* **1863**, 2037-2043 (2016).
38. Z. B. Katz, C. Zhang, A. Quintana, B. F. Lillemeier, P. G. Hogan, Septins organize endoplasmic reticulum-plasma membrane junctions for STIM1-ORAI1 calcium signalling. *Sci Rep* **9**, 10839 (2019).
39. Q. Hu, W. J. Nelson, E. T. Spiliotis, Forchlorfenuron alters mammalian septin assembly, organization, and dynamics. *J Biol Chem* **283**, 29563-29571 (2008).
40. V. K. Sidhaye, E. Chau, P. N. Breyse, L. S. King, Septin-2 mediates airway epithelial barrier function in physiologic and pathologic conditions. *Am J Respir Cell Mol Biol* **45**, 120-126 (2011).
41. N. F. Valadares, H. d' Muniz Pereira, A. P. Ulian Araujo, R. C. Garratt, Septin structure and filament assembly. *Biophys Rev* **9**, 481-500 (2017).
42. R. K. Motiani, I. F. Abdullaev, M. Trebak, A novel native store-operated calcium channel encoded by Orai3: selective requirement of Orai3 versus Orai1 in estrogen receptor-positive versus estrogen receptor-negative breast cancer cells. *J Biol Chem* **285**, 19173-19183 (2010).
43. H. L. Ong *et al.*, Dynamic Assembly of TRPC1-STIM1-Orai1 Ternary Complex Is Involved in Store-operated Calcium Influx. *Journal of Biological Chemistry* **282**, 9105-9116 (2007).
44. Y. Liao *et al.*, Orai proteins interact with TRPC channels and confer responsiveness to store depletion. *Proceedings of the National Academy of Sciences* **104**, 4682-4687 (2007).
45. Y. Liu *et al.*, Crystal Structure of Calmodulin Binding Domain of Orai1 in Complex with Ca<sup>2+</sup>•Calmodulin Displays a Unique Binding Mode. *Journal of Biological Chemistry* **287**, 43030-43041 (2012).
46. A. Jha *et al.*, The STIM1 CTID domain determines access of SARAF to SOAR to regulate Orai1 channel function. *Journal of Cell Biology* **202**, 71-79 (2013).
47. L. Albarran *et al.*, EFHB is a Novel Cytosolic Ca<sup>2+</sup> Sensor That Modulates STIM1-SARAF Interaction. *Cellular Physiology and Biochemistry* **51**, 1164-1178 (2018).
48. A. M. Lopez-Guerrero *et al.*, Regulation of membrane ruffling by polarized STIM1 and ORAI1 in cortactin-rich domains. *Scientific Reports* **7**, (2017).
49. S. Pece, J. S. Gutkind, Signaling from E-cadherins to the MAPK Pathway by the Recruitment and Activation of Epidermal Growth Factor Receptors upon Cell-Cell Contact Formation. *Journal of Biological Chemistry* **275**, 41227-41233 (2000).
50. R. R. Rayavarapu *et al.*, The Role of Multicellular Aggregation in the Survival of ErbB2-positive Breast Cancer Cells during Extracellular Matrix Detachment. *Journal of Biological Chemistry* **290**, 8722-8733 (2015).

51. A. Sharma, R. C. Elble, From Orai to E-Cadherin: Subversion of Calcium Trafficking in Cancer to Drive Proliferation, Anoikis-Resistance, and Metastasis. *Biomedicines* **8**, 169 (2020).
52. M. Vandenberghe *et al.*, ORAI1 calcium channel orchestrates skin homeostasis. *Proc Natl Acad Sci U S A* **110**, E4839-4848 (2013).
53. S. M. Emrich *et al.*, Omnitemporal choreographies of all five STIM/Orai and IP<sub>3</sub>Rs underlie the complexity of mammalian Ca<sup>2+</sup> signaling. *Cell Reports* **34**, 108760 (2021).
54. J. Sun *et al.*, STIM1- and Orai1-mediated Ca<sup>2+</sup> oscillation orchestrates invadopodium formation and melanoma invasion. *J Cell Biol* **207**, 535-548 (2014).
55. R. E. Yoast *et al.*, The native ORAI channel trio underlies the diversity of Ca<sup>2+</sup> signaling events. *Nature Communications* **11**, (2020).
56. M. J. Berridge, The Inositol Trisphosphate/Calcium Signaling Pathway in Health and Disease. *Physiological Reviews* **96**, 1261-1296 (2016).
57. A. Politi, L. D. Gaspers, A. P. Thomas, T. Höfer, Models of IP<sub>3</sub> and Ca<sup>2+</sup> Oscillations: Frequency Encoding and Identification of Underlying Feedbacks. *Biophysical Journal* **90**, 3120-3133 (2006).
58. C. Fewtrell, Ca<sup>2+</sup> Oscillations in Non-Excitable Cells. *Annual Review of Physiology* **55**, 427-454 (1993).
59. T. Singhal, A Review of Coronavirus Disease-2019 (COVID-19). *The Indian Journal of Pediatrics* **87**, 281-286 (2020).
60. B. Hu, H. Guo, P. Zhou, Z.-L. Shi, Characteristics of SARS-CoV-2 and COVID-19. *Nature Reviews Microbiology* **19**, 141-154 (2021).
61. H. Yang, Z. Rao, Structural biology of SARS-CoV-2 and implications for therapeutic development. *Nat Rev Microbiol* **19**, 685-700 (2021).
62. N. Kirtipal, S. Bharadwaj, S. G. Kang, From SARS to SARS-CoV-2, insights on structure, pathogenicity and immunity aspects of pandemic human coronaviruses. *Infect Genet Evol* **85**, 104502 (2020).
63. T. Klemm *et al.*, Mechanism and inhibition of the papain-like protease, PLpro, of SARS-CoV-2. *EMBO J* **39**, e106275 (2020).
64. W. Li *et al.*, SARS-CoV-2 Nsp5 Activates NF-kappaB Pathway by Upregulating SUMOylation of MAVS. *Front Immunol* **12**, 750969 (2021).
65. B. Xia, X. Kang, Activation and maturation of SARS-CoV main protease. *Protein & Cell* **2**, 282-290 (2011).
66. Y. Kasuga, B. Zhu, K. J. Jang, J. S. Yoo, Innate immune sensing of coronavirus and viral evasion strategies. *Exp Mol Med* **53**, 723-736 (2021).
67. T. Pillaiyar, M. Manickam, V. Namasivayam, Y. Hayashi, S.-H. Jung, An Overview of Severe Acute Respiratory Syndrome–Coronavirus (SARS-CoV) 3CL Protease Inhibitors:

- Peptidomimetics and Small Molecule Chemotherapy. *Journal of Medicinal Chemistry* **59**, 6595-6628 (2016).
68. D. R. Owen *et al.*, An oral SARS-CoV-2 Mpro inhibitor clinical candidate for the treatment of COVID-19. *Science* **374**, 1586-1593 (2021).
  69. P. Satir, S. T. Christensen, Overview of structure and function of mammalian cilia. *Annu Rev Physiol* **69**, 377-400 (2007).
  70. O. Palander, M. El-Zeiry, W. S. Trimble, Uncovering the Roles of Septins in Cilia. *Front Cell Dev Biol* **5**, 36 (2017).
  71. S. C. Goetz, K. V. Anderson, The primary cilium: a signalling centre during vertebrate development. *Nat Rev Genet* **11**, 331-344 (2010).
  72. L. E. Kuek, R. J. Lee, First contact: the role of respiratory cilia in host-pathogen interactions in the airways. *American Journal of Physiology-Lung Cellular and Molecular Physiology* **319**, L603-L619 (2020).
  73. M. Saade *et al.*, Multimerization of Zika Virus-NS5 Causes Ciliopathy and Forces Premature Neurogenesis. *Cell Stem Cell* **27**, 920-936.e928 (2020).
  74. M. E. Johansson, G. C. Hansson, Immunological aspects of intestinal mucus and mucins. *Nat Rev Immunol* **16**, 639-649 (2016).
  75. R. Robinot *et al.*, SARS-CoV-2 infection induces the dedifferentiation of multiciliated cells and impairs mucociliary clearance. *Nat Commun* **12**, 4354 (2021).
  76. N. Zamorano Cuervo, N. Grandvaux, ACE2: Evidence of role as entry receptor for SARS-CoV-2 and implications in comorbidities. *Elife* **9**, (2020).
  77. H. Chen *et al.*, SARS-CoV-2 activates lung epithelial cell proinflammatory signaling and leads to immune dysregulation in COVID-19 patients. *EBioMedicine* **70**, 103500 (2021).
  78. X. Huang *et al.*, Human Coronavirus HKU1 Spike Protein Uses O-Acetylated Sialic Acid as an Attachment Receptor Determinant and Employs Hemagglutinin-Esterase Protein as a Receptor-Destroying Enzyme. *J Virol* **89**, 7202-7213 (2015).
  79. W. Li, M. Li, G. Ou, COVID-19, cilia, and smell. *The FEBS Journal* **287**, 3672-3676 (2020).
  80. M. A. Chilvers *et al.*, The effects of coronavirus on human nasal ciliated respiratory epithelium. *European Respiratory Journal* **18**, 965-970 (2001).
  81. M. Letko, A. Marzi, V. Munster, Functional assessment of cell entry and receptor usage for SARS-CoV-2 and other lineage B betacoronaviruses. *Nature Microbiology* **5**, 562-569 (2020).
  82. B. A. Afzelius, Ultrastructure of human nasal epithelium during an episode of coronavirus infection. *Virchows Archiv* **424**, 295-300 (1994).
  83. L. Wang *et al.*, SARS-CoV-2 ORF10 impairs cilia by enhancing CUL2ZYG11B activity. *Journal of Cell Biology* **221**, (2022).
  84. D. Kim *et al.*, The Architecture of SARS-CoV-2 Transcriptome. *Cell* **181**, 914-921.e910 (2020).

85. M. D. Parker *et al.*, Subgenomic RNA identification in SARS-CoV-2 genomic sequencing data. *Genome Research* **31**, 645-658 (2021).
86. D. A. Fletcher, R. D. Mullins, Cell mechanics and the cytoskeleton. *Nature* **463**, 485-492 (2010).
87. Z. Wen, Y. Zhang, Z. Lin, K. Shi, Y. Jiu, Cytoskeleton-a crucial key in host cell for coronavirus infection. *J Mol Cell Biol* **12**, 968-979 (2020).
88. J. E. Jones, V. Le Sage, S. S. Lakdawala, Viral and host heterogeneity and their effects on the viral life cycle. *Nat Rev Microbiol* **19**, 272-282 (2021).
89. X. Wang *et al.*, The septin complex links the catenin complex to the actin cytoskeleton for establishing epithelial cell polarity. *J Mol Cell Biol* **13**, 395-408 (2021).
90. G. Russo, M. Krauss, Septin Remodeling During Mammalian Cytokinesis. *Front Cell Dev Biol* **9**, 768309 (2021).
91. L. Dolat, Q. Hu, E. T. Spiliotis, Septin functions in organ system physiology and pathology. *Biol Chem* **395**, 123-141 (2014).
92. H. Van Ngo, S. Mostowy, Role of septins in microbial infection. *J Cell Sci* **132**, (2019).
93. F. Caudron, Y. Barral, Septins and the lateral compartmentalization of eukaryotic membranes. *Dev Cell* **16**, 493-506 (2009).
94. I. A. Cavini *et al.*, The Structural Biology of Septins and Their Filaments: An Update. *Front Cell Dev Biol* **9**, 765085 (2021).
95. N. F. Valadares, H. D' Muniz Pereira, A. P. Ulian Araujo, R. C. Garratt, Septin structure and filament assembly. *Biophysical Reviews* **9**, 481-500 (2017).
96. R. Ghossoub *et al.*, Septins 2, 7 and 9 and MAP4 colocalize along the axoneme in the primary cilium and control ciliary length. *J Cell Sci* **126**, 2583-2594 (2013).
97. T. Kanamaru, A. Neuner, B. Kurtulmus, G. Pereira, Balancing the length of the distal tip by septins is key for stability and signalling function of primary cilia. *EMBO J* **41**, e108843 (2022).
98. H. Li *et al.*, Zika Virus Protease Cleavage of Host Protein Septin-2 Mediates Mitotic Defects in Neural Progenitors. *Neuron* **101**, 1089-1098 e1084 (2019).
99. S. Zhao, J. Gao, L. Zhu, Q. Yang, Transmissible gastroenteritis virus and porcine epidemic diarrhoea virus infection induces dramatic changes in the tight junctions and microfilaments of polarized IPEC-J2 cells. *Virus Research* **192**, 34-45 (2014).
100. K. Biswas, J. Das Sarma, Effect of Microtubule Disruption on Neuronal Spread and Replication of Demyelinating and Nondemyelinating Strains of Mouse Hepatitis Virus *In Vitro*. *Journal of Virology* **88**, 3043-3047 (2014).
101. F. Reggiori, C. A. M. De Haan, M. Molinari, Unconventional Use of LC3 by Coronaviruses through the Alleged Subversion of the ERAD Tuning Pathway. *Viruses* **3**, 1610-1623 (2011).
102. H. J. Maier *et al.*, Visualizing the autophagy pathway in avian cells and its application to studying infectious bronchitis virus. *Autophagy* **9**, 496-509 (2013).

103. M.-F. Hsu *et al.*, Mechanism of the Maturation Process of SARS-CoV 3CL Protease. *Journal of Biological Chemistry* **280**, 31257-31266 (2005).
104. K. Fan *et al.*, Biosynthesis, Purification, and Substrate Specificity of Severe Acute Respiratory Syndrome Coronavirus 3C-like Proteinase. *Journal of Biological Chemistry* **279**, 1637-1642 (2004).
105. H. Wang *et al.*, Comprehensive Insights into the Catalytic Mechanism of Middle East Respiratory Syndrome 3C-Like Protease and Severe Acute Respiratory Syndrome 3C-Like Protease. *ACS Catalysis* **10**, 5871-5890 (2020).
106. L. Kiemer, O. Lund, S. Brunak, N. Blom, *BMC Bioinformatics* **5**, 72 (2004).
107. M. Sirajuddin, M. Farkasovsky, E. Zent, A. Wittinghofer, GTP-induced conformational changes in septins and implications for function. *Proceedings of the National Academy of Sciences* **106**, 16592-16597 (2009).
108. F. Bangs, K. V. Anderson, Primary Cilia and Mammalian Hedgehog Signaling. *Cold Spring Harb Perspect Biol* **9**, (2017).
109. L. Antonucci *et al.*, Mitogen-activated kinase kinase kinase 1 inhibits hedgehog signaling and medulloblastoma growth through GLI1 phosphorylation. *International Journal of Oncology*, (2018).
110. H. Sasaki, C. Hui, M. Nakafuku, H. Kondoh, A binding site for Gli proteins is essential for HNF-3beta floor plate enhancer activity in transgenics and can respond to Shh in vitro. *Development* **124**, 1313-1322 (1997).
111. S. Y. Cheng, J. M. Bishop, Suppressor of Fused represses Gli-mediated transcription by recruiting the SAP18-mSin3 corepressor complex. *Proceedings of the National Academy of Sciences* **99**, 5442-5447 (2002).
112. J. He *et al.*, Single-cell analysis reveals bronchoalveolar epithelial dysfunction in COVID-19 patients. *Protein Cell* **11**, 680-687 (2020).



## Acknowledgement

많은 분들의 관심과 도움 덕분에 박사과정을 무사히 마무리 지을 수 있었습니다. 저에게 도움을 주신 분들께 감사의 말씀을 드리고자 글을 적습니다.

가장 먼저, 저의 부족함에도 인내심을 가지고 귀중한 조언을 아끼지 않으신 저의 스승님 박찬영 교수님께 감사드립니다. 교수님의 지도아래 박사과정을 보낸 것은 제 인생에 너무 큰 행운이고 영광이었습니다. 교수님의 연구에 대한 열정, 지식과 지혜를 본받아 자랑스러운 제자, 더 나은 연구자가 되도록 더욱 더 노력하겠습니다. 바쁘신 와중에도 진심 어린 조언 해주시고 논문을 끝까지 마무리할 수 있도록 도움주신 박태주 교수님, 고명곤 교수님, 권태준 교수님, 그리고 정용규 교수님께 깊은 감사 인사를 드립니다. 그리고 학부생 인턴 시절부터 격려 아끼지 않아 주신 서영교 교수님, 이상민 박사님 감사합니다. 다양한 현미경 실험에 도움주신 허진희 선생님과, 정홍찬 선생님께도 감사의 말씀을 드립니다.

실험실 구성원들에게도 고마움을 전하고 싶습니다. 먼저 박사과정의 길을 걸으면서 학문적, 인간적 조언을 아끼지 않은 김규민 박사님, 이상권 박사님 감사합니다. 아무것도 모르는 저에게 실험 방법, 문제 해결 방법을 알려주고 밤 늦게 물어봐도 알려주던 그 친절함을 잊지 않겠습니다. 학부생 시절부터 가장 많은 시간을 함께 보낸 동기 수지, 영천이 오빠에게 감사인사를 전합니다. 수업, 시험, 실험실 생활까지 모든 시간이 함께여서 참 좋았습니다. 항상 고민을 잘 들어주고 자기일처럼 생각해주며 저를 도와주어서 고맙습니다. 그리고 실험실 연차로서는 1년 후배지만 선배 같은 든든한 랩장 윤영이, 항상 저를 응원해주고 도와주어서 고맙습니다. 서성경 선생님, 이애연 선생님. 새로운 시각으로 꼼꼼하게 피드백 해주시고 저를 응원해 주셔서 감사합니다. 선생님들이 계셔서 참 좋았습니다. 잊지 않고 실험실을 찾아와 주는 준호오빠, 학부생 인턴시절을 함께 보낸 동현이, 기현이 오빠 함께여서 즐거웠습니다. 나의 첫 사수 성국이, 친절하게 잘 알려주지 못한 것 같아 미안하고 부족한 저를 따라주어서 정말 고맙습니다. 모두들 행복하시길 바랍니다.

마지막으로 저를 항상 응원해주고 지원을 아끼지 않으시는 가족들에게 감사합니다. 자랑스러운 딸, 누나, 며느리가 되도록 하겠습니다. 물심양면으로 도와주고 응원과 격려 아끼지 않은 사랑하는 우리 남편 이재준님 감사합니다. 앞으로도 잘 부탁드립니다.

박사학위 과정 동안 도움주신 많은 분들의 도움과 응원을 항상 기억하며 더 나은 연구자가 되도록 열심히 노력하겠습니다. 감사합니다.



